DEPOSITION AND CHARACTERIZATION OF HIGH-K (Ca,Sr)ZrO_3 THIN FILMS USING SOL-GEL TECHNIQUE

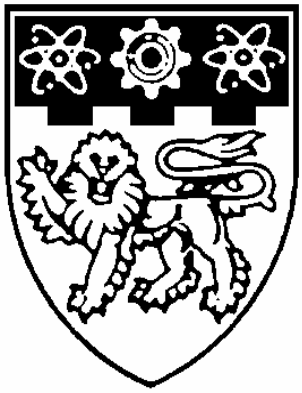

YU TING

SCHOOL OF ELECTRICAL & ELECTRONIC ENGINEERING
NANYANG TECHNOLOGICAL UNIVERSITY

2005

Deposition and Characterization of High-K $(Ca,Sr)ZrO_3$ Thin Films Using Sol-Gel Technique

Yu Ting

School of Electrical & Electronic Engineering

A thesis submitted to the Nanyang Technological University
in fulfillment of the requirement for the degree of
Doctor of Philosophy

2005

Statement of Originality

I hereby certify that the work embodied in this thesis is the result of original research and has not been submitted for a higher degree to any other University or Institution.

Date

Yu Ting

ACKNOWLEDGMENTS

I owe a great gratitude to my supervisor Prof. Zhu Weiguang for his invaluable guidance, helpful suggestion and persistent encouragements throughout the study. His broad knowledge and enthusiasm has a lasting effect on me. His kindness and patience are also deeply appreciated.

I would like to express my gratitude to Dr. R Gopal Krishnan for his inspiration and guidance. I would also thank A/Prof. Tan Ooi kiang for his useful suggestions and encouragements.

I also wish to express my appreciation for the help provided by other graduate students and research staff. In particular, I would like to thank Dr. Chen Changhong, Dr. Wang Zhihong, Dr. Chen Xiaofeng, Mr. Lu Yuekang, Mr. Zhao Changlei, Ms. Hu Ying, Mr. Chao Chen, Mr. Du Jinlong and Mr. Lu Hua. They are nice enough to share their invaluable knowledge and experience with me. The assistance provided by all the technicians in Sensors and Actuators Lab, Characterization Lab, and Photonics Lab is highly appreciated.

Finally, from the bottom of my heart, I want to thank my parents for their love and support.

SUMMARY

The continuous down-scaling of CMOS device dimensions has been the main stimulus to the growth of microelectronics and the computer industry over the past two decades. There are growing interests in high-k dielectric materials because of their broad future applications for semiconductor industry such as alternative gate oxide, high-density storage capacitors, and high-voltage capacitors. According to recent discoveries, there are a few reports on the research field of perovskite zirconate thin films for the applications of semiconductor technologies, therefore, the sol-gel derived $Ca_xSr_{1-x}ZrO_3$ dielectric thin films have been systematically investigated in this thesis for potential electronic device applications.

$Ca_xSr_{1-x}ZrO_3$ dielectric thin films have been synthesized using the sol-gel technique and systematically studied for electronic device applications. The microstructure, dielectric and electrical properties are characterized and analyzed. The influence of the deposition process, composition ratio and preparation conditions on the microstructure, dielectric and electrical properties of $Ca_xSr_{1-x}ZrO_3$ thin films have been systematically investigated. It is shown in the structural studies that the films are amorphous when annealed below 600 ºC, and are composed of crystallized perovskite grains with further increasing annealing temperatures.

The Schottky mechanism dominates in amorphous $CaZrO_3$ and $SrZrO_3$ thin films at high electric fields. On the other hand, the Poole-Frenkel mechanism is dominant in polycrystalline $CaZrO_3$ and $SrZrO_3$ thin film at high electric fields. The lowest leakage current densities of the $CaZrO_3$ thin films post-annealed in air and O_2 atmosphere are approximately 1×10^{-8} A/cm^2 and 1×10^{-9} A/cm^2 at 1 M*V*/cm, respectively. $CaZrO_3$ thin films show good electrical properties in terms of a dielectric constant of about 20 and leakage current density of 1×10^{-7} A/cm^2 at a high applied electric field of 2.6 M*V*/cm.

X-ray photoelectron spectroscopy (XPS) analysis of C1s, Ca2p and Zr3d lines have been performed on $SrZrO_3$ and $CaZrO_3$ thin films annealed at 700 ºC. Although two C1s lines are detected in the spectra, O1s referencing is found to be useful in interpreting the XPS spectra of $SrZrO_3$ and $CaZrO_3$ thin films.

Reflection infrared spectroscopy studies provide detailed insight in the chemical structure development of sol-gel derived $Ca_xSr_{1-x}ZrO_3$ thin films. Three main bands are clearly shown in the Fourier transform infrared spectroscopy (FTIR) spectra. One is focused on the modes of metal-oxygen (M-O) vibrating at 400 ~ 800 cm^{-1}, the others are the modes of C-O stretching, C=O stretching, C-H bending, O-H bending and C=C stretching vibrations at 1300-1800 cm^{-1} and CO_2 reflectance bands at 2340 and 2363 cm^{-1} approximately. The intensities of the bands at 1300 ~ 1800 cm^{-1} decrease with the increase of annealing temperature, indicating that the dissociation

and evaporation of metal-organic compounds have occurred.

Auger electron spectroscopy (AES) depth profiling presents a clear evidence for the interdiffusion of Pt/Ti bilayer in oxidizing environments at high temperatures. The interface reactions are complicated. In the initial stage of oxygen heat-treatment, Ti diffuses from the Ti under layer, reacts with O diffused from the surrounding gas around the center region of Pt layer or from dissociated SiO_2 to form titanium oxide. With increase in annealing temperatures, the formation of the titanium oxide increases. Higher annealing temperatures result in the formation of titanium oxide in the surface Pt grain boundaries.

Compared to ZrO_2 oxide thin films, $Ca_xSr_{1-x}ZrO_3$ thin films show higher crystallization temperatures and lower leakage current densities. With their relatively high and stable dielectric constants, $Ca_xSr_{1-x}ZrO_3$ thin films are promising candidates for high-k microelectronic device applications.

TABLE OF CONTENTS

LIST OF FIGURES

LIST OF TABLES

CHAPTER ONE

INTRODUCTION

1.1 Motivation

Device scaling has been the primary means by which the semiconductor industry has achieved the historically unprecedented gains in productivity and performance quantified by the Moore's Law, which states that transistor performance and density double every 3 years [1]. These gains have traditionally been paced by the development of lithography tools, photoresist materials and critical dimension etch processes. In the past several years it has become clear that despite advances in these crucial process technologies and the resultant ability to produce ever-smaller feature sizes, the crux of the problem comes from the fact that the traditional transistor and capacitor formation materials, silicon, silicon dioxide, and polysilicon have been pushed to the fundamental material limits and continued scaling has required the introduction of new materials [2]. Unless new methods are developed, further scaling

of the transistor will result in the loss of total charge, increase in resistance, and potential decrease in performance [3].

In no area is this issue more clear or urgent than in the MOSFET (metal-oxide-semiconductor-field-effect transistor) gate stack. Silicon dioxide has been used for more than 30 years as the gate dielectric for MOSFET. With other device parameters properly scaled (for example, source/drain resistance and overlap capacitance), optimal performance can be achieved by maximizing the gate-to-channel capacitance of the MOSFET, for instance, by minimizing the associated oxide thickness. The rapid scaling of CMOS technology over the last few years has resulted in the reduction of gate dielectric thickness to about only 1 nanometer. The oxide layer has become so thin that the quantum mechanical tunneling of electrons from the silicon substrate to the gate electrode is now possible [4]. State-of-the-art gate oxide thicknesses are currently between 1.5 and 2.0 nm [5]. At these dimensions, the leakage current density rises to 1~10 A/cm^2 [6]. Gate leakage becomes dominated by the direct tunneling current, which must be limited to meet both stand-by power specifications and reliability requirements. Some estimates suggest that the standard SiO_2 (or its nitrogen containing variants) will cease to be useful when thickness is reduced to below 1.0 nm. The future of CMOS down to and below the 0.1 μm gate lengths may well hinge on finding a replacement of silicon dioxide as the gate insulator. Further gate capacitance improvements might be possible by integrating a

higher dielectric constant material into the gate dielectric. In principle, these materials would allow a proportionally higher voltage at an equivalent capacitance or a higher capacitance for the same voltage.

Memory cell capacitance will be one of the most critical challenges which Gbit density DRAM (dynamic random access memory) faces. The best-suited dielectric material would have a low leakage current and a high dielectric constant for the applications of DRAM. DRAM capacitor technology faces new challenges of introducing new storage capacitor dielectric materials. For the 130 nm node, a poly-silicon bottom electrode and a 3D capacitor cell with high-k dielectric and metal counter-electrode are needed (this is an example of Metal Insulator Silicon (MIS) structure). A gate stack with an effective dielectric constant of 10 ~ 20 is a promising choice for this node [1].

The stringent requirements for ten years reliability of CMOS devices will be a demanding challenge on any high-k material candidate. Furthermore, failure mechanisms and reliability of any potential high-k dielectric material need to be understood. High temperature materials particularly zirconates are currently gaining considerable importance. There is a growing interest in calcium zirconate-based oxides for potential sensor/device applications at elevated temperatures. In particular, several studies have been reported on the use of calcium zirconate-based systems for

monitoring oxygen [7, 8], humidity，hydrogen, hydrocarbons and as a thermistor material [9-13]. It has been shown that in (Ca, Sr, Ba) zirconate system, the Ca, Sr-rich composition region with orthorhombic perovskite-type structure has suitable dielectric constant of 29 ~ 32 and widely adjustable temperature coefficient of dielectric constant (-50 to +50 ppm/°C) [14]. Due to their high temperature thermodynamic stability, high dielectric constant and high dielectric breakdown strength, they are promising materials for the next generation of semiconductor applications.

To our knowledge, there are a few reports on perovskite zirconate thin films for semiconductor technologies such as the alternative gate dielectric and high voltage capacitor. Therefore, it is very worthwhile to explore the microstructural, dielectric and electrical properties of preovskite zirconate $Ca_xSr_{1-x}ZrO_3$ thin films for future high-k microelectronic device applications. It will have a significant meaning for both scientific understanding and technological applications.

1.2 Objectives

In this thesis, the goal is to extend the fundamental understanding on these high-k dielectric thin films for potential electronic device applications. $Ca_xSr_{1-x}ZrO_3$ dielectric thin films, which have a much denser structure and a much lower leakage current density than those of popular currently used high-k dielectric films, are

deposited using the sol-gel wet chemical technique. Then systematic characterizations on physical, electrical and dielectric properties are investigated, and the conduction mechanism study is carried out.

Firstly, the sol-gel technique is successfully employed to $Ca_xSr_{1-x}ZrO_3$ thin films owing to its easy control in the composition. The influence of the deposition process on the microsturctural features and dielectric properties of the $Ca_xSr_{1-x}ZrO_3$ thin films are discussed. Based on these studies, the microstructure and composition dependence of dielectric thin films performance are expected to extend the fundamental understanding of these complex perovskites for the potential high-k microelectronic device applications.

Secondly, the conduction mechanism of $Ca_xSr_{1-x}ZrO_3$ thin films is discussed. The prescribed research works include the effects of bottom electrodes, heat-treatment, and other preparation conditions. It is anticipated that these research works would extend our knowledge on the electrical property of the high-k dielectric thin film, and in turn afford useful understanding for the applications of these perovskite high-k dielectric materials.

1.3 Major contributions of the thesis

The major contributions achieved in this thesis are summarized as follows:

1. The calcium strontium zirconate $Ca_xSr_{1-x}ZrO_3$ thin films have been successfully synthesized by a sol-gel route in a series of compositions. The phase development and microstructures have been investigated by X-ray diffraction (XRD), atomic force microscopy (AFM), and Fourier transform infrared spectroscopy (FTIR).
2. The influence of the deposition process and composition ratio on the microstructure, dielectric and electrical properties of $Ca_xSr_{1-x}ZrO_3$ thin films has been systematically investigated. The dielectric properties and electrical properties have been characterized and analyzed.
3. X-ray photoelectron spectroscopy (XPS) analysis of C1s, Ca2p and Zr3d lines have been performed on $SrZrO_3$ and $CaZrO_3$ thin films annealed at 700 ºC. Although two C1s lines are detected in the spectra, O1s referencing is found to be useful in interpreting the XPS spectra of $SrZrO_3$ and $CaZrO_3$ thin films.
4. Reflection infrared spectroscopy studies provide detailed insight in the chemical structure development of sol-gel derived $Ca_xSr_{1-x}ZrO_3$ thin films. There are three main bands for determining the phase transformation from the carbonate decomposition to the growth of the perovskite phase in the films. Between 2500 and 2200 cm^{-1}, the 2340 and 2363 cm^{-1} reflectance peaks are assigned to CO_2. Between 1800 and 1300 cm^{-1}, the bands typically involve C=O stretching, C-H bending, O-H bending, C=C stretching, and C-O stretching vibrations. Between 800 and 400 cm^{-1}, the Zr-O stretching vibrations are observed. All of the IR

spectra suggest complete decomposition of the carbonate and the growth of the perovskite phase when the films are annealed at above 600 ºC.

5. Auger electron spectroscopy (AES) depth profiling presents a clear evidence for the interdiffusion of Pt/Ti bilayer in oxidizing environments at high temperatures. The interface reactions are complicated. Annealing in an oxidizing atmosphere causes oxidation of the intermediate Ti layer and its migration into Pt grain boundaries. Ti diffused from the Ti under layer, reacts with O diffused from the gas environment around the center region of Pt layer or SiO_2 dissociation to form titanium oxide, and higher annealing temperatures result in the formation of titanium oxide in the surface Pt grain boundaries.
6. Electrical properties and leakage current mechanisms of $CaZrO_3$ and $SrZrO_3$ dielectric thin films have been studied. These thin films are deposited on Pt/Ti/SiO_2/*n*-Si and Pt/TiO_2/SiO_2/*n*-Si substrates by the sol-gel wet chemical technology, and then annealed at temperatures ranging from 550 to 700 ºC for 1h in O_2 or air. These films with platinum top and bottom electrodes are characterized with respect to the leakage current density as a function of temperature and applied voltage. $CaZrO_3$ shows good electrical properties in terms of a dielectric constant of about 20 and leakage current density of 1×10^{-7} A/cm^2 at a high applied electric field of 2.6 M*V*/cm. The data can be interpreted via a thermionic emission model. The Schottky mechanism dominates in amorphous $CaZrO_3$ and $SrZrO_3$

thin films at high electric fields. On the other hand, the Poole-Frenkel mechanism is dominant in polycrystalline $CaZrO_3$ and $SrZrO_3$ thin films at high electric fields.

7. Compared to ZrO_2 oxide thin films, the high temperature thermodynamic stability, high dielectric constant, low leakage current density and high breakdown strength suggest that $Ca_xSr_{1-x}ZrO_3$ thin films are promising candidates for high-k microelectronic device applications.

1.4 Organization of the thesis

This thesis has studied $Ca_xSr_{1-x}ZrO_3$ high-k dielectric thin films for potential microelectronic device applications, and is organized into six chapters.

Chapter 1 provides a general introduction to the state-of-the-art on the high-k materials and electronic devices. The motivations for developing $Ca_xSr_{1-x}ZrO_3$ high-k dielectric thin films are explained. Then, the objectives, major contributions, and organization of the thesis are presented.

Chapter 2 devotes to the fundamental background and related literature review with respect to the applications of high-k dielectric materials. First, the material candidates for high-k electronic applications are reviewed. Next, the present status of the high-k dielectric thin film development is introduced. Then, the difficulties and problems in

this research area are presented. Finally, the conduction phenomena in perovskites and the development of the sol-gel technology for the film deposition are presented.

Chapter 3 gives the detailed experimental procedures used in this research project, including the synthesis of precursor solution, deposition and characterization of the resultant thin films. First part describes the precursor solution preparation process and the deposition steps of the sol-gel technology followed by the fabrication of the top electrode for MIM structure measurements. Finally, the instruments for characterizing properties of $Ca_xSr_{1-x}ZrO_3$ thin films are presented.

Chapter 4 presents the details of the microstructures and physical properties of the obtained $Ca_xSr_{1-x}ZrO_3$ thin films. The influences of the annealing temperature and composition ratio on the structure evolution of $Ca_xSr_{1-x}ZrO_3$ thin films are firstly discussed. Then, the study on the dielectric properties is followed as a correlation to their microstructure. A discussion on the dielectric properties is conducted based on the experimental results. Since currently ZrO_2 is one of the popular research focuses as a high-k candidate, the comparison of ZrO_2 thin films and $Ca_xSr_{1-x}ZrO_3$ thin films using the same sol-gel process is given in the last section.

Chapter 5 analyzes the effects of heat-treatment and preparation conditions on the electrical properties of $Ca_xSr_{1-x}ZrO_3$ thin films. The conduction behaviors of

$Ca_xSr_{1-x}ZrO_3$ thin films are investigated and the discussion on conduction mechanisms is made.

Finally, the conclusion from this work and recommendations for future work are given in Chapter 6.

CHAPTER TWO

LITERATURE REVIEW

In this chapter, the fundamental knowledge and related literature review with respect to high-k materials, conduction phenomena and sol-gel technology are presented. This chapter serves to provide the related background of the research work on the high-k dielectric materials for microelectronic device applications and comprises of four sections. The first section gives the present status of high-k thin film research. Then the considerations on high-k materials properties for microelectronic device applications are discussed. After that the materials studied in this research work are introduced. The third section gives the basic principles of the conduction phenomena in the perovskite thin films. Sol-gel technique for the deposition of thin films is presented in the last section.

2.1 Present status of high-k thin film research

The latter half of the 20th century has surely come to be known as the silicon revolution. The integration of semiconductor devices has gone through medium (MSI), large (LSI), very large (VLSI), and now ultralarge-scale integration (ULSI). The continuous down-scaling of CMOS device dimensions has been the main stimulus to the growth of microelectronics and the computer industry over the past two decades. Since the traditional transistor and capacitor formation materials, silicon, silicon dioxide, and polysilicon have been pushed to the fundamental material physical limits and for continued device scaling, it is very important to explore new materials to replace traditional materials. High-k dielectric materials show promise for applications in semiconductor industry such as alternative gate oxide, high-density storage capacitors, and high-voltage capacitors.

The dominant electronic device used today in integrated circuits is the silicon-based metal oxide semiconductor (MOS) transistor, which consists of a source, drain, channel, and gate region. A typical modern CMOS transistor structure is shown in Figure 2-1 [15]. For decades, the semiconductor industry has been able to continue increasing the amount of circuitry on a chip while reducing its size—enabling smaller, faster and better electronic products. Silicon dioxide has been used as the primary gate dielectric material in field-effect devices since 1957, when the usefulness of the Si/SiO_2 material system was first demonstrated [16-19]. The reason for the nearly

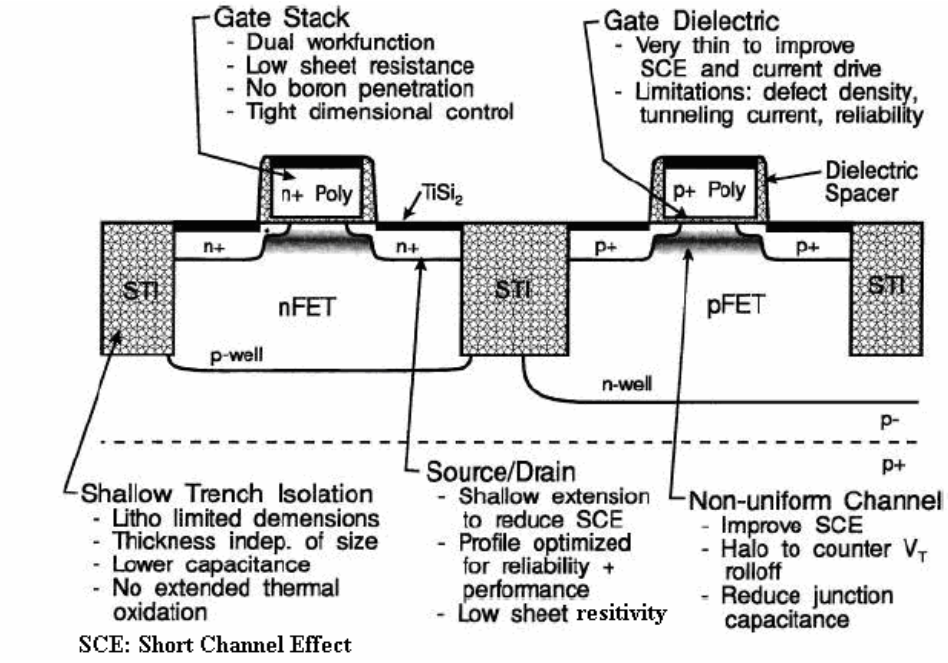

Figure 2-1. A cross-sectional diagram of typical a state-of-the-art CMOS [15].

exclusive use of silicon dioxide in this application is that silicon dioxide uniquely possesses the required combination of several properties: good mobility of holes and electrons flowing in silicon at the silicon dioxide interface, ability to keep defect states at this interface low, relatively low trapping rates of holes and electrons, and excellent compatibility with CMOS processing. At first single devices and then integrated devices were made, and the thickness of SiO_2 films decreased with each generation. After years of exponential growth we are finally encountering fundamental limits. Up until now the CMOS circuit has been scaled with little concern for fundamental limits. Scaling challenges have been met with appropriate lithography improvements, reduction of gate oxide thickness, and the use of shallower implanted junctions (with

reduced thermal cycle) and contacts. Notwithstanding important improvements have been made along the way, such as self-aligned silicides (1982) and halo-doping of source and drain (1985). These have allowed the scaling of the channel lengths down to ~ 0.1 μm, the basic device structure and physics of operation of the MOSFET has remained substantially the same over all these years, thus enabling confident predictions of future performance. Several factors conspire to make further evolutionary change difficult for sub-0.1μm gate lengths such as lithography, controlling diffusion profiles, and generating sufficiently shallow and low-resistance contacts, but more fundamental limits are being encountered such as tunneling through thin oxides and through narrow depletion layers, as well as increasing variability in device characteristics caused by random impurities [20].

Table 2-1. The roadmap of the high performance logic technology requirements [2].

	2001	2002	2003	2004	2005	2006	2007	2010	2013	2016
DRAM ½ Pitch [nm]	130	115	100	90	80	70	65	45	32	22
MPU ½ Pitch [nm]	150	130	107	90	80	70	65	45	32	22
MPU Printed GL [nm]	90	75	65	53	45	40	35	25	18	13
MPU Physical GL [nm]	65	53	45	37	32	28	25	18	13	9
Gate oxide thickness (A)	20	17	14	12	10	9	8	6	4	3

The problem lies with the current gate insulating material, a layer of silicon dioxide. The silicon dioxide layer "gates" the electrons, controlling the flow of electricity across the transistor. Each time the chip is reduced in size, the silicon dioxide layer must also be proportionally thinned to maintain a value of capacitance to reduce short-channel effects and to keep device drive current at an acceptable level. At the current pace of chip progression, the gate oxide thickness will need to be reduced to fewer than 10 angstroms in the next ten years. The silicon industry roadmap dictates 1.2 nm SiO_2 gate dielectrics for 0.09 μm technology today, and calls for <1 nm equivalent SiO_2 thickness for 0.05 μm technology in 2012. Table 2-1 shows the recent roadmap (ITRS) of the high performance logic technology requirements [2].

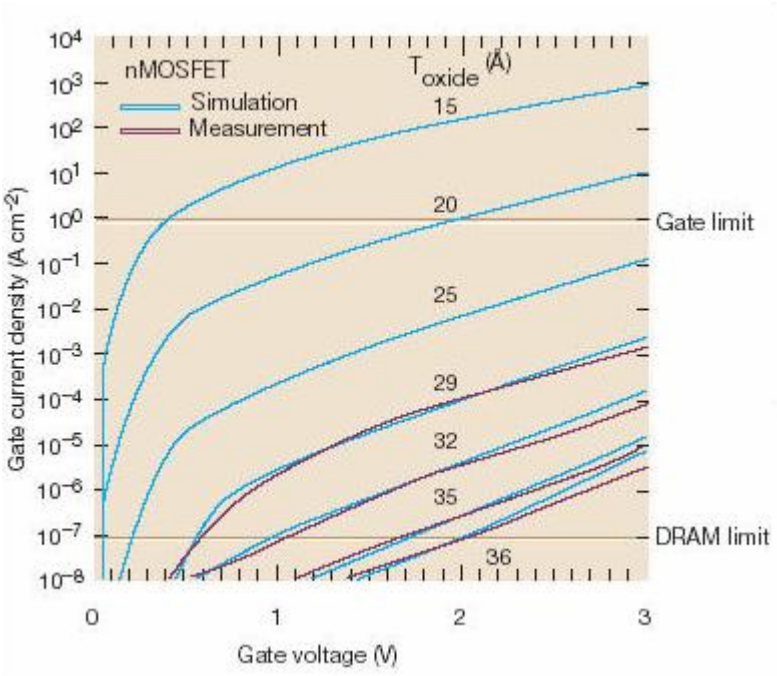

Figure 2-2. Gate leakage density versus gate voltage for various oxide thicknesses [21].

For silicon dioxide thickness of ~ 35 Å at a gate bias of ~ 1*V*, the leakage current density is at 1×10^{-12} A/cm^2 range. Unfortunately, once the thickness is reduced to 20 Å or less, the leakage current density can rise to 1~10 A/cm^2, thus the silicon dioxide is no longer able to provide effective insulation due to the effects of the quantum tunneling current and the devices will fail to work properly [21]. Figure 2-2 shows the gate leakage current density versus gate voltage for various oxide thicknesses. At a gate bias of 1.5 *V*, the current density increases by 10 orders of magnitude as the oxide thickness decreases from 36 Å to 15 Å. The tunneling current density calculated for a 15 Å oxide agrees reasonably well with the reported experimental data. If we assume the gate leakage limit occurs for devices with 100 Å gate length designed for 1.0 *V* operation, the SiO_2 thickness limit occurs at ~ 16 Å.

This exponential increase in gate leakage current with decreasing dielectric thickness will likely be one, if not the mayor contributor, leading to the limited extendibility of SiO_2 as the gate dielectric in the 15-20 Å regime. To develop an effective gate insulator at a dimension of fewer than 20 Å, most industry experts predict the need to develop new materials with a higher dielectric constant (sometimes referred to as high-k materials).

A potential road map for thermal/thin films is given in Figure 2-3 [2]. It can be easily seen from Figure 2-3 that many materials have been suggested that could replace

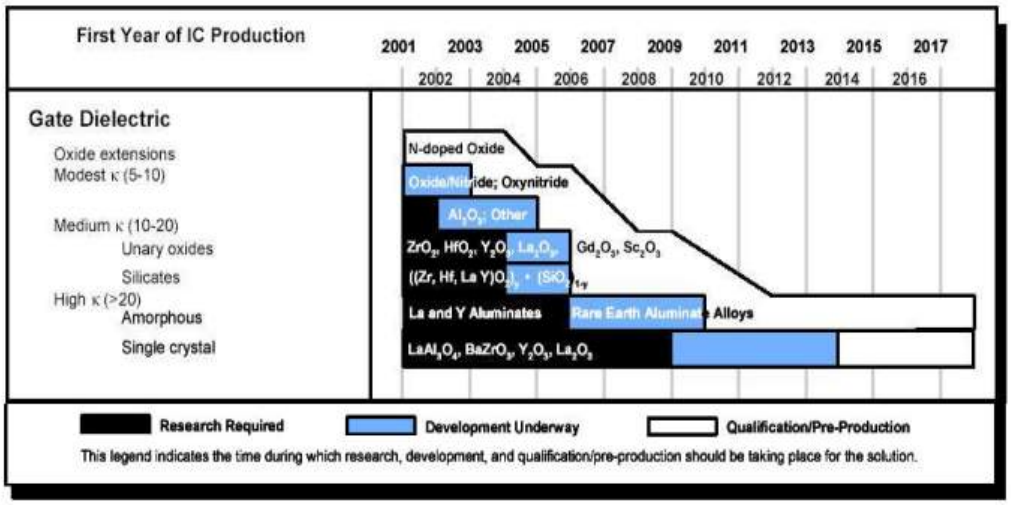

Figure 2-3. Thermal/Thin films potential solutions [2].

silicon dioxide or silicon nitride as a possible gate dielectric. The most common of these are simple metal oxides such as TiO_2 [22-26], Ta_2O_5 [27-38], Al_2O_3 [39-42], ZrO_2 [43-46] and HfO_2 [47-52]. Ferroelectric materials such as PZT (lead zirconate titanate) [53, 54] have also been suggested as gate dielectrics. A summary of the appropriate materials properties for the selection of materials for gate dielectric applications will be discussed in the next section.

2.2 The considerations of high-k materials properties

All of the materials systems should meet a set of criteria for the application. A summary of considerations on the high-k materials properties for microelectronic device applications is given below.

2.2.1 Tunneling current and bandgap

One of the fundamental limits to the scaling of the gate dielectric is the exponential increase in the tunneling current with decreasing film thickness. The reduction of gate leakage current is an important reason for replacing SiO_2-based dielectrics. For a given technology, CMOS devices are designed with a specific gate capacitance. To reduce the leakage current while maintaining the same gate capacitance, a thicker film with a higher dielectric constant is required. The gate leakage current, at least for direct quantum-mechanical tunneling, is exponentially dependent upon the dielectric thickness, while the capacitance is only linearly dependent on the thickness. At first glance, this would seem to be a winning proposition, since a substantial reduction in the current should be possible with only small increases in thickness. There is, however, another exponentially dependent term in the tunneling current-the barrier height between the cathode and the conduction band of the insulator. For a large number of dielectrics, the tunneling current is exponentially dependent upon the barrier height [55, 56] as shown in following equation (2-1):

$$J_{DT} = \frac{A}{d^2}\exp\left(-2d\sqrt{\frac{2m^* q}{\hbar^2}\left\{\Phi_B - \frac{V}{2}\right\}}\right) , \qquad (2\text{-}1)$$

here A is a constant, d is the physical thickness of the dielectric, m^* is the electron effective mass in the dielectric, Φ_B is the potential barrier between the metal and dielectric, and V is the voltage drop across the dielectric. For highly defective films which have electron trap energy levels in the insulator band gap, a trap-assisted mechanism such as the Poole-Frenkel emission or hopping conduction

will govern the electron transport, as described by equations (2-2) and (2-3), respectively;

$$J_{PF} = E\exp\left(-\frac{q}{kT}\left\{\Phi_B - \sqrt{\frac{qE}{\pi\varepsilon_i}}\right\}\right), \tag{2-2}$$

$$J_{hop} = \frac{q^2 l^2 n^* \Gamma E}{kT}, \tag{2-3}$$

here E is the electric field in the insulator, l is the interval of separation between adjacent hopping sites, n^* is the density of free electrons in the dielectric, and Γ is the mean hopping frequency. Therefore, not only is a material with higher dielectric constant required, but this material must also have a suitably large bandgap and barrier height, to keep the gate leakage currents within reasonable limits. For most of these high-k materials, the bandgap is inversely proportional to the dielectric constant, following approximately a $E_g \approx 1/\varepsilon^2$ law [26]. As dielectric constant increases, the bandgap decreases, which is shown in Figure 2-4.

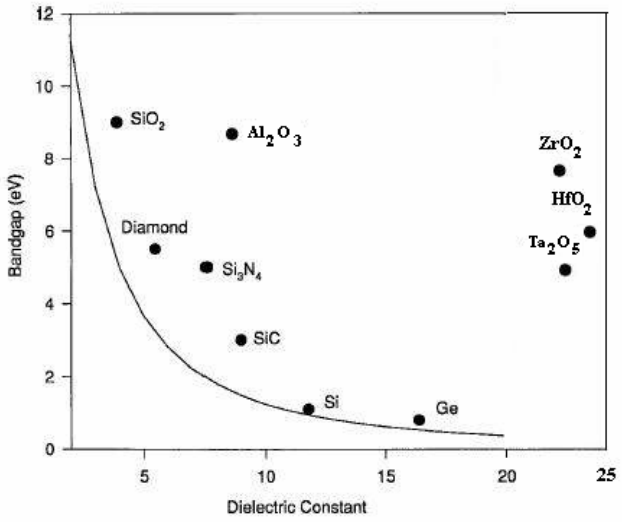

Figure 2-4. Relationship between bandgap and permittivity for several commonly studied gate dielectric materials [26].

Thus, even if there is a reduction of the leakage current due to the increased thickness, this may be nullified by the reduction of the barrier height. Since both the thickness and barrier height have an exponential influence upon the leakage current, it is an optimization problem to discover which will have the larger effect.

Alumina (Al_2O_3) has many favorable properties for the gate application, such as a high bandgap, thermodynamic stability on Si up to high temperatures, and is amorphous under the conditions of interest [57, 58]. The biggest drawback is that Al_2O_3 only has low permittivity k ~ 8-10; therefore makes it a relatively short-term solution for industry needs (1-2 generations). Although many people initially assumed that selecting a dielectric with k > 25 would be necessary to replace SiO_2, the more relevant consideration is whether the desired device performance can be obtained at the prescribed operating voltage without producing unacceptable leakage currents and reliability characteristics. Therefore it is more appropriate to find a dielectric which provides a large tunneling barrier and high-quality interface to Si. With this in mind, if a single dielectric layer can be employed, then even a material with k ~ 12-20 will allow a physical dielectric thickness of 35 ~ 50 Å to obtain the equivalent oxide thickness values required for 0.1 μm CMOS and beyond.

2.2.2 Interface quality

Interface problem is the most critical problem nowadays in thin film. And recently nearly all the efforts have been dedicated to how to control the interface to achieve better gate properties.

For all thin gate dielectrics, the interface with Si plays a key role, and in most cases it is the dominant factor in determining the overall electrical properties. Therefore, any potential high-k gate dielectric should attain a sufficiently high-quality interface with the Si channel, as close as possible to that of SiO_2. It is crucial to understand the origin of the interface properties of any high-k gate dielectric, so that an optimal high-k dielectric-Si interface may be obtained. In order to maintain a high-quality interface and channel mobility, it is important to have no metal oxide or silicides phases at or near channel interface. Several simple oxides such as ZrO_2 and HfO_2 have been previously reported as having high oxygen diffusivities [59]. Any annealing treatments which have an excess of oxygen will lead to rapid oxygen diffusion through the oxide, resulting in SiO_2 or SiO_2-containing interface layers. This SiO_2 formation at the interface will severely compromise the capacitance gain from any high-k layers in the gate stack. Caution must therefore be taken in assessing the interface stability of high-k dielectrics, as resistance to oxygen diffusion in annealing ambient should be characterized. The relevant annealing ambient is forming gas (typically 90% N_2:10% H_2), which is a standard final anneal in the CMOS process and

is believed to passivate interfacial traps with hydrogen. Since many high-k dielectrics will be reduced in the presence of H_2, it is important to study the change of characteristic with respect to the effect of annealing in the reducing ambient.

High-k materials such as hafnium oxide and zirconium oxide exhibit a tendency to trap electrons. Charge trapping and mobility degradation now become one of the most concerned problems. Most of the charge is being trapped in the interface layers. Until now, there is no consensus whether mobility degradation and threshold voltage instability are problems intrinsic to all metallic high-k materials [60]. With charge trapping, the voltage applied at the gate is instead absorbed in the “traps” that mine the channel. It degrades transistor performance by reducing the gain and causing delay.

A team from University of Texas at Austin led by Jack C. Lee has tackled the problem by incorporating nitrogen in the hafnium dioxide gate dielectric and by high-temperature forming gas anneal, which increases electron mobility while reducing the boron penetration of the gate oxide [61]. This has allowed them to achieve an ultrathin equivalent oxide thickness of 0.7 nm, outpacing the International Technology Roadmap for Semiconductors (ITRS), which calls for a 0.9 to 1.4 nm thickness range at the 90-nm node. Even with a 0.7-nm-thin gate oxide, mobility is still too low compared with that of silicon dioxide. To boost capacitance, this team has tried a hydrogen-based forming gas anneal at temperatures ranging from 500 ºC to 600

ºC, rather than the standard 400 ºC, and that has yielded substantial improvements in rooting out traps in the dielectrics and therefore increased the mobility. They are currently studying the long-term reliability of these forming gas-annealed devices. Use of hydrogen reduces the charge traps because the hydrogen fills dangling bonds at the interfacial layer and in the dielectric.

Capping layers have also proven to have a significant effect on scaling by suppressing reactions between the gate dielectrics and the gate electrode. Depositing CVD silicon gates directly onto Al_2O_3 capped HfO_2 showed greater than a 10^4 times reduction in gate leakage compared to the poly-si/HfO_2 of similar electrical thickness [62]. The addition of an $HfSi_xO_y$ capping layer to HfO_2 films has resulted in an equivalent of thickness (EOT) reduction by as much as 4 Å. It is most likely due to a reduction in interfacial reactions between the polysilicon electrode and the high-k material [63].

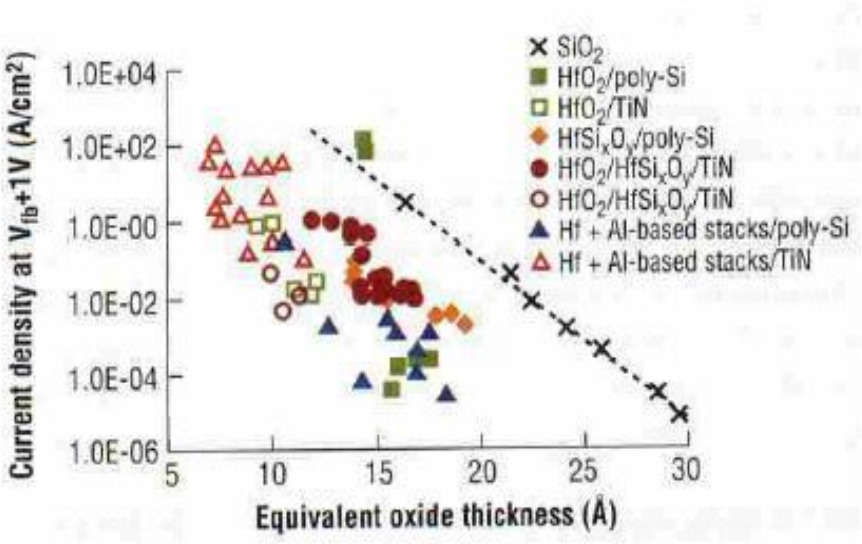

Figure 2-5. Scaling of various gate materials [63].

One of the most dramatic effects on scaling comes from the use of metal gate electrodes. In the case of the following evaluation taken by Murto *et al*. [63], a 10 nm CVD TiN layer was deposited prior to the polysilicon gate electrode. This resulted not only in a significant reduction in the capacitance equivalent thickness due to the elimination of gate depletion, but also in a significant reduction (0.5 nm) in the EOT for the elimination of the upper interfacial layer. A brief summary of Hf-based high-k material scaling efforts over the past few years at International SEMATECH is shown in Figure 2-5 [63].

2.2.3 Thermodynamic stability on Si

Unfortunately, most of the high dielectric constant materials studied, specifically Ta_2O_5 [31, 64], TiO_2 [22, 26] and Y_2O_3 [65, 66], are not sufficiently stable thermally. The formation of SiO_2 and/or metal silicides often occurs when these materials are deposited on silicon. An underlying SiO_2 layer reduces the effectiveness of any high-k material, since SiO_2 has a lower dielectric constant and thus reduces the effective capacitance of the film. Although a substantial amount of work has been reported on Ta_2O_5 as a gate dielectric, its inherent thermal instability when in direct contact with Si is a severe limitation as a gate dielectric. The TiO_2 system has also been heavily studied for high-k applications. TiO_2 shows a very high dielectric constant k ~ 80-110, makes it very attractive for gate applications. It is important to note that since TiO_2 is not stable on Si during deposition by CVD [67], all of the studies on TiO_2 system

contain both a reaction layer at channel interface and metal electrodes/gates to prevent reaction at the gate interface. Manchanda and Gurvitch have studied the Y_2O_3 for the purpose of high-k gate dielectrics [68, 69]. They found that the dielectric constant of the Y_2O_3 grown on SiO_2 was about k ~ 17, but for Y_2O_3 grown directly on Si, k ~ 12. That means this lower measured k value is likely resulted from growth of interfacial SiO_2.

It is important to understand the thermodynamics of the high dielectric constant materials, and thereby attempt to control the interface with Si. Although we find a material with a reasonably high dielectric constant that reduces the leakage current for a given equivalent oxide thickness, there is still the problem of integrating this material into ever more complicated device processing. The easiest integration would be that this material could be simply substituted for SiO_2 in a given CMOS process. Due to their thermodynamic instability, most of the alternative high-k materials can change phase (and therefore their material properties) at much lower temperatures than that needed for normal CMOS processing. It is also not clear that any of these materials could be used with poly-Si gates because of the materials' chemical reactivity with the poly-Si. Since most of the materials would not be compatible with the high-temperature processing required for most CMOS devices, the gate structure might have to be moved to the end of the device process instead of remaining at the beginning. Therefore, the use of high-k materials would require not only the discovery

and development of a new material, but possibly a complete re-engineering of the CMOS manufacturing process.

An important approach toward predicting and understanding the relative stability of a particular three-component system for device applications can be explained through ternary phase diagrams [70, 71]. An analysis of the Gibbs free energies governing the relevant chemical reactions for the Zr-Si-O system leads to the ternary phase diagram shown in Figure 2-6.

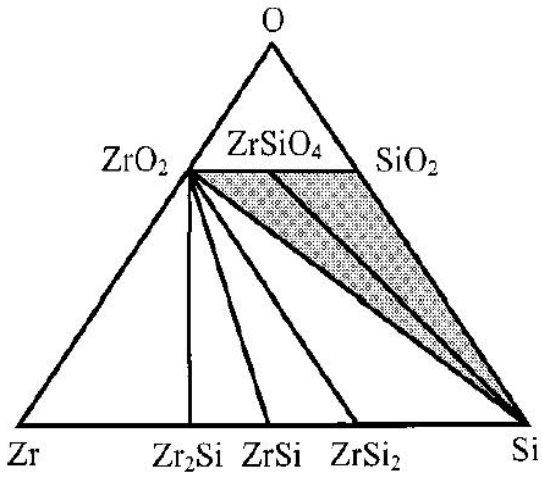

Figure 2-6. Ternary phase diagram for the Zr-Si-O system in the temperature ranges of 700 ~ 950 ºC [72].

The tie lines in the phase diagram for the Zr-Si-O system [72] indicate that the metal oxide ZrO_2 and the compound silicate $ZrSiO_4$ will both be stable in direct contact with

Si up to high temperature. The gray shaded area in Figure 2-6 denotes a large field of $ZrSi_xO_y$ compositions which are expected to be stable on Si up to high temperatures (700 ~ 950 ºC). Other $ZrSi_xO_y$ compositions outside of the gray area are also stable on Si, but since it is desirable to prevent any Zr-Si bonding, film compositions within the gray area are preferable. Gutowski [73] also found the HfO_2/Si interface stable with respect to the formation of silicides. Hafnium silicate is also stable in direct contact with Si, and by controllably incorporating a suitable high level of Si during deposition, the dielectric-Si interface will act more like the preferable SiO_2-Si interface [74]. Although the k values of $(HfO_2)_x(SiO_2)_{1-x}$ and $(ZrO_2)_x(SiO_2)_{1-x}$ are substantially lower than those of pure HfO_2 and ZrO_2, this tradeoff for interfacial control will be acceptable as long as the resulting leakage currents are sufficiently low.

The use of p^+ gates for CMOS process was first introduced to reduce short-channel effects and lower threshold voltages as the devices were pushed into the submicrometer regime [75]. However, with the use of boron as the dopant for the p^+ gates, dopant diffusion and its subsequent penetration into the gate dielectric have become a problem. The penetration of the boron into the gate dielectric causes a number of problems not only with the quality of the dielectric but especially with the device operation [76]. Boron penetration shifts the threshold voltage of MOS devices to more positive values. Degradation of the MOSFET transconductance and the

subthreshold slope is also correlated with boron penetration [76]. Typically boron is implanted into the poly-Si gate using sufficiently high doses to ensure reasonable conductance of the poly-Si gate. Unfortunately, it is also necessary to activate the dopant with a high-temperature anneal, typically in the range of 950-1050 ºC in an inert ambient for a few seconds. During the high-temperature annealing, the boron penetrates into and through the thin gate dielectric. It was reported that poly-Si deposition at a temperature of 620 ºC results in the reduction of ZrO_2 to form a Zr-rich layer near the poly-Si/ZrO_2 interface, leading to very high leakage currents. As an interim solution, nitrided and/or oxide/nitride stacks may serve to reduce boron-penetration effects, assuming the leakage current and reliability can be improved. The feasibility of such structures remains to be proven in manufacturing. Even if an oxide/nitride combination that would allow at least some scaling of CMOS was to be found, it is not clear that the thin oxide layers could pass the reliability criteria needed to produce reasonable devices. Using atomic layer chemical vapor deposition (ALCVD) method, Copel *et al.* [77] deposited a highly uniform layer of ZrO_2 as thin as 2 nm on top of a SiO_2 layer. This initial oxidation (SiO_2) limits the minimum achievable equivalent oxide thickness, but it provides a very high quality interface and at the same time a reactive surface for depositing the ultrathin layer of ZrO_2. They also found these ZrO_2 layers were thermally stable under vacuum annealing up to 900 ºC, but were observed to decompose at higher-temperature vacuum anneals of 1000 ºC.

2.2.4 Film morphology

Given the concerns regarding polycrystalline and single crystal films, it appears that an amorphous film structure is the ideal one for the gate dielectric.

Table 2-2. Comparison of relevant properties for high-k candidates [26, 81, 82, 83].

Material	Dielectric constant	Band gap (ev)	Crystal structure (900 ºC)	Drawbacks for application
SiO_2	3.9	8.9	Amorphous	
Al_2O_3	9	8.7	Amorphous	low dielectric constant
Y_2O_3	15	5.6	Cubic	relatively low dielectric constant thermodynamic instability
Ta_2O_5	26	4.5	Orthorhombic	low band gap thermodynamic instability
TiO_2	80	3.5	Tetragonal (rutile,anatase)	very low band gap thermodynamic instability
ZrO_2	25	7.8	Mono,tetrag,cubic	high oxygen diffusivity
HfSiO	11	5.3	Amorphous	relatively low dielectric constant
HfON	18	--	Amorphous	relatively low dielectric constant
HfSiON	14	--	Amorphous	relatively low dielectric constant
HfO_2	25	5.7	Mono,tetrag,cubic	high oxygen diffusivity
HfAlO	16	--	Amorphous	relatively low dielectric constant

One of the main problems is that common high-k dielectrics will crystallize at a fairly low temperature (much less than 900 ºC). As shown in Table 2-2, nearly all metal oxides of interest, with the exception of Al_2O_3, will form a crystallized film either during deposition or upon modest thermal treatments: HfO_2 and ZrO_2 are no exceptions. Crystal grain boundaries then can act as high dopant diffusivity paths and

may also be the cause of device failure and high leakage. For example, crystallized HfO_2 portions strongly degrade the electron mobility in hafnium silicate MISFETs [78].

And it should be noted that single crystal oxides grown by MBE methods [79, 80] can in principle avoid grain boundaries while providing a good interface, but these materials require submonolayer deposition control, which may only be obtainable by MBE approaches.

The good news is that adding nitrogen to the film helps to keep the film amorphous at temperatures of up to 700-800 ºC and also helps to improve the dielectric constant, Samsung, for example, found that incorporating nitrogen in HfSiON definitely enhanced its dielectric constant. HfSiON was amorphous up to 1100 ºC and showed a reduction in leakage current by more than three orders of magnitude compared with that of SiO_2 obtained with a nitrogen concentration of 30 % [81]. Researchers said that excellent properties of HfSiON were due to the suppression of crystallization, phase separation and microscopic inhomogeneity of the film, which can be achieved with nitrogen over 20 %. Also, by controlling the ratio between Si and Hf in HfSiO [82] and the ratio between Al and Hf in HfAlO [83], one can increase their crystallization temperature to 900-1000 ºC.

2.2.5 Process compatibility

A crucial factor in determining the final film quality and properties is the method by which the dielectric materials are deposited in a fabrication process. The deposition process for the dielectric must be compatible with the CMOS processing, cost and throughput. Since high-k dielectrics are being studied as alternatives to SiO_2, they may permit further MOS scaling. The integration of such dielectrics into current device processing may be an extremely difficult task. Unfortunately, most of the current materials, of which Ta_2O_5, TiO_2 and BST seem to be not stable on silicon and tend to form an underlying SiO_x film which reduces their effective capacitance. This path is almost self-defeating unless suitable barrier layer for both interfaces can be found. Although there may be a solution to integrating high-k dielectrics into device processing, it appears that it will be anything but straightforward. It is therefore important to consider the various methods for depositing the gate dielectrics. PVD methods have provided a convenient means to evaluate materials systems for alternate dielectric applications. However the sputter PVD process results in surface damage and thereby creates unwanted interfacial states. Additionally, device morphology inherent to the scaling process generally rules out such line-of-sight PVD deposition approaches. For this reason, CVD and MBE methods have proven to be quite successful in providing uniform coverage over complicated device topologies. Very high-k dielectrics $SrTiO_3$ have been deposited directly on Si using MBE methods [79]. An equivalent oxide thickness of less than 1 nm was reported with dramatic

improvements in transistor performance. More recently, crystalline Y-ZrO_2 has also been examined by MBE methods [84]. However, a manufacturable scaled CMOS process incorporating MBE methods, with the inherent poor throughput relative to present Si-based fabrication operations, remains a clear challenge.

2.2.6 Reliability

A number of different theories have been used to describe the physics of dielectric reliability and to predict the lifetime of MOS devices. For most applications, it is generally accepted that MOS devices are required to work continuously for ten years. Understanding the behavior of oxide breakdown, particularly as a function of the applied bias and temperature, is extremely important for the device lifetime prediction. Recent research indicates reliability limitation to SiO_2 layers at least down to thickness of about 14 Å [84]. Other extrinsic reliability factors, however, such as particles or contaminants, could still yield ultimately poorer oxide reliability. Part of the difficulty in making reliability projections arises from the difference between test conditions and operating conditions. It is clearly not feasible to test individual devices for ten years prior to product incorporation, thus testing must be “accelerated” at higher voltages and temperatures than are actually experienced by typical devices. Making reliability projections from accelerated to actual conditions requires proper scaling for area (from one device area to an entire chip area), voltage, temperature and the failed fraction of devices [85, 86].

Extrapolated leakage current versus gate oxide thickness data from more recent measurement methodology must be adopted for useful comparisons. Much of the understandings for ultrathin oxides have come about only in the past five years, despite decades of research on SiO_2. This suggests that understanding the reliability and failure mechanisms in high dielectric constant materials will require significant effort, especially if any material is to replace SiO_2 within five years, as most roadmaps suggest.

2.2.7 Our considerations of high-k dielectric materials

According to the discussion above, we give a comparison of properties of most commonly studied alternative dielectrics, which is shown in Table 2-2.

For most studied high-k materials, the biggest drawback is that they usually have thermodynamic instability. And many other problems are induced by the thermodynamic instability, such as interface quality, process compatibility, and gate compatibility. Recently, ZrO_2, HfO_2 and Y-stabilized ZrO_2 have received marked attention, mainly because of their relatively large dielectric constant of ~ 20 - 25, and thermal stability up to about 800 ºC. However, it should be pointed out that ZrO_2, HfO_2 and Y-stabilized ZrO_2 have a very loose fluorite structure (as shown in Figure 2-7) and with about 15% oxygen vacant sites makes Y-stabilized ZrO_2 the primary choice for oxygen full cell because large sized O^{2-} ions can easily diffuse to generate the current.

ZrO_2 has been previously reported as having high oxygen diffusivities [59]. The ionic conduction mechanism mainly dominates Y-stabilized ZrO_2 [87]. In this sense, it is impossible for such materials to have low leakage current under applied electric field due to the nature of their open structure, and it is similar in HfO_2.

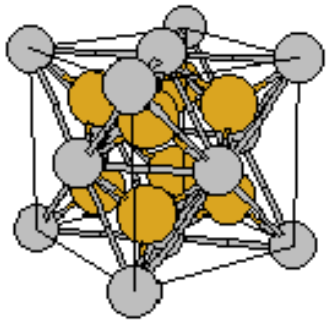

Figure 2-7. Fluorite structure.

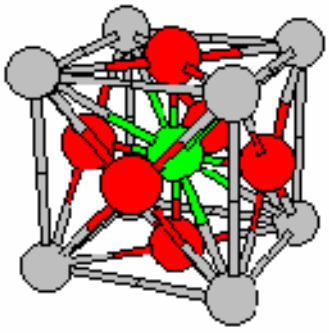

Figure 2-8. Perovskite structure.

High temperature materials particularly zirconates of alkaline earth metals ($SrZrO_3$, $BaZrO_3$, $La_2Zr_2O_7$ and Y-$SrZrO_3$) are currently gaining considerable importance in the field of electrical ceramics [88, 89], refractories [90] and heterogeneous catalysis [91]. Several studies have been reported on the use of calcium zirconate-based systems for monitoring oxygen [7, 8], humidity, hydrogen, hydrocarbons and as a thermistor material [9-13]. $CaZrO_3$ is an orthorhombic *Pbnm* perovskite consisting of slightly deformed ZrO_6 octahedra with Zr-O bond lengths ranging from 2.091(1) to 2.101(1) Å and O-Zr-O angles ranging from 88.0(1)° to 90.9(1)° [92]. The average Zr-O-Zr tilt angle between ZrO_6 octahedra is 146°, compared with 180° of the cubic perovskite

structure. It can be anticipated that zirconates will have a desirable high temperature thermodynamic stability. Perovskite structure (as shown in Figure 2-8) $SrZrO_3$ and $CaZrO_3$ have been reported that their dielectric constant are in the range of 20 ~ 50 [93]. It has been shown that [14] in (Ca, Sr, Ba) zirconate system, the Ca, Sr-rich composition region with orthorhombic perovskite-type structure has high quality factor (2000-3000 at 11 GHz), suitable dielectric constant of 29 ~ 32 and widely adjustable temperature coefficient of dielectric constant (-50 to +50 ppm/ ºC). M. Joseph [94] reported the films of $CaZrO_3$ prepared by pulsed laser deposition (PLD). The observed difference in the stoichiometry of the $CaZrO_3$ films deposited under vacuum and oxygen background was discussed based on the mass spectrometry results. In the view of the leakage current density, the close-packed perovskite structure along with the oxygen ions seems better than the open fluorite structure. Due to their high temperature thermodynamic stability, perovskite structure, high dielectric constant, zirconate materials may be more suitable for the high-k gate application.

2.3 Conduction phenomena in the perovskite thin films

The application of perovskite thin films in electrical engineering and electronics demands exact knowledge on electronic transport processes. The exact control of transport mechanisms in thin films today is part of high reliability of electronic devices. As the thickness of the oxide scaling goes down to a few tens of nanometer, the electrical behaviors of the thin film are different from those of the bulk material,

and the interface with the electrode frequently plays an important role in the electronic transport. Several electrical behaviors have been reported in the literature, such as the Schottky-barrier emission [95-98], Fowler-Nordheim tunneling [99, 100], space-charge limited current [101, 102], and Poole-Frenkel process [103-105].

2.3.1 Schottky barrier emission conduction

An electron to escape into vacuum has to overcome the work function only, if no electric field is applied. This can be realized by thermal activation. When an electric field is applied, the carrier injection from a metal electrode into the bulk dielectric is governed by the Schottky theory [55]:

$$\ln(J/T^2) = \ln A^* + \left\{ \frac{q\left[\sqrt{\frac{qE}{4\pi\varepsilon_0\varepsilon_r}} - \Phi_b\right]}{kT} \right\}, \qquad (2\text{-}4)$$

where A^* denotes the effective Richardson's constant, Φ_b the Schottky barrier height, E the external applied field drop across the depletion layer, ε_0 vacuum permittivity, ε_r dielectric constant. The barrier height Φ_b depends on many parameters, e.g., the work function of metal, barrier lowering by image force, and the surface states. According to equation (2-4) a plot of $\ln(J/T^2)$ versus $E^{1/2}$ gives a straight line. The intercept is the pre-exponential and the slope is the term in bracket. Usually most of the experiments on conduction phenomena of insulator films have been performed

using metal/insulator/metal (MIM) structure. In such a configuration, the MIM structure samples constitute the back to back Schottly diodes，and therefore it is possible to obtain characteristics only of the reverse saturation current by electric biasing the sample. As a result, equation (2-4) is widely used to interpret the variation of J with V and T.

2.3.2 Poole-Frenkel conduction

An electron transferring from a trap to another localized state under the influence of an electric field is known as the Poole-Frenkel effect. The Poole-Frenkel mechanism occurs within the bulk of the dielectric where the barrier between localized states can be lowered due to the influence of the high electric field. For the mechanism to occur the material must have a wide band gap and must have donors or acceptors. Because the localized states of the valence band do not overlap those in the conduction band, the donors or acceptors do not gain enough energy to move into the conduction band or valence band, unlike in normal semiconductors.

Below is the Poole-Frenkle expression from which the current may be calculated for a given electric field. A plot of log J versus $E^{1/2}$ yields a straight line with slope M_{pf} and intercept C_{pf} [106]:

$$J = \left(N_{eff} N_D\right)^{1/2} e\mu \exp\left(-\frac{\Phi_D}{2kT}\right) \exp\left(\frac{e^{3/2} E^{1/2}}{\left(4\pi\varepsilon_0\varepsilon_r\right)^{1/2} kT}\right), \qquad (2\text{-}5)$$

$$M_{pf} = \frac{e^{3/2}}{(4\pi\varepsilon_0\varepsilon_r)^{1/2} kT}, \quad C_{pf} = e\mu \log(N_{eff} N_D)^{1/2}, \tag{2-6}$$

where N_{eff} is the effective density of charge carriers in the conduction band, N_D is the number of donor atoms or molecules per m^3, Φ_D is the barrier height in the absence of the electric field, ε_r represents the dielectric constant.

And as we know that the same plot of log J versus $E^{1/2}$ is also used for determining whether the Schottky emission occurs and to resolve between the two mechanisms we have to apply additional tests. The conduction mechanism generally does not remain the same as the temperature is raised and it is not unusual to find two mechanisms operating simultaneously, though one may predominate over the other depending on the experimental conditions.

2.3.3 Space-charge limited current

Charge injected from the electrode moves through the bulk and eventually reaches the opposite electrode. If the rate of injection is equal to the rate of motion, charges do not accumulate in a region close to the interface and the electrodes are called Ohmic. Ohmic conductors are sources of unlimited number of charge carriers. If the mobility is low which is the normal situation with many materials, then the charges are likely to accumulate in the bulk and the electric field due to the accumulated charge influences the conduction current. A linear relationship between the current and the electrical field does not apply anymore except at very low electric fields. At higher fields the

current increases much faster than the linear one and it may increase as the square or cube of the electric field. This mechanism is usually referred to as space charge limited current (SCLC).

2.4 Sol-gel technique

Conventional solid state reaction of $SrCO_3$ and ZrO_2 requires high temperature calcinations and schedules with intermittent grinding and prolonged duration of calcinations (1200 ºC/48h) for the completion of the diffusion controlled reaction to form $SrZrO_3$ powders. In the same vein, the synthesis of $CaZrO_3$ has been carried out through the solid-state reaction. However, it is difficult to obtain very pure and homogeneous powders using the solid-state reaction route. Therefore, a wet chemical method such as sol-gel was recently developed. From this process, it is expected that (a) homogeneous mixing of Ca, Zr and Sr on an atomic level can be achieved; and (b) sub-micron sized particles can be prepared.

Contemporary sol-gel processing emerged during the 1960s, primarily as a result of specialized requirements for ceramic nuclear fuels [107, 108]. During the past two decades, the demand for advanced ceramics with high purity, homogeneity and well-controlled, tailored properties has led to a renewed interest in the sol-gel technology [109, 110]. Traditionally, the term sol-gel (solution-gelation) was applied to a solution process which initially formed a colloid followed by a gel phase.

Recently the term has been used to include any solution process involving hydrolysis and formation of a gel, irrespective of whether an intermediate colloid is formed. The main advantages inherent in the sol-gel process include:

- Good mixing for multi-component systems;
- Control of particle size, shape and properties;
- Mixing of components at the colloidal (nm) level;
- Since the sol-gel transition is reversible, materials can be recycled and waste minimized.

However, disadvantages include the high cost of alkoxides, large shrinkages during fabrication, and residual carbon and associated porosity. These can be minimized by the appropriate choice of precursor materials.

The sol-gel deposition process involves (1) preparation of a homogeneous solution containing the precursor, usually metal alkoxides; (2) deposition of the solution on the substrate, producing a wet thin film; (3) drying of the film to form an amorphous thin film; and (4) crystallization of the amorphous thin film at elevated temperatures. The first step (preparation of solutions) includes tailoring of solution characteristics, such as viscosity. In the deposition step, pyrolysis and crystallization may be accomplished by a single-step heat treatment. Despite the apparent ease and versatility of the

scheme, the properties of oxides are extremely sensitive to the different conditions of their preparation. Changes in any of the processing steps could potentially affect not only the nature of the species obtained in the subsequent steps, but also the final film microstructure and electrical properties. For instance, the choice of starting chemicals, solvents, solution concentration, as well as handling conditions, solution reactions and firing procedures, can all affect the phase assemblage and the properties of the final material. The most commonly used precursor as the Sr-source is Sr-acetates [Sr $(CH_3COO)_2$]. The commonly used solvent is acetic acid or 2-methoxy ethanol, depending on the precursor. The commonly used zirconium source is a zirconium alkoxide, such as zirconium acetylacetonate [$(CH_3$-$COCH=COCH_3)_4Zr$] or zirconium butoxide [$Zr(OC_4H_9)_4$].

It has been found that the density and microstructure of the samples are greatly influenced by the firing procedure. Dense samples are obtained only when they are fired to a high temperature after each deposition and before another layer is spun on top of the previous one. Also, the drying and baking processes for pyrolizing organics have some effect on the crystallization of the films. The investigation has shown that samples that do not go through drying and baking step usually have poor crystallinity. This is because of the trapping of the organics in the film and their unsuccessful burning, which may inhibit the complete crystallization of the films.

Due to the large delay of Laser-MBE system which can be used directly deposit high-k thin films on Si substrates, and the time constrain in my Ph.D period, I have to deposit and characterize our high-k thin films by using sol-gel technique. It is worth noting that the sol-gel technique can form silicon dioxide on Si substrates easily due to certain amount of H_2O and oxygen in precursor solutions. During the thermal decomposition process, H_2O or oxygenous components reacts with Si substrate, which is similar with the wet oxidation process of SiO_2. J. G. Yoon *et al.* [111] reported the existence of interfacial SiO_2 layer between the Si and MgO when MgO thin films deposited on Si by the sol-gel process. C. R. Cho *et al.* [112] also found a possible silicon dioxide layer of 1-2 nm thickness existed on the Si surface when the sol-gel processed $BaTiO_3$ thin films deposited on Si substrates.

However, for the dielectric of metal insulator metal (MIM) structure capacitors, the sol-gel process is widely used as an easily-controlled method to deposit dielectric thin film with high purity and homogeneity. To our knowledge, there are a few reports on perovskite (Ca, Sr)ZrO_3 thin films for the semiconductor applications. In this thesis, we systematically explore their physical and electrical properties on the platinum-coated Si substrates forming the MIM structure without the formation of interfacial SiO_2 layer particularly at the (Ca, Sr)ZrO_3/bottom electrode by using sol-gel technique.

CHAPTER THREE

EXPERIMENTAL PROCEDURES

The dielectric $Ca_xSr_{1-x}ZrO_3$ thin films prepared by the sol-gel process have been systematically investigated in this study for the high-k microelectronic device applications. The sol-gel derived thin films have been characterized using various measurement methods. In this chapter, the description is given for the detailed experimental procedures: (1) preparation of the $Ca_xSr_{1-x}ZrO_3$ thin films; and (2) characterizations of these $Ca_xSr_{1-x}ZrO_3$ thin films including microstructure, elemental analysis, thermal properties, dielectric and electrical properties.

3.1 Thin film preparation

High temperature materials particularly zirconates of alkaline earth metals are currently gaining considerable importance in the field of electrical ceramics [88, 89], refractories [90] and heterogeneous catalysis [91]. Wet chemical methods via coprecipitation, sol-gel and hydrothermal have been widely used to prepare precursors

with required purity, stoichiometry, physical and chemical characteristics. The sol-gel technique is applied for our thin film deposition due to its good homogeneity, ease of chemical composition control and large area coverage. Four steps are involved in the process: (1) solution preparation, (2) film deposition, (3) low temperature heat treatment for organic pyrolysis, and (4) high temperature annealing for film crystallization.

3.1.1 Solution preparation

The $Ca_xSr_{1-x}ZrO_3$ thin films were prepared by the sol-gel process from the starting raw organic materials of strontium acetate $Sr(CH_3COO)_2$, calcium acetate $Ca(CH_3COO)_2 \cdot H_2O$, zirconium acetylacetone $[CH_3COCH=C(O-)CH_3]_4Zr$ and glacial acetic acid CH_3COOH. The flow chart of the $Ca_xSr_{1-x}ZrO_3$ solution preparation process is shown in Figure 3-1. Strontium acetate or calcium acetate was dissolved in acetic acid first. In order to control the degree of hydrolysis, a solution of zirconium acetylacetonate in acetic acid was added under constant stirring to form Ca-Sr-Zr mixture. The mole ratios of Ca, Sr precursors to Zr were controlled according to the desired composition. A clear solution was obtained after stirring for one hour. It was then mixed for several hours to enhance the homogeneity of the solution. During the mixing, the beaker was sealed with the transparent micro films to prevent further evaporation of water or acetic acid during the mixing.

The thermal properties of synthesized $Ca_xSr_{1-x}ZrO_3$ precursors were analyzed to determine the processing temperatures to deposit thin films. The Perkin-Elmer thermogravimetric analyzer (TGA-7) and differential thermal analyzer (DTA-7) were used for the analysis. The temperature range from room temperature to 1000 °C was chosen and the heating rate was set at 2 °C/min.

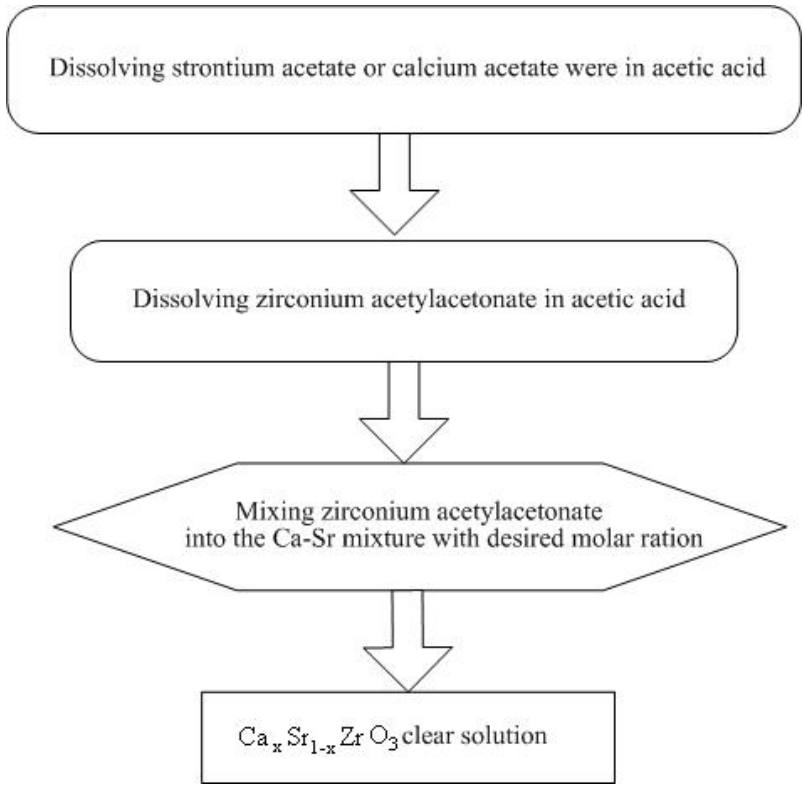

Figure 3-1. The flow chart of $Ca_xSr_{1-x}ZrO_3$ solution preparation process.

The raw chemicals compounds used in this research are listed in Table 3-1.

Table 3-1. Chemicals used for preparation of zirconates solution.

CHEMICAL	FORMULA	MOLAR MASS	PURITY	COMPANY
Strontium acetate	$Sr(CH_3COO)_2$	205.71	>99%	ALDRICH chemical company, Inc.
Calcium acetate	$Ca(CH_3COO)_2 \cdot H_2O$	176.18	>99%	NACALAI TESQUE, Inc.
Zirconium acetylacetone	$[CH_3COCH = C(O-)CH_3]_4Zr$	487.66	98%	NACALAI TESQUE, Inc.
Glacial acetic acid	CH_3COOH	60.05	>99.9%	BEST Chemical CO. (S) PTE LTD

The solutions were filtered into storing amber bottles with 0.1 μm Teflon micropore filter and then aged in a desiccator for 24 to 48 hours.

All the processes described above were carried out on a pre-heated hotplate with continuous stirring using a 10 mm magnetic stirrer.

3.1.2 Deposition of $Ca_xSr_{1-x}ZrO_3$ thin films

(100) single crystal silicon coated with silicon dioxide, Ti, Pt as buffer layer and bottom electrode, was used as the substrate for coating $Ca_xSr_{1-x}ZrO_3$ thin films, and thickness of each layer was 500 nm, 150 nm and 150 nm, respectively. The substrates were soaked in acetone and isopropanol at 80 °C to remove grease, organic contaminants and dust from the substrate surface. Finally the substrates were rinsed with de-ionized water in the dump riser for four cycles and dried with dry nitrogen.

The operation steps are as follows:

1. Place a clean substrate on the platform of the spin coater.
2. Set the heater temperature at 250 °C and 400 °C, respectively.
3. Set the spinning speed and time to 3000 rpm and 40 sec, respectively.
4. Spread the solution on the whole substrate before spinning the substrate.
5. Start the spin coater.
6. Move the as-deposited films quickly to the hot plate and dry for 5 min at 250 °C and 400 °C, respectively.
7. Transfer the dried sample from the hot plate to the sink and wait until it is cooled down to room temperature before another spin coating.
8. Repeat the spin-dry process three to four times to obtain the film with desired thickness.
9. Insert the film in a PC-controlled tube furnace under pure oxygen ambient to anneal the film at the chosen temperature for one hour.
10. Take out the annealed sample after the heat-treatment.

3.2 Fabrication and characterizations of zirconate capacitors

3.2.1 Fabrication of zirconate capacitive device

For the purpose of performing dielectric and electrical measurements, MIM-structured capacitor devices were fabricated and the cross section is shown in Figure 3-2, and the detailed experimental procedure is described as follows:

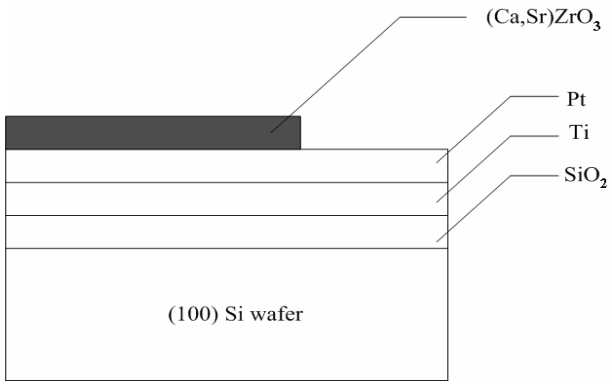

(1) define the window for bottom electrode

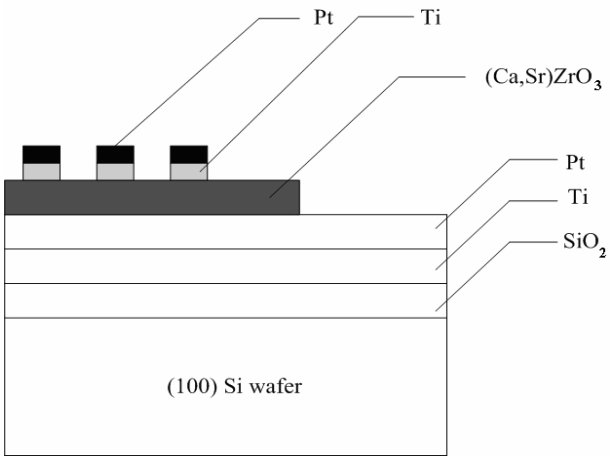

(2) deposit the top electrode

Figure 3-2. The cross section of (Ca, Sr)ZrO_3 thin film capacitors.

In the first step, the top electrode contact windows were defined using the lift-off technique. The windows for the top Pt electrode were defined on patterned photoresist by the image reversal process as illustrated in Figure 3-3.

The photoresist AZ5214 was spin-coated onto $Ca_xSr_{1-x}ZrO_3$ thin film with a spin rate 3000 rpm for 30 seconds. Then the photoresist was soft-baked at 105 °C for 90 seconds. The shadow mask pattern was in a 12×12 square matrix pattern with the cell dimension of 0.3×0.3 mm^2. After aligning the plastic mask and the sample, the top photoresist layer was exposed at the conditions of UV source density 14 mW/cm^2 and exposure time of 4 seconds.

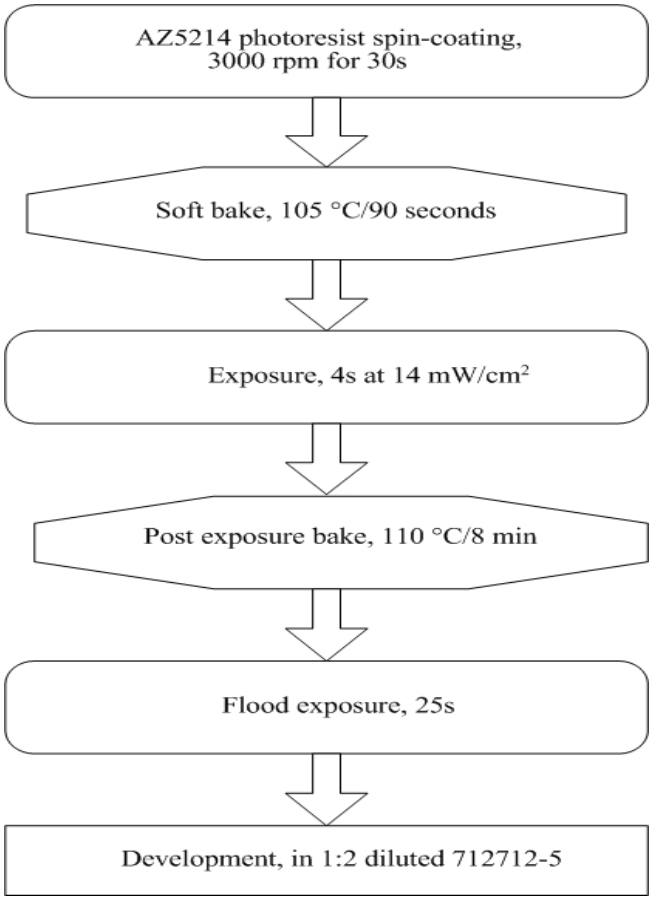

Figure 3-3. The flow chart of the image reversal process for the top electrode window opening.

After that, the image reversal process was carried out by annealing at 110 °C for 8 minutes, and the flood exposure was followed for 25 seconds. Finally the top electrode opening was defined by developing in the 1:2 diluted AZ developer 712712-5 solution. 2 nm of Ti and 200 nm of Pt were deposited onto the $Ca_xSr_{1-x}ZrO_3$ thin films using the RF magnetron sputtering. The sputtering process parameters are summarized in Table 3-2. The top electrode pattern was shown by bathing in acetone to remove the photoresist layer.

Table 3-2. The sputtering parameters of the Pt top electrode.

Target	3-inch Pt metal
Sputtering pressure	15 mTorr (argon 50 sccm)
Sputtering power	120 W
Substrate temperature	No heating
Thickness	200 nm

3.2.2 Characterizations of the physical properties of zirconate films

The structural characterizations of the $Ca_xSr_{1-x}ZrO_3$ thin films were performed using XRD, AFM and SEM. The structure of the $Ca_xSr_{1-x}ZrO_3$ thin films was investigated

by a Siemens D5005 diffractometer with Cu Kα radiation at 40 K*V*/40 mA. The films were scanned in 2θ from 20° to 70° with a sweep rate of 2°/min.

The atomic force microscope (AFM) uses a physical probe raster scanning across the sample using a piezoelectric sample holder controller. A feedback loop is used to maintain a constant interaction between the probe and the sample. The position of the probe and the feedback signal are electronically recorded to produce a three dimensional map of the surface or other information depending on the specialty probe used. Data output is either a three dimensional image of the surface or a line profile with height measurements. The surface roughness parameters of Ra or RMS (root mean square) are also available with either of the above outputs. So, the surface morphology of the $Ca_xSr_{1-x}ZrO_3$ films was imaged in contact mode using AFM.

The scanning electron microscope (SEM) uses a finely focused electron beam scanning across the surface of the sample to generate secondary electrons, backscattered electrons, and characteristic X-rays. These signals are collected by detectors to form images of the sample displayed on a cathode ray tube screen. Then, the cross-section of the thin films was investigated using SEM.

As the electron beam of the SEM is scanned across the sample surface, it generates X-ray fluorescence from the atoms in its path. The energy of each X-ray photon is

characteristic of the element which produces it. The Energy dispersive X-Ray spectroscopy (EDS) microanalysis system collects the X-rays, sorts and plots them by energy, and automatically identifies and labels the elements responsible for the peaks in this energy distribution. Therefore, the composition of the $Ca_xSr_{1-x}ZrO_3$ thin films was roughly estimated by the micro-area EDS analysis.

Infrared spectroscopy is an important technique in determining the bonding vibrations, and it is an easy way to identify the presence of certain functional groups in a molecule. For the purpose of routine organic structure determination, using a battery of spectroscopic methods, the most important absorptions in the infrared region are the simple stretching vibrations. For simple systems, these can be approximated by considering the atoms as point masses, linked by a spring having a force constant *k* and following Hooke's Law. Using this simple approximation, the equation shown below can be utilized to approximate the characteristic stretching frequency (in cm^{-1}) of two atoms of masses m_1 and m_2, linked by a bond with a force constant *k*:

$$\nu = \frac{1}{2\pi c}\sqrt{\frac{k}{\mu}} \quad , \tag{3-1}$$

where $\mu = m_1 m_2 /(m_1 + m_2)$ (termed the reduced mass), and *c* is the velocity of light. The stretching vibrations of typical organic molecules tend to fall within distinct regions of the infrared spectrum, as shown below:

- 3700 - 2500 cm^{-1}: X-H stretching (X = C, N, O, S)

- 2300 - 2000 cm^{-1}: C≡X stretching (X = C or N)
- 1900 - 1500 cm^{-1}: C=X stretching (X = C, N, O)
- 1300 - 800 cm^{-1}: C-X stretching (X = C, N, O)

Since most organic molecules have single bonds, the region below 1500 cm^{-1} can become quite complex and is often referred to as the fingerprint region: that is, if you are dealing with an unknown molecule which has the same fingerprint in this region, that is considered as an evidence that the two molecules may be identical. Therefore, one can use the unique collection of absorption bands to confirm the identity of a pure compound or to detect the presence of specific impurities. Fourier transform infrared (FTIR) spectroscopy was performed using a Perkin-Elmer spectrum 2000 in the wavelength ranges of 3000-400 cm^{-1}. The incident angle of the IR beam to sample surfaces was 60 degree and IR spectra were obtained by the reflected radiation from the surfaces.

Material depth profiling was carried out using JEDL Jamp7800F scanning auger electron microscope. The principal advantages of AES are excellent surface sensitivity (< ~20 Å depth) and high spatial resolution (< 1 μm). Auger electron spectroscopy (AES) is a surface analytical technique that provides information about the chemical composition of surfaces and interfaces. It uses an incident electron beam to excite a solid resulting in the emission of electrons known as auger electrons. An energy

analysis of these auger electrons provides the analytical information for this technique. AES can be used for determining the composition of a surface, mapping the spatial distribution of the surface constituents, and obtaining a depth profile of these constituents into the bulk of the material.

X-ray photoelectron spectroscopy (XPS) provides chemical state information for compound identification. X-ray photoelectron spectroscopy (XPS, also called electron spectroscopy for chemical analysis, ESCA) is an electron spectroscopic method that uses X-rays to knock electrons out of inner-shell orbital. The kinetic energy (E_K) of these photoelectrons is determined by the energy of the X-ray radiation ($h\nu$) and the electron binding energy (E_b) as given by:

$$E_K = h\nu - E_b. \tag{3-2}$$

The result can also be expressed by the following equation:

$$A + h\nu \rightarrow A^{+*} + e - E_K, \tag{3-3}$$

where A^{+*} is an excited ionized atom.

Equation (3-2) shows the kinetic energy of the electrons is dependent on the binding energy. The electron binding energies are dependent on the chemical environment of the atom. XPS is therefore useful to identify the oxidation state and ligands of an atom.

The measurements of dielectric and electrical properties were carried out on a Mitutoyo vibration-proof microprobing station. Platinum top electrodes of 0.3×0.3 mm^2 areas were sputtered and patterned by the lift-off technique. Capacitance (*C*) and leakage current density (*J*) were measured by a HP 4284A LCR meter and a HP 4155B semiconductor parameter analyzer, respectively.

CHAPTER FOUR

PROPERTIES OF SOL-GEL DERIVED $Ca_xSr_{1-x}ZrO_3$ THIN FILMS

Aggressive dimension scaling of semiconductor devices requires the conventional gate dielectric thickness must also decrease to maintain a given storage capacitance to reduce the short-channel effects and to keep device drive current at an acceptable level. Since direct tunneling increases exponentially with decreasing oxide thickness, continuous scaling of thermal silicon oxide as the gate dielectric has run into difficulties when the oxide thickness is less than 20 Å [6]. The evolving decrease of the gate dielectric film thickness to an oxide-equivalent value of 10 Å is identified as a critical front-end technology issue in the Semiconductor Industry Association's (SIA's) ITRS. A suitable replacement gate dielectric with a high permittivity must exhibit low leakage current, compatibility with CMOS process flow, and exhibit at least the same equivalent capacitance, performance and reliability of silicon oxide. In recent years metal oxides with the ABO_3 perovskite structure are of fundamental

interest and significance, as their properties may be tailored to specific applications by subtle changes in chemical doping at A or B cation sites. Perovskite oxides have received great attention recently as high-temperature proton conductors [7, 8, 93]. Alkaline-earth zirconates (such as $CaZrO_3$) are in general chemically stable and have high dielectric constant. Due to its high relative permittivity and low leakage current compared to other dielectric materials, the solid perovskite phase $Ca_xSr_{1-x}ZrO_3$ may be one of the promising candidates for use as an alternative dielectric material replacing the conventional silicon oxide in advanced CMOS technologies, and in other integrated capacitor applications. Despite recent structural and synthesis studies [9, 94], there is still a lack of the fundamental understanding of the effects of cation doping in this system.

In this chapter, we systematically investigate the preparation of $Ca_xSr_{1-x}ZrO_3$ thin films by using sol-gel wet chemical technology. The calcination behavior was studied by using differential thermal analysis (DTA) and thermogravimetric analysis (TGA). The influence of the processing parameters on the structure and dielectric properties of the $Ca_xSr_{1-x}ZrO_3$ thin films was investigated by using X-ray diffraction (XRD), atomic force microscope (AFM), scanning electron microscope (SEM), and dielectric property measurements.

This chapter is divided into five sections. The first section discusses the thermal properties of the $Ca_xSr_{1-x}ZrO_3$ precursors. Next, the studies on the influence of deposition parameters for the microstructure evolution of sol-gel derived $Ca_xSr_{1-x}ZrO_3$ thin films are presented in the second section. Then, the changes in the chemical structure and oxide growth during the exposure are investigated by the Fourier transform infrared (FTIR) spectroscopy. Next, the studies on the dielectric properties of the sol-gel derived $Ca_xSr_{1-x}ZrO_3$ thin films as a correlation to their microstructure are presented. A dielectric mechanism discussion is given based on the above data for further understanding. Lastly, the sol-gel derived ZrO_2 properties have been systematically investigated for the comparison with the $Ca_xSr_{1-x}ZrO_3$ system. The $Ca_xSr_{1-x}ZrO_3$ system shows better properties than those of ZrO_2, indicating its potential in high-k microelectronic device applications.

4.1 Thermal properties of sol-gel derived $Ca_xSr_{1-x}ZrO_3$ thin films

In order to provide an indication of suitable heat-treatment schedules for eliminating organic components from the film deposited from the solution, the calcination behavior was studied at temperatures up to 1000 ºC using DTA and TGA technique at a heating rate of 2 ºC/min to distinguish the low-temperature reaction steps. The complex was heated in a crucible and a couple of Pt-Pt/10%Rh thermocouples was used to register the temperature. For the DTA analysis, Al_2O_3 powder was used as a reference.

Sol-gel method to prepare $CaZrO_3$ fine powders from calcium carbonate and zirconium oxychloride octahydrate in a dilute alkaline $(NH_4)_2C_2O_4 \bullet H_2O$ solution with diammonium oxalate monohydrate as complexing agent was reported [113]. Our method is based on the preparation of an acetate precursor solution of Ca- and Zr-compounds in stoichiometric amounts in acetic acid and subsequent calcinations to an oxidic perovskite phase. From this process, it is expected that homogeneous mixing of Ca and Zr on an atomic level can be achieved.

Figure 4-1 shows the typical DTA and TGA curves for the dried 0.2M $CaZrO_3$ (x=1) (a) and $SrZrO_3$ (x=0) (b) precursors. It can be seen from Figure 4-1 (a) that the endothermic peaks at 56 ºC and 180 ºC in the dried $CaZrO_3$ precursor DTA curve are due to the evaporation of adsorbed water and solvents. The exothermic peak at 378 ºC is ascribed to the decomposition of the acetate complexes to carbonates. This decomposition causes a continuous decrease in sample weight in this temperature region. At 675 ºC, an endothermic peak is found and attributed to the decomposition of the carbonates to oxides, accompanied by the loss of CO_2, *i.e.* reaction (4-1).

$$CO_3^{2-} \rightarrow O^{2-}(oxide) + CO_2 \uparrow \quad . \qquad (4\text{-}1)$$

It can be seen that the crystallization temperature for the $CaZrO_3$ perovskite phase is relatively high. At temperature above 700 ºC, the TGA result shows a flat curve, approximately 39 wt% of inorganic residue remained from the fabricated precursor as shown in TGA curve.

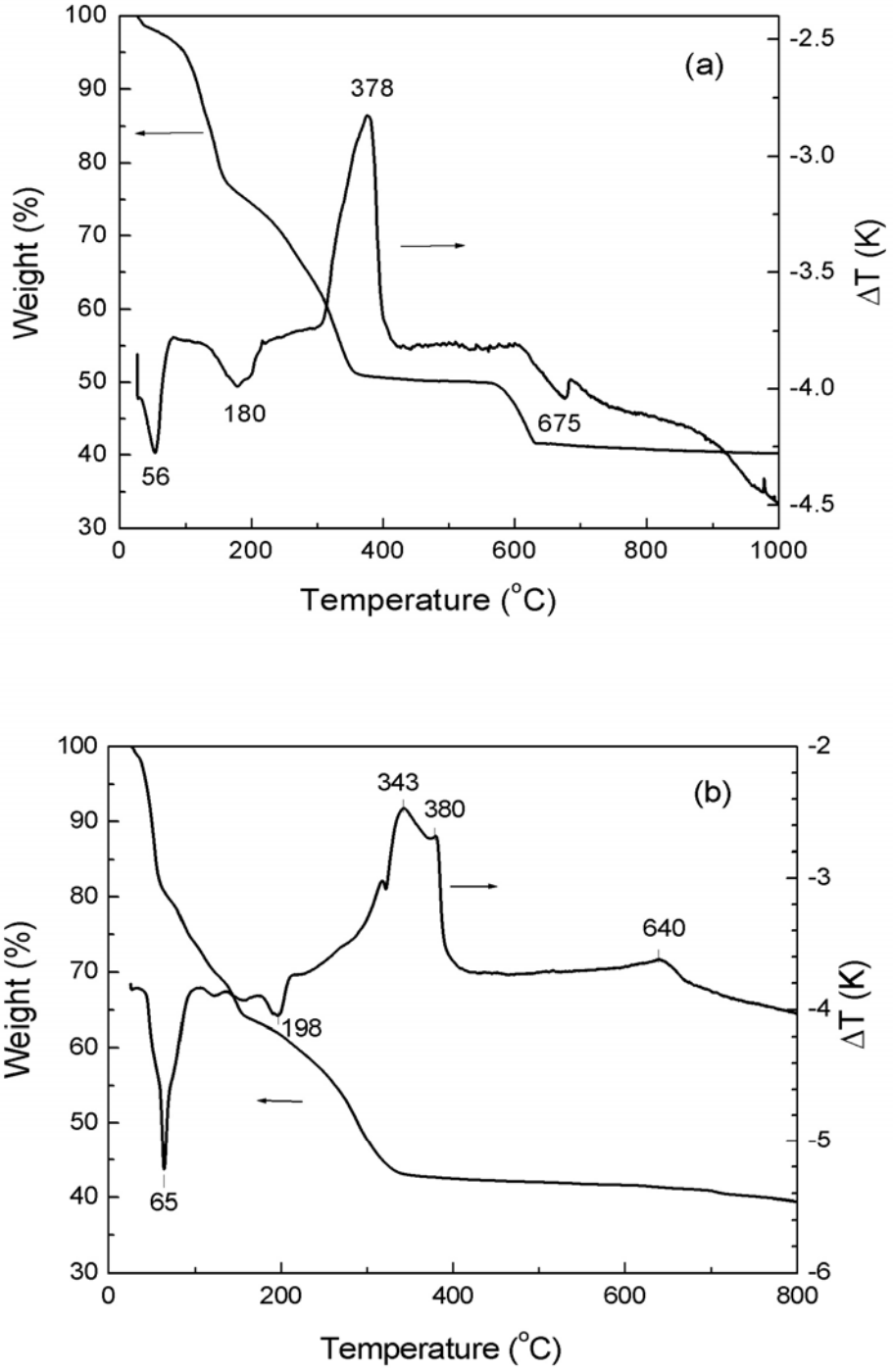

Figure 4-1. DTA and TGA curves of (a) $CaZrO_3$ (x=1) precursor and (b) $SrZrO_3$ (x=0) precursor at a heating rate of 2 ºC/min in air.

Figure 4-1 (b) shows in the temperature range of 50 ~ 300 ºC, the dried $SrZrO_3$ precursor DTA curve shows two main endothermic peaks at 65 and 198 ºC. The TGA curve presents marked weight losses in this temperature region, which is consistent with the DTA result. By combining these two curves, the DTA peaks in this temperature range can be attributed to the evaporation of solvent as well as decomposition of organics. The TGA curve shows about 57 wt% of weight in the sample below 250 ºC.

In the temperature range of 300 ~ 650 ºC, several exothermic peaks are observed in the DTA curve of the sample. In this region, the samples present a less abrupt weight loss. The exothermic peak and corresponding weight loss at 343 ºC are due to the oxidation of residual organics and the de-carbonization of $SrCO_3$. There is almost no weight loss observed above 350 ºC, indicating that the organic components and hydrates are almost removed completely around the temperature range of 300 ~ 350 ºC. The other two exothermic peaks at 380 and 640 ºC are attributed to the glass formation and perovskite phase crystallization temperature, respectively. Potdar *et al.* [114] also found these similar thermal properties in sol-gel derived $SrZrO_3$ precursor.

At temperature above 650 ºC, according to the DTA and TGA results, the chemical reaction is complete. Approximately 38 wt% of inorganic residue remained from the fabricated precursor as shown in the TGA curve.

Samples with other doping composition show similar thermal properties as those of the two basic precursors, as shown in Figure 4-2. It can be easily seen that the step height of weight loss in the temperature range of 600 ~ 700 ºC decreases gradually with the decrease of Ca content due to the decrease in calcium carbonate.

According to the thermal analysis, two pre-heating temperatures at 250 ºC and 400 ºC were chosen to eliminate the organic components from the as coated film during the process of deposition of $Ca_xSr_{1-x}ZrO_3$ thin films.

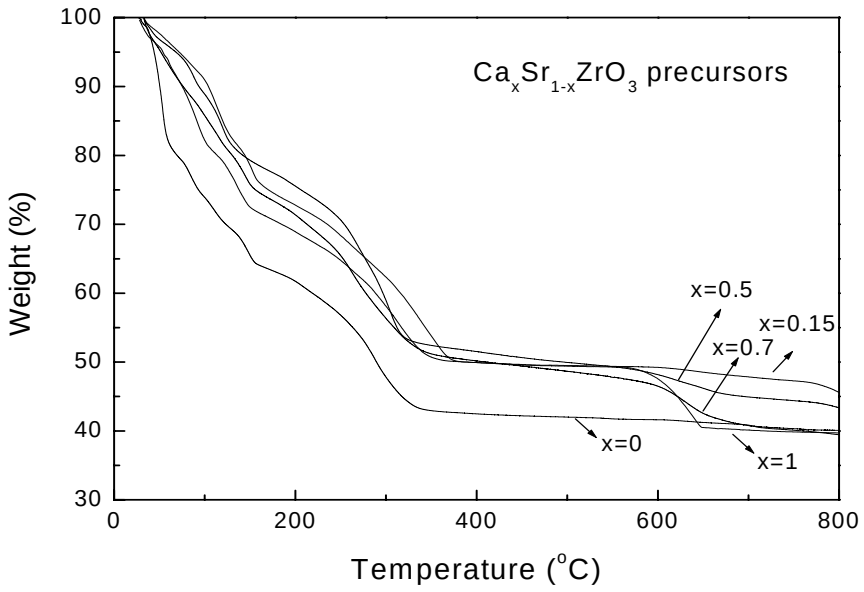

Figure 4-2. TGA curves of $Ca_xSr_{1-x}ZrO_3$ precursors at a heating rate of 2 ºC/min in air.

4.2 Structural and elemental analysis of sol-gel derived $Ca_xSr_{1-x}ZrO_3$ thin films

Some physical properties of the sol-gel derived $Ca_xSr_{1-x}ZrO_3$ thin films, which is related to the experimental process conditions, was studied using XRD, AFM, SEM and XPS techniques. These serve to provide better understandings of the structure, dielectric, and electrical properties that are important for high-k device applications.

4.2.1 X-ray diffraction

XRD analysis was used to obtain information on the different phases present in the calcined powder or annealed thin films at temperatures between 150 ºC and 1000 ºC. The experiments were carried out using a Siemens D5005 diffractometor with Cu Kα radiation (λ=1.5406Å) at 40 k*V*/40 mA. The scanning range was from 20º to 70º in 2θ with a scan rate of 2º/min. A small glancing angle fixed at 1º was used to ensure that the diffraction intensity mostly came from the measured thin films. The JCPDS files were used for the analysis of all XRD results.

The XRD spectra taken after calcining the $SrZrO_3$ precursor at 150 (1h) (drying), 450 (3h), 1000 ºC (5h) and 1000 ºC (10h) are presented in Figure 4-3. All peaks with # mark observed for the dried precursor can be attributed to strontium acetate ($C_4H_6SrO_4$). If the precursor is calcined at 450 ºC, the strontium acetate complex decomposes to $SrCO_3$, confirming the experimental results from TGA and DTA measurements. If the precipitated precursor is calcined at 1000 ºC, the solid-state

reactions progress even further towards the formation of desired $SrZrO_3$ phase, as shown in Figure 4-3 of the XRD pattern obtained in the curve for 5h at 1000 ºC. If the precursor is calcined at 1000 ºC for 10h, it can be easily seen that the XRD peaks of the $SrZrO_3$ perovskite phase have increased in intensity.

Figure 4-4 shows the XRD spectra taken after calcining the $CaZrO_3$ precursor at 150 (1h) (drying), 450 (3h), 800 (3h), 1000 ºC (5h) and 1000 ºC (10h). All peaks with ♦ mark observed for the dried precursor can be attributed to calcium acetate ($C_4H_6CaO_4$). When the annealing temperature is up to 450 ºC, the calcium acetate complex decomposes to $CaCO_3$, which is in agreement with the experimental results from the TGA-DTA measurements. In the precursor calcined at 800 ºC, two different phases are identified, a $CaZrO_3$ perovskite phase and a $CaZr_4O_9$ cubic phase. Several authors have reported the coexistence of a $CaZrO_3$ perovskite and a $CaZr_4O_9$ cubic phase in the CaO-ZrO_2 system at temperatures up to 1300 ºC with CaO concentrations between 20 and 50 mol% [115-117]. The observed mixture of different binary oxides confirms the results obtained from the temperature-programmed TGA and DTA analysis. If the precipitated precursor is calcined at 1000 ºC, then the solid-state reactions progress even further towards the formation of the desired $CaZrO_3$ perovskite phase, as shown in Figure 4-4 of the XRD pattern obtained after calcining the precursor for 5h at 1000 ºC. It can be easily seen that the XRD peaks of the $CaZrO_3$ perovskite phase

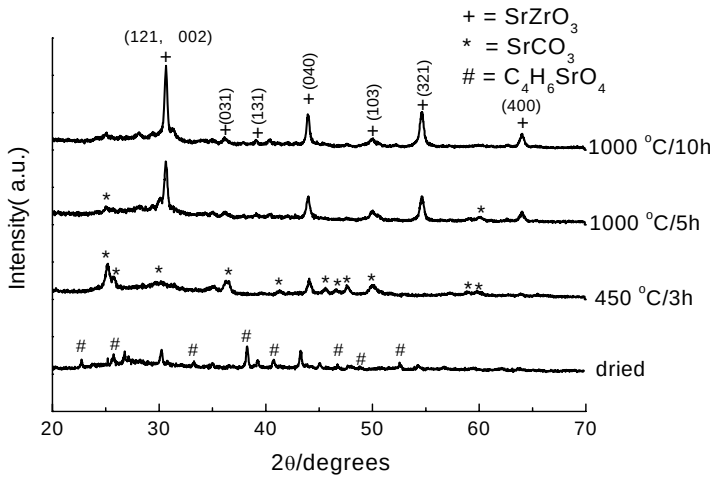

Figure 4-3. XRD patterns of $Ca_xSr_{1-x}ZrO_3$ (x=0) precursor calcined at different temperatures between 150 and 1000 °C.

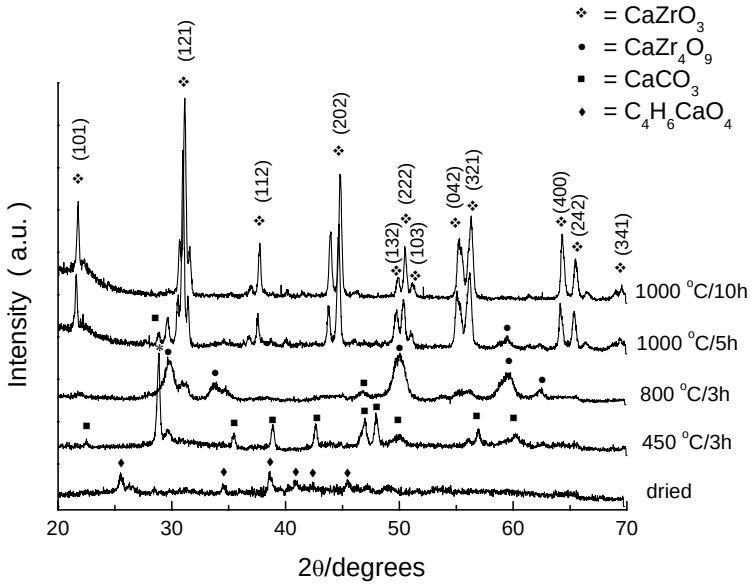

Figure 4-4. XRD patterns of $Ca_xSr_{1-x}ZrO_3$ (x=1) precursor calcined at different temperatures between 150 and 1000 °C.

have increased in intensity. The intensity of the $CaZr_4O_9$ phase has decreased dramatically, indicating a substantial decrease in the amount of this phase. If the precursor is calcined at 1000 ºC for 10h, the conversion to $CaZrO_3$ phase progresses further and the $CaZr_4O_9$ phase nearly cannot be detected. In other words, the cubic $CaZr_4O_9$ phase reacts with CaO to form stoichiometric $CaZrO_3$ phase.

Hence, the reaction scheme can be given as follows:

$$\text{Precursor} \xrightarrow{150^\circ C} Ca(CH_3COO)_2 + \text{Amorphous zirconia}$$

$$\xrightarrow{450^\circ C} CaCO_3 + \text{Amorphous zirconia}$$

$$\xrightarrow{800^\circ C} CaZr_4O_9 + CaCO_3 + CaZrO_3$$

$$\xrightarrow{1000^\circ C / 5h} CaZr_4O_9 + CaZrO_3$$

$$\xrightarrow{1000^\circ C / 10h} CaZrO_3$$

It has been found that varying the calcinations temperature leads to different phases in the bulk materials. The desired perovskite $CaZrO_3$ is formed as the calcination temperature increases to 1000 ºC.

Figure 4-5 shows the XRD patterns for $Ca_xSr_{1-x}ZrO_3$ (x=0) thin films prepared on $Pt/Ti/SiO_2/Si$ substrate and annealed at different temperatures for 1h in flowing oxygen. It is clearly shown that the film annealed at 550 ºC has an amorphous structure; while the film annealed at 600 ºC, which is just slightly below the crystallization temperature, it crystallizes into the polycrystalline perovskite phase of

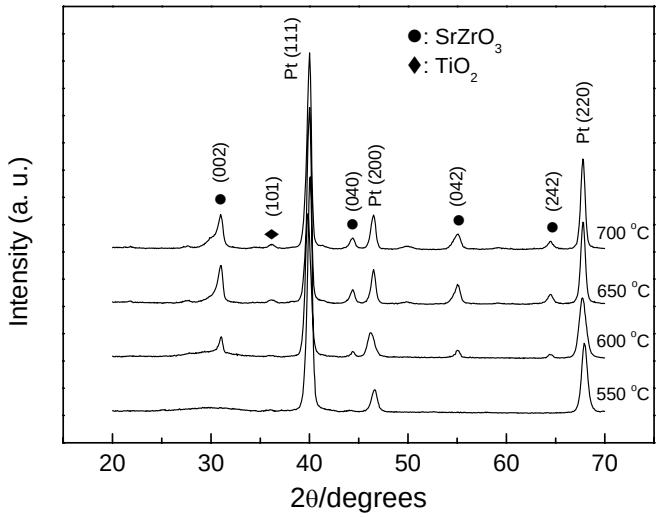

Figure 4-5. XRD patterns of $Ca_xSr_{1-x}ZrO_3$ (x=0) films prepared on $Pt/Ti/SiO_2/Si$ substrates annealed at different temperatures in O_2 for 1h.

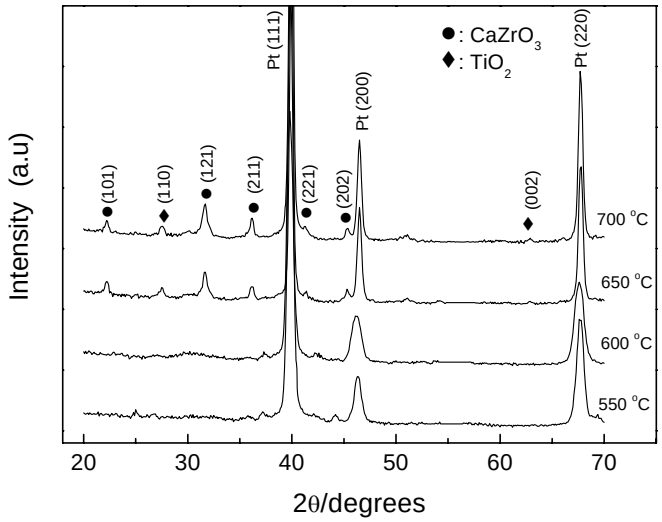

Figure 4-6. XRD patterns of $Ca_xSr_{1-x}ZrO_3$ (x=1) films prepared on $Pt/Ti/SiO_2/Si$ substrates annealed at different temperatures in O_2 for 1h.

$SrZrO_3$. With further increase in annealing temperatures, the intensity of the diffracted peaks is further increased, showing an increased crystallinity of the film. XRD results show those films annealed at 650 and 700 ºC have polycrystalline structure. However, as the thickness of the present films is small (~140 nm) and the grain size is of the order of tens of nanometers, the peaks are broad.

Figure 4-6 shows the XRD patterns of $Ca_xSr_{1-x}ZrO_3$ (x=1) thin films prepared on $Pt/Ti/SiO_2/Si$ substrate and annealed at a series of temperatures of 550, 600, 650 ºC and 700 ºC for 1h in flowing oxygen. The XRD result of the film annealed at 550 °C, which is much lower than the crystallization temperature, indicates that the film has its amorphous structure. It seems that $CaZrO_3$ film begins to crystallize at 600 °C.

Since decomposition temperature given by TGA analyses on powder samples are higher than the one observed in thin films, the role of electrode material and film thickness on the film decomposition and phase formation behavior should be considered. It reveals that the Pt surface can enhance the hetero-nucleation and the growth of the $CaZrO_3$ film, and this phenomenon was observed for other materials annealing on Pt coated substrates [118, 119]. Moreover, the faster decomposition kinetics showed by thin films deposited on Pt could be attributed to the catalytic effect of the substrate as well as to different kinetics between films and bulks [120]. With further increase in annealing temperatures, the intensity of perovskite $CaZrO_3$ phase is

increased, indicating that further crystallization progresses in $CaZrO_3$ thin films. Meanwhile, it is worth to note that with the increase of annealing temperature above 600 °C, the diffraction peaks of TiO_2 appear which is caused by the inter diffusion of the Pt/Ti bottom electrode [121]. Nam *et al*. [122] reported that when the Pt/Ti substrates were annealed in oxygen environment, titanium oxide was formed along Pt grain boundary.

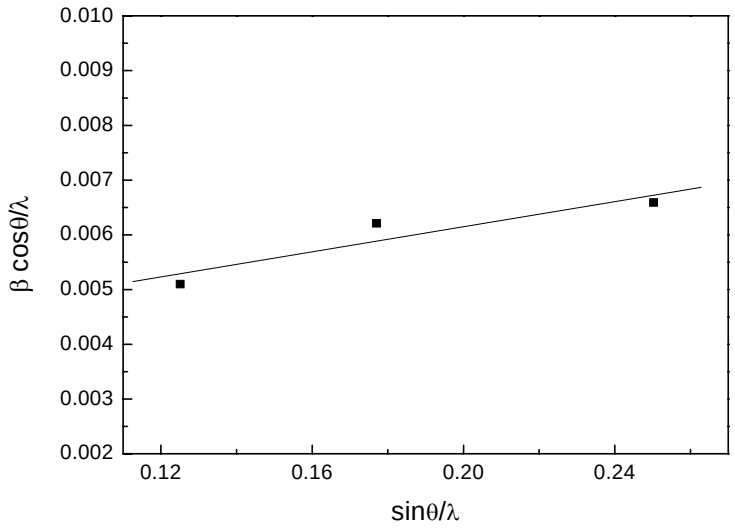

Figure 4-7. Plot to determine strain and particle size of $CaZrO_3$ thin films annealed at 700 °C. Data obtained from XRD pattern.

The information on strain and the particle size is obtained from the full-width-at-half-maximum (FWHM) of the diffraction peaks. The FWHM's (β's) can be expressed as a linear combination of the contributions of the strain (σ) and particle size (L) through the following relation [123]:

$$\beta \cos\theta / \lambda = 1/L + \sigma \sin\theta / \lambda . \quad (4\text{-}2)$$

Figure 4-7 represents the plot of $\beta \cos\theta / \lambda$ vs. $\sin\theta / \lambda$ for $CaZrO_3$ thin films annealed at 700 °C. The slope of the line gives the amount of strain which comes out to be 1.146×10^{-2} and the intercept on y-axis gives the particle size as ~ 26 nm.

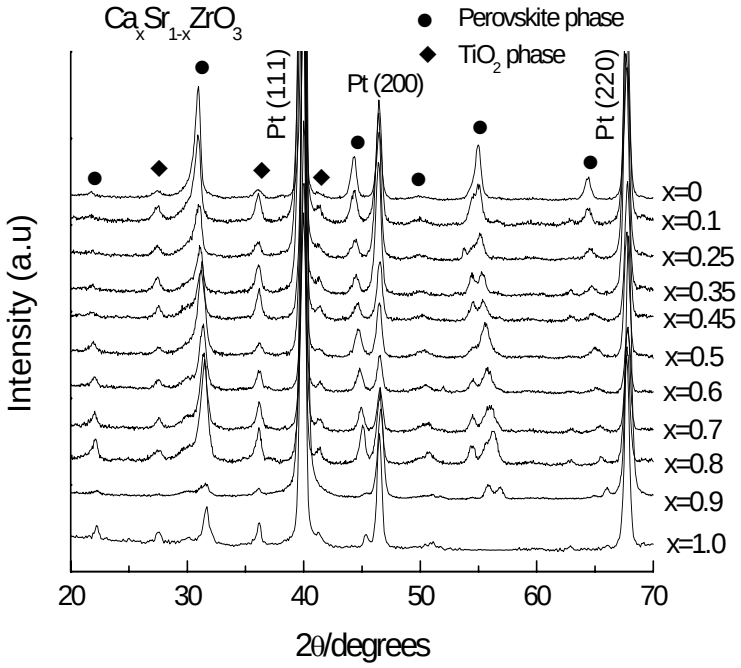

Figure 4-8. XRD patterns of $Ca_xSr_{1-x}ZrO_3$ ($0 \le x \le 1$) thin films annealed at 700 ºC.

Figure 4-8 shows the systematic XRD patterns of $Ca_xSr_{1-x}ZrO_3$ ($0 \le x \le 1$) thin films annealed at 700 ºC. It is evident that the XRD profiles of $Ca_xSr_{1-x}ZrO_3$ change systematically with composition x. The strongest diffraction peak of the perovskite phase shifts to the higher degree from $SrZrO_3$ (x=0) to $CaZrO_3$ (x=1). This is due to the lattice contraction as Sr is replaced by Ca with a smaller ionic radius in

$Ca_xSr_{1-x}ZrO_3$ thin films. The XRD profiles of each end member $SrZrO_3$ or $CaZrO_3$ can be indexed as an orthorhombic unit cell. The lattice parameters are determined to be a = 5.879 Å, b = 8.147 Å and c = 5.769 Å for $SrZrO_3$ phase (JCPDS 10-0268), and a = 5.642 Å, b = 7.970 Å and c = 5.650 Å for $CaZrO_3$ phase (JCPDS 35-0790). It can also be seen that the peaks associated with the TiO_2 phase remain constant when the composition x changes.

4.2.2 EDX measurements

The obtained molar cation ratios in the films were determined using Energy Dispersive X-ray Microanalysis (EDX) methods. The electron accelerating voltage is 10 K*V*.

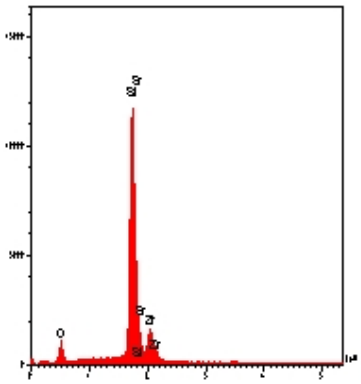

Elt	XRay	Int	Error	K	Kratio	W%	A%
O	Ka	388.0	3.5962	0.1178	0.0920	22.91	44.28
Si	Ka	3730.3	11.1510	0.4785	0.3737	38.44	42.33
Sr	La	941.8	5.6030	0.2395	0.1871	20.61	7.27
Zr	La	586.8	4.4228	0.1642	0.1282	18.04	6.12
				1.0000	0.7810	100.00	100.00

Figure 4-9. EDX spectra of $SrZrO_3$ thin film deposited on the silicon substrate annealed at 700 ºC in O_2.

Figure 4-9 shows the typical EDX spectra of the $SrZrO_3$ thin film deposited on the silicon substrate followed by a post-annealing in O_2 at 700 ºC. The film deposited on the silicon substrate was investigated in order to ensure that the Zr emission line was not influenced by contributions originating from the Pt coated silicon substrate. The result indicates that the ratio of Sr:Zr is 1:0.84, which is close to the stoichiometry of precursor.

Table 4-1. Calculated and measured cation ratios for the sol-gel syntheses.

Film compositions (x) $Ca_xSr_{1-x}ZrO_3$	molar cation ratio(Ca:Sr) (mol%) (x/1-x)		measured film compositions (x)
	stoichiometric	measure	
0.05	0.053	0.069	0.065
0.15	0.176	0.207	0.171
0.35	0.538	0.565	0.361
0.45	0.818	0.813	0.448
0.5	1	1	0.5
0.6	1.5	1.428	0.588
0.7	2.333	2.239	0.691
0.8	4	3.77	0.790
0.9	9	7.532	0.88

Table 4-1 gives the calculated calcium and strontium ratios from the EDX spectra after the films annealed at 700 ºC for 1h in O_2 ambient. The element ratios can be roughly compared with the values of the stoichiometric ratios. Actually, EDX is not a preferred mode for precise composition determination and AES may be the best method to detect the quantitative elemental composition of the thin film. The AES

result of the $CaZrO_3$ film indicates that the ratio of Ca:Zr is 1:1.1, which is close to the stoichiometry of precursor. Unfortunately, due to the lack of the standard calibration data of strontium element of the AES equipment, further precise composition analysis for $Ca_xSr_{1-x}ZrO_3$ system cannot be measured at present.

4.2.3 Surface morphology

The microstructure such as grain size is an important parameter determining the dielectric and electrical properties of thin films. Atomic force microscopy (AFM) measurement was performed to study the surface morphology and microstructure development of the sol-gel derived $Ca_xSr_{1-x}ZrO_3$ films as a function of the annealing temperature. Typically, we investigated the surface morphology of $SrZrO_3$ (x=0) thin films using contact-AFM measurement, and the cross-sectional image of $CaZrO_3$ (x=1) thin film was indicated by scanning electron microscopy (SEM).

The surface roughness evolution of $SrZrO_3$ thin films is listed in Table 4-2.

Table 4-2. The surface root mean square roughness corresponding to the annealing temperatures.

Annealing temperature (ºC)	550	600	650
Root mean square roughness (Å)	16.1	23.6	80.9

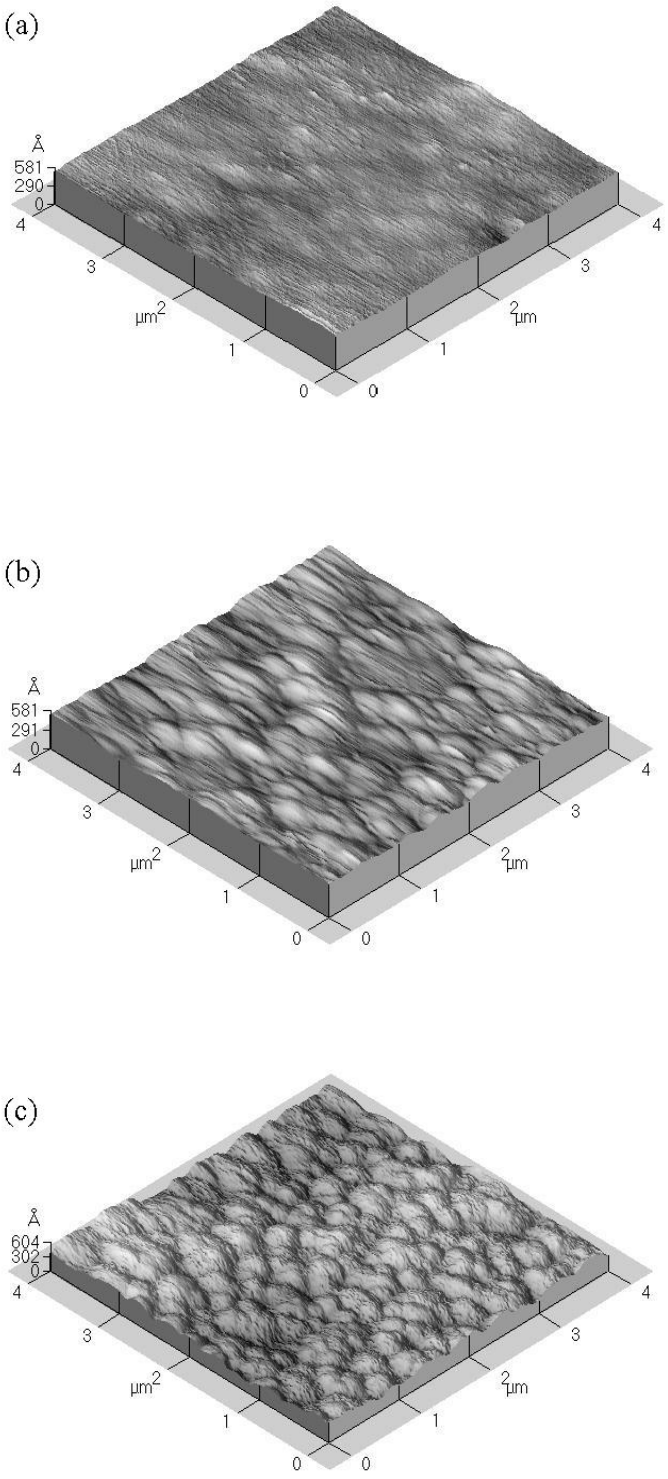

Figure 4-10. AFM images of $SrZrO_3$ thin films annealed in O_2 at (a) 550 ºC, (b) 600 ºC, (c) 650 ºC.

Figure 4-10 shows the AFM images of $SrZrO_3$ thin films annealed at different temperatures with the scanning area of 4×4 μm^2. It is evident that when annealed at 550 ºC, the sample shows a homogeneous surface morphology with low roughness. It agrees with the XRD results that the sample has its amorphous structure annealed at low temperature. When the sample was annealed at 600 ºC and 650 ºC, the increased RMS (root mean square) roughness indicates that the material's structure becomes increasingly ordered. In addition, their grain size increases with the increase in annealing temperature, as shown in Figures 4-10 (b) and (c). At this stage of growth, coalescence of nuclei occurs, with the formation of granular structures resulting in a significant increase of roughness. This result is in agreement with the XRD analysis where annealing at high temperatures results in a high degree of crystallization.

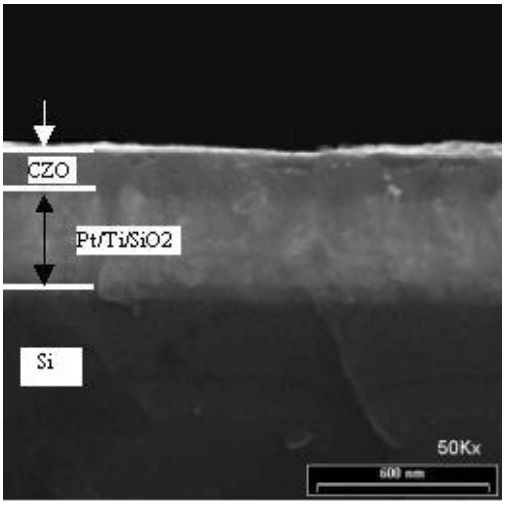

Figure 4-11. The cross-sectional image of $CaZrO_3$ (CZO) thin film deposited on $Pt/Ti/SiO_2/Si$ substrate annealed at 600 °C for 1h in O_2.

Figure 4-11 shows a typical cross-sectional image of $CaZrO_3$ thin film annealed at 600 °C. The thickness of the film is about 140 nm.

4.2.4 X-ray photoelectron spectroscopy

X-ray photoelectron spectroscopy (XPS) is an analytical spectroscopy which is used to determine the oxidation state or chemical environment and to quantify elements in the surface region [124]. This technique uses low power X-rays to excite surface atoms which then emit photoelectrons. The resultant spectrum of photoelectron energy versus intensity has peaks with energies which are characteristic of the element and the orbital from which the electron is emitted. In losing an electron, the atom, and by extrapolation the analyte, becomes positively charged. If the analyte is a metal, charge neutralization can be achieved by earthing, but in the case of semiconductors and insulators, sample charging is a problem. Various charge neutralization techniques can be used but total control of the process cannot always be accomplished and a small correction to the photoelectron energy has to be applied [125].

Correcting the photoelectron energy is referred to as charge referencing and the procedure depends on being able to identify a feature in the photoelectron energy spectrum for which the exact energy in an uncharged state is known. The difference between the charged and uncharged position is the amount of charge which can be subtracted from all the other photoelectron peaks to give their true positions. Many

charge referencing methods have been applied with varying degrees of success. The preferred method is to use an internal reference. The most widely applied method is to use the C1s peak arising from adsorbed hydrocarbon contamination [124], since C always contaminates any material surface. This contamination originates from airborne sources and is a common feature in all X-ray photoelectron spectra of samples that have been exposed to air.

Metal oxides exhibit wide variations in their electron transfer properties, surface redox potentials and surface acidities. However, an ambiguity can remain since the chemical C species depend on both the nature of the specimen and its treatment before analysis [126]. In XPS studies of oxide compounds, the authors have noted significant variation in the reported C1s spectra [127]. Both the position and the shape of the C1s peak change according to the preparation method and the subsequent sample history, such as calcinations and reduction; however, the complexity of the peak shape makes it difficult to unequivocally assign the C1s peak position to a known hydrocarbon with a well defined binding energy. This introduces a degree of uncertainty when attempting to compare the spectra from different samples. So, XPS performed on insulating materials suffers from artifacts due to the electrical charge accumulation in the probed surface. In this study, O1s charge referencing is shown to be successful in mixed oxides.

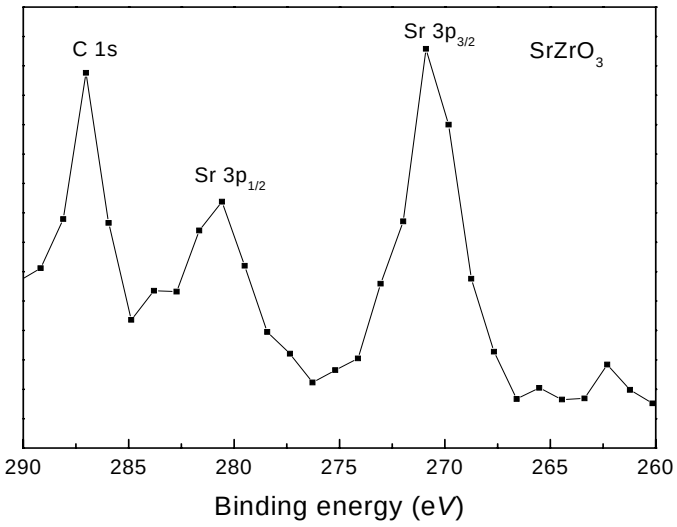

Figure 4-12. XPS spectra of $SrZrO_3$ thin film annealed at 700 °C for 1h in wide-scan mode in the energy range of 290 ~ 260 e*V*.

Figure 4-12 shows the XPS spectra of $SrZrO_3$ thin film annealed at 700 °C for 1h in wide-scan mode in the energy range of 290 ~ 260 e*V*. It is found that C1s peak is very close to the $Sr3p_{1/2}$ peak. To overcome these difficulties, Werrett *et al.* have proposed to reference the XPS spectra of some oxides (including ZrO_2) by using the O1s line for which the energy is precisely known from measurements on ultra-thin films deposited on metallic substrates [128, 129].

Using the O1s binding energies obtained from thin film data of zirconia 531.2 e*V* [130], the XPS spectra of $SrZrO_3$ (x=0) thin film annealed at 700 °C for 1h in wide-scan mode in the energy range of 1100 ~ 0 e*V* have been replotted in Figure 4-13.

It shows the $SrZrO_3$ phase in agreement with the XRD results discussed before. The strategy of O1s referencing is found to be useful in interpreting the XPS of mixed metal oxides.

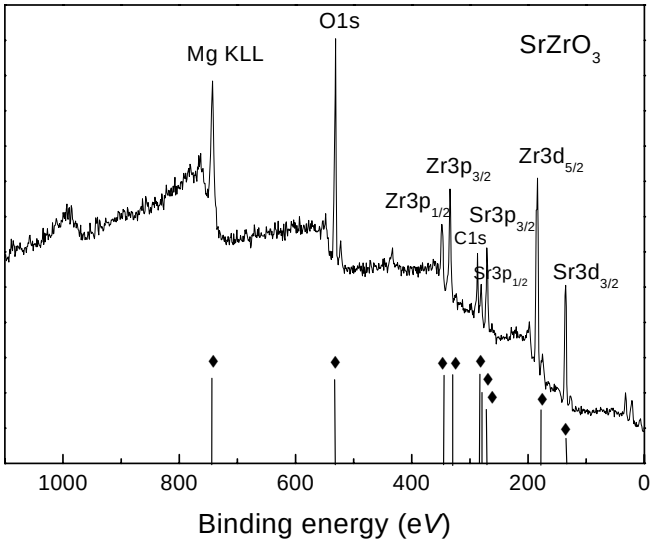

Figure 4-13. XPS spectra of $SrZrO_3$ thin film annealed at 700 °C for 1h in wide-scan mode in the energy range of 1100 ~ 0 e*V*.

The O1s, Ca2p, Zr3d and C1s lines are shown in Figure 4-14 (a, b, c, d) respectively for $CaZrO_3$ thin film annealed at 700 °C. For each line the best fit is also drawn, taking into account for a Gaussian shape added to a linear base-line. The fit parameters (binding energy and full width at half maximum FWHM) are given in Table 4-3. As well in the decomposition of the O1s spectrum into 2 lines, one is attributed to Zr-O bonding, the other one may be assigned to Ca-O bonding. The

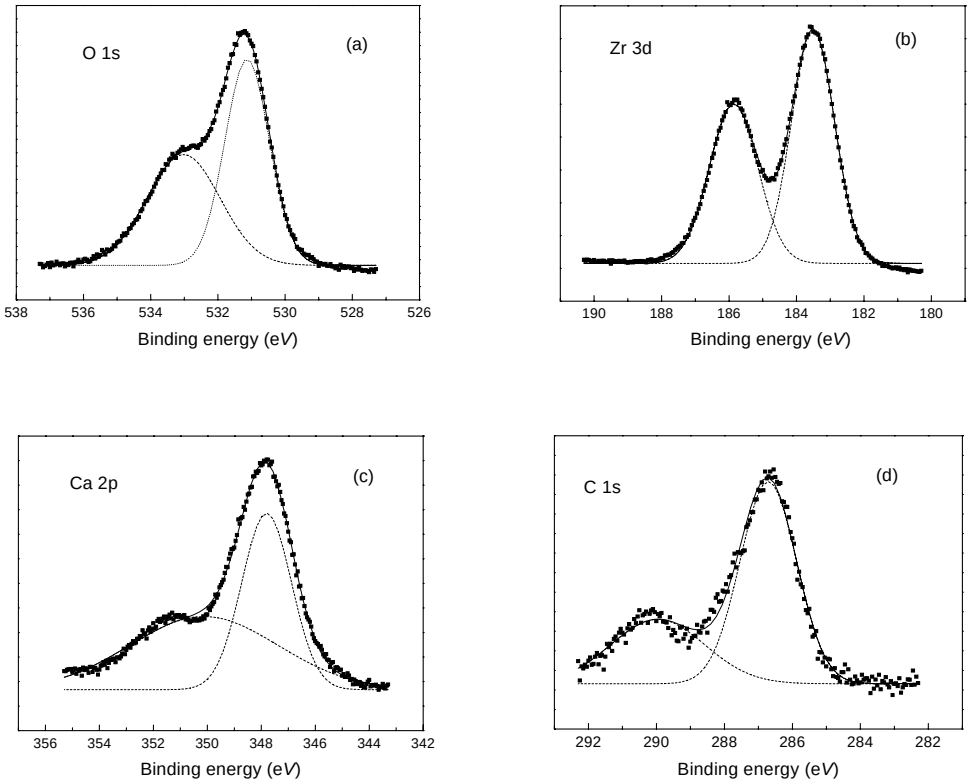

Figure 4-14. XPS spectra of $CaZrO_3$ thin films: experimental points together with the fitted lines.

Table 4-3. Assigning and best fit parameters of $CaZrO_3$ thin films XPS spectra, given in Figure 4-14 (a, b, c, d).

Line	Binding energy (eV)	FWHM (eV)	assigning
$Ca2p_{3/2}$	347.8	1.85	Ca-O bonding
O1s	533.0	2.17	Ca-O bonding
O1s	531.1	1.33	Zr-O bonding
$Zr3d_{5/2}$	183.5	1.28	Zr-O bonding
C1s	286.7	1.67	Surface contamination

$Zr3d_{5/2}$ line is measured at 183.5 e*V* in the sample, therefore in the $CaZrO_3$ perovskite phase. This value is in agreement with the typical bonding of Zr3d oxide [128], which proves that our use of O1s line as referencing method is valid.

Two C1s line are detected in the spectra, this result is similar with that found by Werrett who reported two C peaks on several oxides elaborated by sol-gel derived ZrO_2, Al_2O_3, SiO_2 and TiO_2 [128, 129]. The reason of this discrepancy is not known at present.

4.3 FTIR of sol-gel derived $Ca_xSr_{1-x}ZrO_3$ thin films

Changes in the oxide growth during the annealing process were investigated by the Fourier transform infrared (FTIR) spectroscopy. FTIR enables easy detection and differentiation of molecular forms of functional groups, especially various forms of hydrogen, which cannot be analyzed easily by other surface analytic tools. A bare silicon substrate was used as the reference. Figure 4-15 shows the infrared reflectance spectra of the $CaZrO_3$ (x=1) thin films annealed at different temperatures in the wavelength range of 3000 ~ 400 cm^{-1}. Three main bands are clearly shown in the spectra as follows:

(1) Between 2500 and 2200 cm^{-1}, the 2340, 2363 reflectance peaks were assigned to CO_2.

(2) Between 1800 and 1300 cm^{-1}, the bands typically involve C=O stretching, C-H bending, O-H bending, C=C stretching, and C-O stretching vibrations [131, 132], which confirm the presence of unreacted organic compounds in the films. The bands which are attributed to carbonates, becomes well visible in samples annealed at low temperatures. The presence of carbonates can be due to the combined result of acetate decomposition. The intensities of these bands decreased with the increase of annealing temperatures, indicating that the dissociation and evaporation of these metal-organic compounds occurred. Although the carbonates are not detected by XRD, however, the infrared spectra clearly shows that the residual organic species exist in the samples annealed at low temperatures. The persistence of carbonates up to 600 ºC could represent an obstacle for $CaZrO_3$ crystallization at lower temperatures. Further heat treatment is necessary to remove the organic species of residual carbonates in the films and to promote the crystallization for those films.

(3) Between 800 and 400 cm^{-1}, the Zr-O stretching vibrations are observed.

Figure 4-16 shows the detailed infrared reflectance spectra of the $CaZrO_3$ (x=1) thin films annealed at different temperatures in the wavelength range of 1000 ~ 400 cm^{-1}. Several minor peaks in the low wavelength rage of 500 ~ 400 cm^{-1} could not be confirmed, due to the lack of literature data on the IR reflection. The reflectance peak at 866 cm^{-1} observed in curve (a) and (b) is associated with carbonated vibration bond

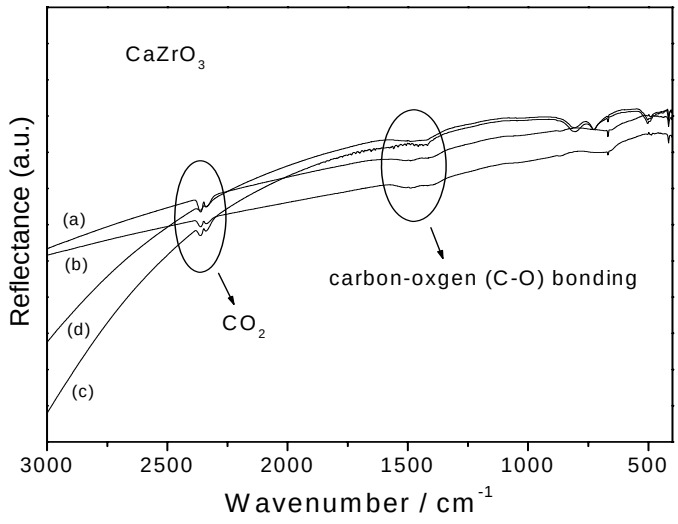

Figure 4-15. FTIR reflectivity spectra at 3000 ~ 400 cm^{-1} for $Ca_xSr_{1-x}ZrO_3$ (x=1) films annealed at: (a) 550 °C, (b) 600 °C, (c) 650 °C, (d) 700 °C.

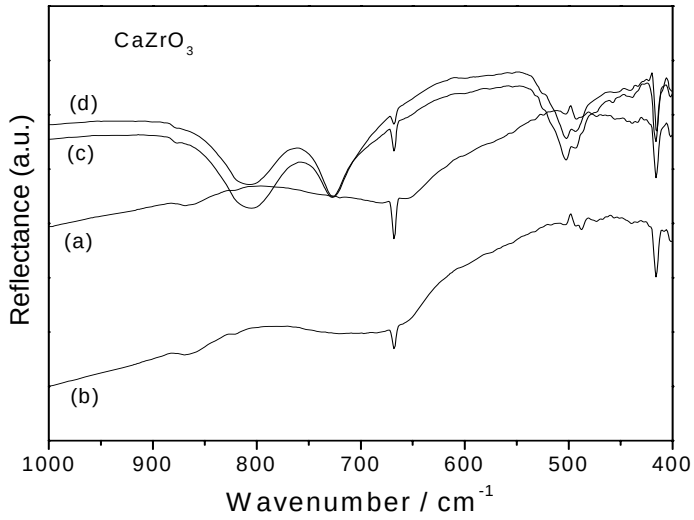

Figure 4-16. FTIR reflectivity spectra at 1000 ~ 400 cm^{-1} for $Ca_xSr_{1-x}ZrO_3$ (x=1) films annealed at: (a) 550 °C, (b) 600 °C, (c) 650 °C, (d) 700 °C.

[133]. It is obvious that there are three main reflectance peaks in the wavelength rages of 850 ~ 500 cm^{-1}. The reflectance peak around 805 cm^{-1} may be attributed to the longitudinal optical phonons of TiO_2, as evidenced by the emerged (002) TiO_2 diffraction peak in Figure 4-5. The reflectance peaks at 502 cm^{-1} and 728 cm^{-1} may be assigned to ZrO_6 octahedral stretching vibration [134] because these two peaks only exist in the samples annealing at higher temperatures (650 ºC and 700 ºC). This result agrees with the XRD results discussed in the previous section. All of the FTIR data suggest complete decomposition of carbonate and the growth of the perovskite phase when the films have been annealed above 600 ºC.

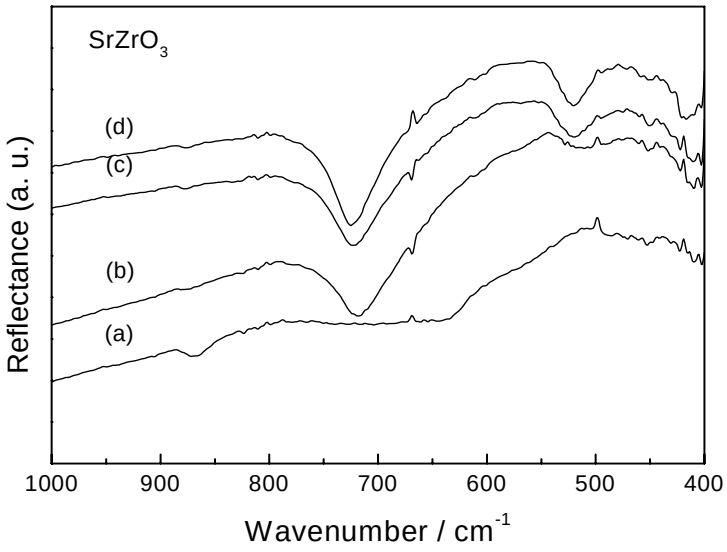

Figure 4-17. FTIR reflectivity spectra at 1000 ~ 400 cm^{-1} for $Ca_xSr_{1-x}ZrO_3$ (x=0) films annealed at: (a) 550 °C, (b) 600 °C, (c) 650 °C, (d) 700 °C.

Figure 4-17 shows the infrared reflectance spectra of the $SrZrO_3$ (x=0) thin films annealed at different temperatures in the wavelength range of 1000 ~ 400 cm^{-1}. It displays similar FTIR behaviors with $CaZrO_3$ thin films. When the thin film is annealed at low temperature of 550 ºC, the reflectance peak between 900 and 800 cm^{-1} is assigned to the vibration band of carbonates [133], which is formed during thermal decomposition of acetate groups. It diminishes when the annealing temperature increases to 600 ºC, showing the completely decomposition of residual organics. With increasing temperature, carbonates associated with amorphous structure are decomposed and eliminated. This result indicates that high temperature heat treatment can eliminate the residual organic content in the sample. The ZrO_6 vibration bands at 520 and 726 cm^{-1}, which change their shape considerably with increasing annealing temperatures, allows to monitor the crystallization of $SrZrO_3$. The broad peak at lower temperature, which indicates a poorly defined network, gradually sharpens. With increasing annealing temperatures, the amorphous film annealed at 550 ºC and transformed to crystals at 600 ºC, which indicates the crystllinity in the $SrZrO_3$ films is improved. The sharpness and narrowness of the FTIR band correlates with a higher degree of crystallinity in the thin films as the annealing temperature increases from 600 to 700 ºC, which is confirmed by XRD analysis. FTIR results clearly show the temperature effect on the elimination of carbonates in the films, evident by the decrease of carbonates vibration peak between 900 and 800 cm^{-1}, and on the improvement of the ZrO_6 FTIR intensity associated with the quality of crystallinity in

the films, showing that FTIR is a powerful tool to monitor the process of crystal growth in the sol-gel processed thin films. Pillai *et al.* [135] reported the crystallization of sol-gel processed $Pb_{0.5}Ba_{0.5}TiO_3$. Small concentrations of barium carbonate phase were evident by FTIR at low temperature. Hwang *et al.* [136] discussed the effects of the variations in heat-treatment temperatures on the crystallinity of hydroxyapatite (HAP) films prepared on alumina substrates using a sol-gel process, which show similar phenomenon with ours.

In conclusion, sol-gel preparation of high-quality thin films requires a good understanding of the effects of the hydrolysis, decomposition and condensation reaction behaviors on microstructure development. Fourier transform infrared spectroscopy (FTIR) is frequently used to elucidate the changes in the chemical structure and oxide growth during thermal processing. From the IR results, it is obvious that there is still a carbonate phase present at 600 ºC. This carbonate phase was not detected by XRD, because it is either amorphous or the fraction of carbonate is too small to be detected by XRD. FTIR spectra show the perovskite oxide phase growth at higher temperatures (650 ºC and 700 ºC). Further heat treatment is necessary to remove the organic species of residual carbonates in the films and to promote the crystallization for those films. FTIR studies provide detailed insight in the thermal decomposition and perovskite oxide phase development of sol-gel derived $Ca_xSr_{1-x}ZrO_3$ thin films.

4.4 Dielectric properties of sol-gel derived $Ca_xSr_{1-x}ZrO_3$ thin films

The dielectric properties of sol-gel derived $Ca_xSr_{1-x}ZrO_3$ thin films were investigated in terms of capacitance and dielectric loss. In this section the study on the dielectric properties will clarify the correlation of the dielectric properties with the processing and their microstructure features. As it is well known, the microstructure and the non-stoichiometric defects of the films affect their dielectric properties such as dielectric constant, dielectric loss, etc. The knowledge of these microstructure dependent dielectric properties will provide an insight to optimize the processing of thin films for high-k applications.

The dielectric characteristics of $SrZrO_3$ and $CaZrO_3$ thin films annealed at different temperatures of 550, 600, 650 °C and 700 °C in O_2 atmosphere for 1h as a function of frequency measured at room temperature are shown in Figure 4-18. During the measurement the applied bias voltage was zero and the oscillation level was 50 m*V*. It can be easily seen from the Figure 4-18 that the dielectric constant of these films is nearly independent of frequency. The dielectric loss is very low for the samples annealed in O_2. However, Figure 4-18 shows that there is a tendency for the dielectric loss to increase at frequency above 100 kHz. Several possible sources exist for such dispersion, including the influence of inductance from metal contacts that increases with the increase in frequency, the presence of the barrier layer between the insulating film and the electrode surface, or leaky grain boundaries. This phenomenon has also

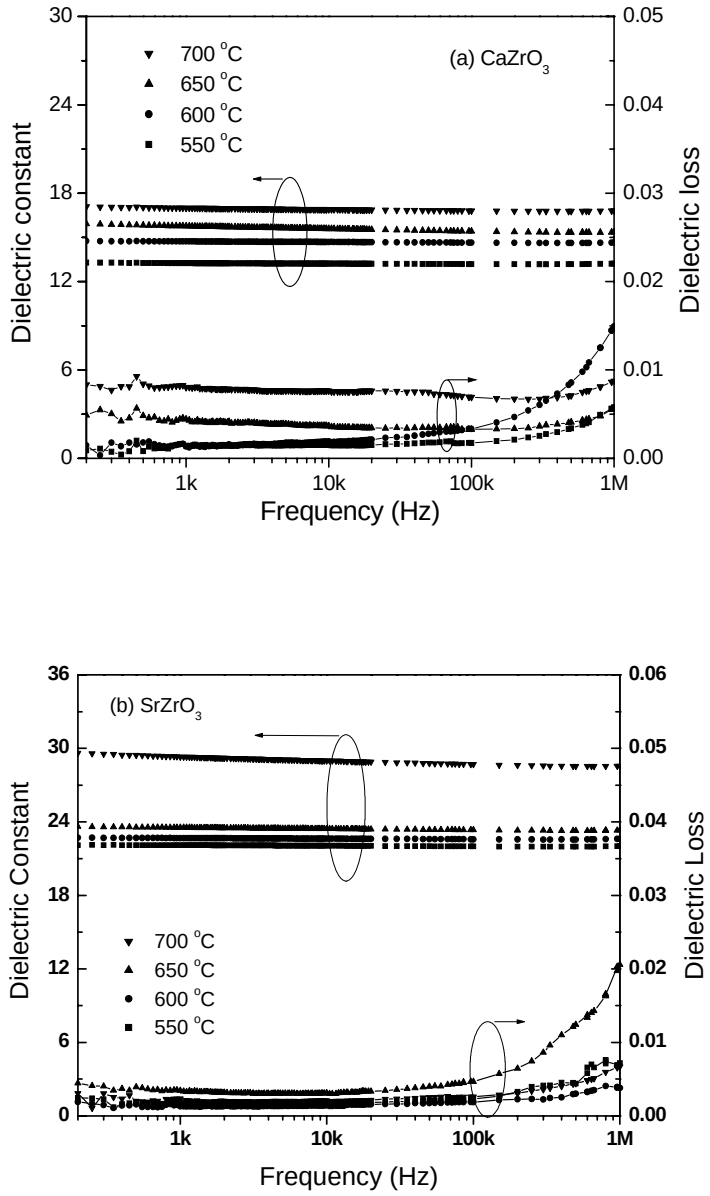

Figure 4-18. Dielectric constant and dielectric loss dependence on frequency of $CaZrO_3$ thin films (a) and $SrZrO_3$ thin films (b) annealed at different temperatures in O_2.

been reported for dielectric BST thin films [137] and it is not regarded to relate to the intrinsic properties of the BST films. Since the tendency has also been observed in the amorphous films, the influence of inductance from metal contacts is preferred to explain this phenomenon in our experiments.

The dielectric constant dependence on the applied bias is shown in Figure 4-19. During the measurement the oscillation level was 50 m*V* and the frequency was 100 kHz. The nearly flat curves without any significant change in dielectric constant indicate that the dielectric constant of these samples does not depend on the applied bias. Typically at a frequency of 100 kHz, the dielectric constants of $CaZrO_3$ thin films annealed at 550, 600, 650 °C and 700 °C are 12.8, 14.4, 15.7 and 16.0, respectively, and the corresponding values of dielectric loss are 0.0018, 0.0027, 0.0026 and 0.0027, respectively. The dielectric constants for $SrZrO_3$ films annealed at 550, 600, 650 °C and 700 °C are 22.0, 22.6, 23.3 and 28.7, respectively, and the corresponding values of dielectric loss are 0.0023, 0.0018, 0.0047 and 0.0026, respectively.

Samples with other doping compositions show similar dielectric properties to those of the two end components, as shown in Figure 4-20. The flat curves without any significant change in dielectric constant indicate that the dielectric constant of these samples does not depend on the applied bias. In most cases, capacitor devices require

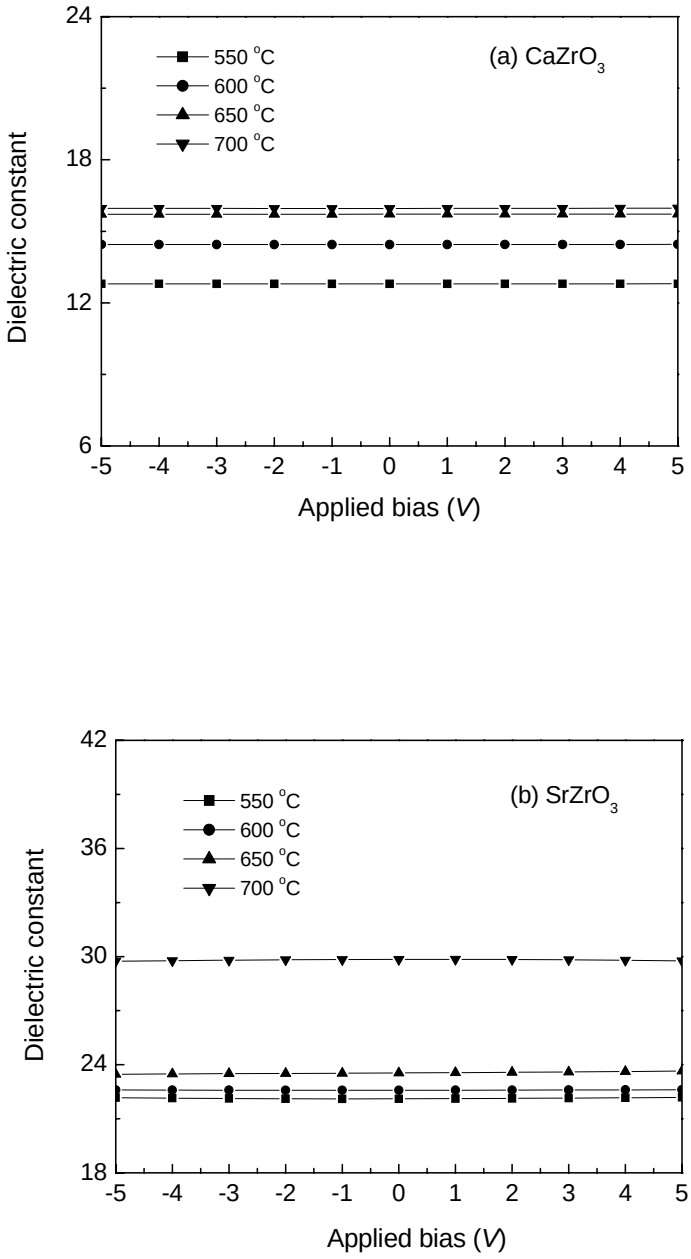

Figure 4-19. Dielectric constant dependence on applied bias of $CaZrO_3$ thin films (a) and $SrZrO_3$ thin films (b) annealed at different temperatures in O_2

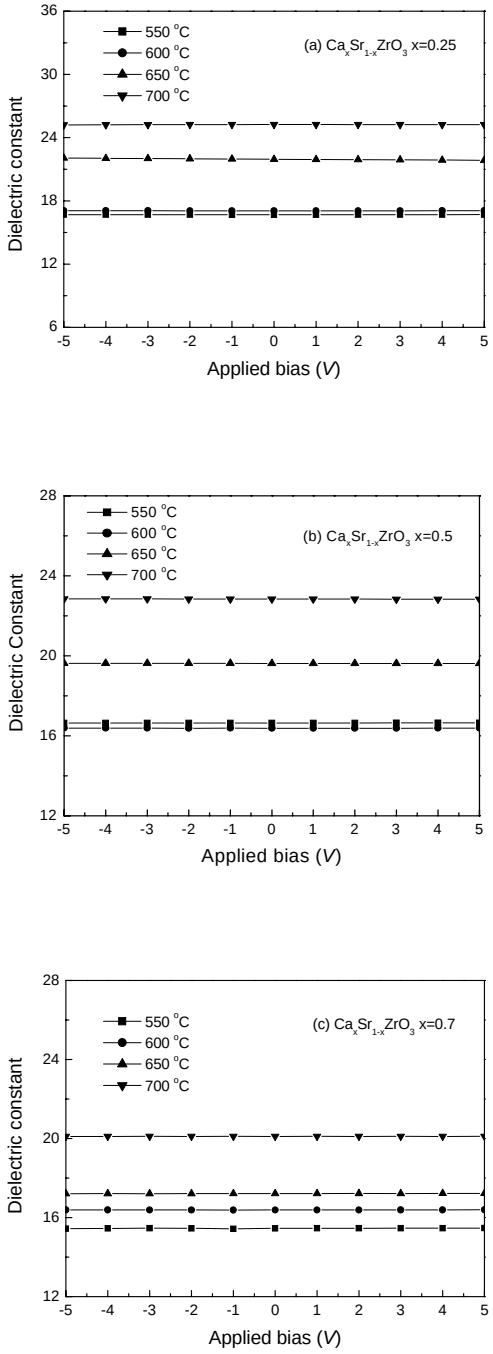

Figure 4-20. Dielectric constant dependence on applied bias of $Ca_xSr_{1-x}ZrO_3$ thin films annealed at different temperatures in O_2 for (a) x=0.25, (b) x=0.5, (c) x=0.7.

that there is no practical change in the value of capacitance with the change in electric field. Thus, $Ca_xSr_{1-x}ZrO_3$ films are suitable for capacitor in practical high-k device use.

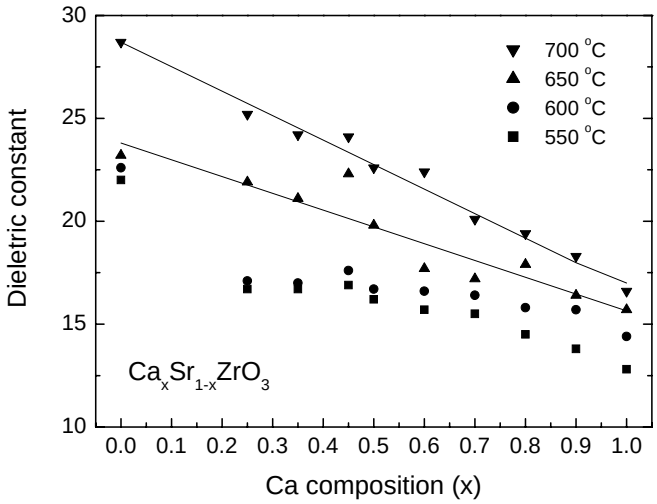

Figure 4-21. Dielectric constant dependence on composition x of $Ca_xSr_{1-x}ZrO_3$ thin films annealed at different temperatures in O_2.

To clarify the influence of the microstructure and compositions of $Ca_xSr_{1-x}ZrO_3$ thin films, Figure 4-21 shows the dielectric constant of $Ca_xSr_{1-x}ZrO_3$ thin films annealed at different temperatures as a function of the composition. First, it can be seen that the dielectric constant increases with the increase of annealing temperature. The dielectric constant of the films annealed at low temperature is the lowest due to their amorphous nature, and with the crystallization progressing further, the dielectric constant increases. Accordingly, the increase of dielectric constant is believed to be caused by

the growth of the perovskite grains. The higher value corresponds to a larger grain size, whereas the lower one corresponds to a smaller grain size. Secondly, it also shows that the dielectric constant decreases with the composition x increases. The polarizability arises from the displacement of Zr ions from their regular ZrO_6 octahedron lattice sites under the influence of an applied field, the dipole moment per molecule can be depicted as $ze\delta$ [138], where ze is the ionic charge and δ is the displacement from equilibrium positions. Previous XRD results show that $SrZrO_3$ and $CaZrO_3$ have the same orthorhombic structure, and the unit cell of $SrZrO_3$ is bigger than that of $CaZrO_3$, so the displacement δ for Zr ions in the ZrO_6 octahedron of $SrZrO_3$ is larger than that of in $CaZrO_3$. That is the possible reason why $SrZrO_3$ has a higher dielectric constant. The increase of dielectric constant is caused by substitution of Sr to Ca, which $SrZrO_3$ has a higher dielectric constant. In addition, the dielectric constant of high temperature annealed films (650 °C and 700 °C) decreases quasi-linearly as the Ca content x increases, which can be expressed as follow equation:

$$\varepsilon_{Ca_xSr_{1-x}ZrO_3} = x \times \varepsilon_{CaZrO_3} + (1-x) \times \varepsilon_{SrZrO_3} . \qquad (4\text{-}3)$$

This similar phenomenon has also been observed in the ternary system $0.5PNN-(0.5-x)PZN-xPZT$ [139]. More investigations are needed to confirm these suggestions. And this feature would facilitate the adjustment of the dielectric constant in practice.

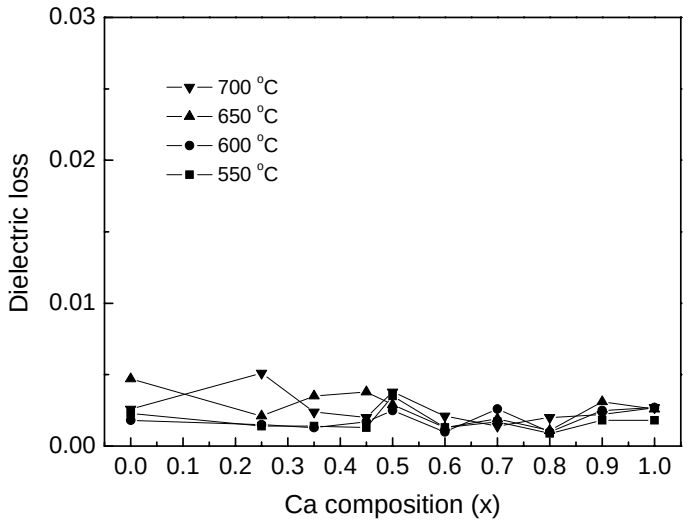

Figure 4-22. Dielectric loss dependence on composition x of $Ca_xSr_{1-x}ZrO_3$ thin films annealed at different temperatures.

Figure 4-22 shows the dielectric loss dependence on composition x of $Ca_xSr_{1-x}ZrO_3$ thin films annealed at different temperatures. Their very low values of dielectric loss are favorable for $Ca_xSr_{1-x}ZrO_3$ films in capacitor device applications.

4.5 Sol-gel derived ZrO_2 thin films

4.5.1 Properties of sol-gel derived ZrO_2 thin films

Among the high-k binary oxides that are predicted to be thermodynamically stable in contact with silicon, ZrO_2 holds promise as a gate dielectric [43]. It has a dielectric constant of about 25 with a wide band gap ~5.1–7.8 e*V* and good thermal stability [140, 141]. Since ZrO_2 has received marked attention as a potential high-k candidate

currently, it is necessary to compare with the properties of $Ca_xSr_{1-x}ZrO_3$ thin films. ZrO_2 thin films were prepared by the same sol-gel process.

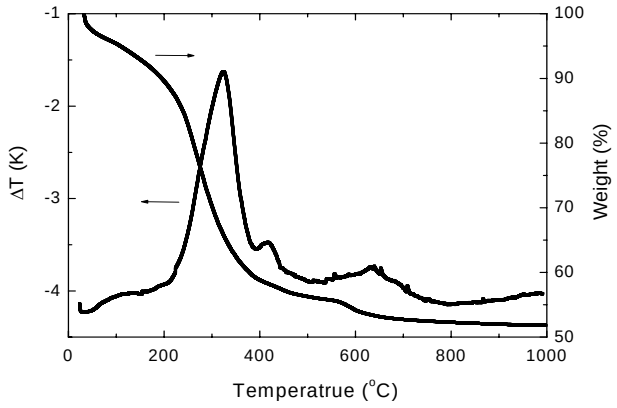

Figure 4-23. DTA and TGA curves of the ZrO_2 dried precursor at a heating rate of 2 ºC/min in air.

Zirconium acetylacetonate was chosen as the precursor. It was dissolved in glacial acetic acid and stirred at room temperature to get a clear and transparent solution. Figure 4-23 shows the DTA and TGA results of the ZrO_2 dried precursor. The exothermic peak at 310 ºC is ascribed to the oxidation of the organics. This oxidation causes a continuous decrease in sample weight in this temperature region. The exothermic peak at 410 ºC is attributed to the crystallization temperature of ZrO_2. It is much lower than that of the $Ca_xSr_{1-x}ZrO_3$ system.

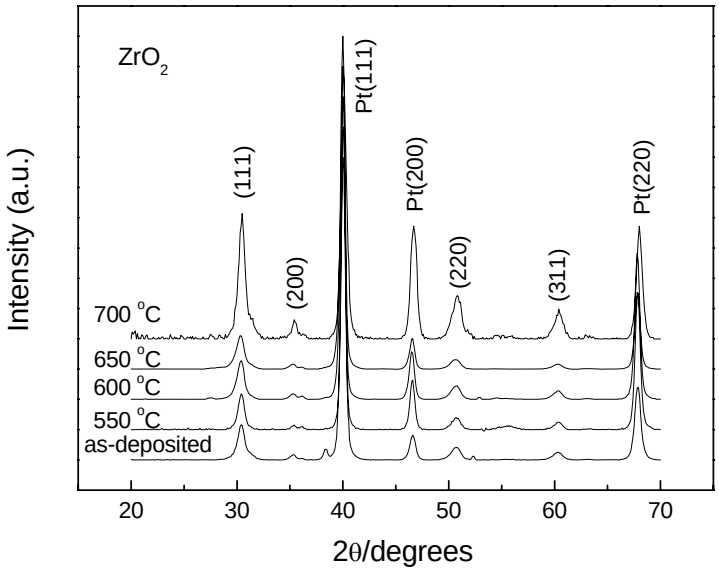

Figure 4-24. XRD patterns of ZrO_2 thin films annealed at different temperatures.

The deposited films spun onto the cleaned $Pt/Ti/SiO_2/Si$ substrate at 4000 rpm for 35s were dried at 400 ºC for 5 minutes. After this procedure was performed several times, the films were finally annealed in a micro-processor-controlled tube furnace in flowing oxygen atmosphere at different temperatures of 550 ºC ~ 700 ºC with an interval of 50 ºC for 1h. The thickness of these thin films measured by a Dektak III profiler is approximately 100 nm. Figure 4-24 shows the XRD patterns for these films prepared on $Pt/Ti/SiO_2/Si$ substrate. It can be seen from the figure that the as–deposited film is also crystallized. It seems that the crystallization temperature of the sol-gel derived ZrO_2 thin films is very low. There is no tendency of preferential

orientation in the sol-gel derived ZrO_2 thin films. The peaks are indexed to be the monoclinic structure (JPCDS 27-0997).

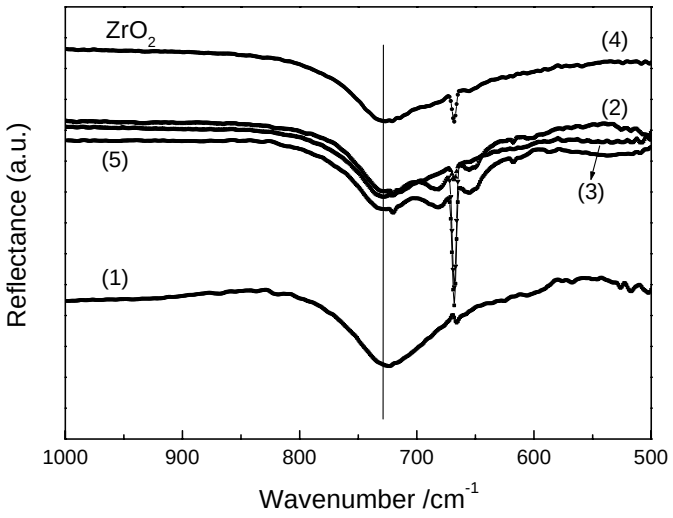

Figure 4-25. FTIR reflectivity spectra at 1000 ~ 500 cm^{-1} for ZrO_2 thin films (1) as-deposited and annealed at: (2) 550 ºC, (3) 600 ºC, (4) 650 ºC, (5) 700 ºC.

Figure 4-25 shows the FT-IR reflectivity spectra of those as-deposited and annealed films at different temperatures in the wavelength range of 1000 ~ 500 cm^{-1}. A bare silicon substrate was used as the reference. The reflectance peak at 728 cm^{-1} can be assigned as ZrO_6 octahedral stretching vibration [134], which is very close to the FT-IR reflectance peak of $CaZrO_3$ thin films.

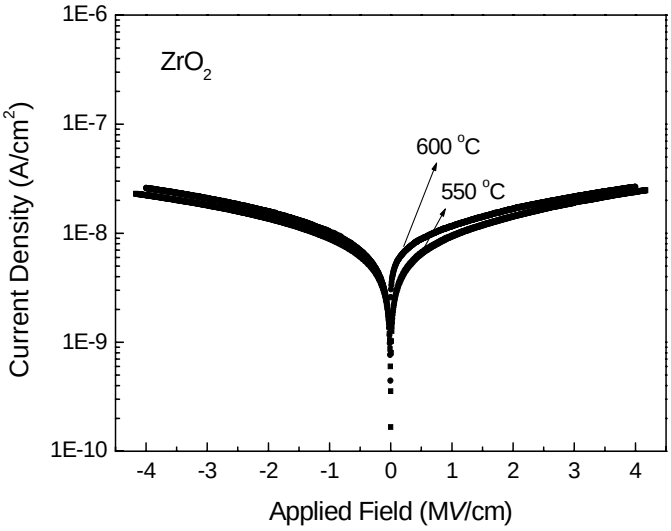

Figure 4-26. Leakage current density dependence on applied field of ZrO_2 thin films annealed at 550 ºC and 600 ºC.

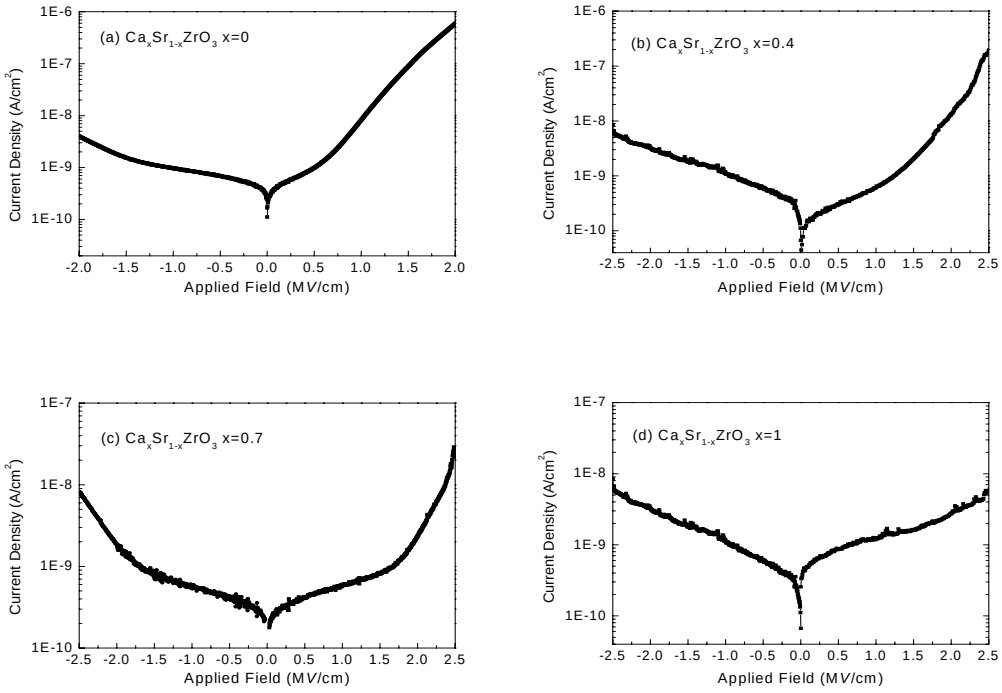

Figure 4-27. Leakage current density dependence on applied field of $Ca_xSr_{1-x}ZrO_3$ films annealed at 600 ºC (a) x=0, (b) x=0.4, (c) x=0.7, (d) x=1.

The characteristics of leakage current density versus applied field for capacitors of Au/Ti/ZrO_2/Pt are shown in Figure 4-26. The leakage current density of the ZrO_2 thin film annealed at 550 ºC for 1 hour is approximately 2.23×10^{-8} A/cm^2 at high applied electric field of 4M*V*/cm. Electrical measurements results show that the leakage current density subjected to an external electric field displayed a linear relationship in the $\log_{10}(J)$ vs $E^{1/2}$ plots. This dependence is attributed to the field enhanced Schottky (ES) mechanism. The ES processes across the interface between a metal and an insulating film as a result of barrier lowering due to the applied field and the image force. The current governed by the ES mechanism is described as equation (5-2). (See chapter 5)

For the comparison of leakage current density, Figure 4-27 shows the leakage current density dependence on applied field of $Ca_xSr_{1-x}ZrO_3$ films annealed at 600 ºC (a) x=0, (b) x=0.4, (c) x=0.7, (d) x=1.

The dielectric characteristics of ZrO_2 as a function of frequency measured at room temperature are shown in Figure 4-28. The measurement is carried out by applying a 50 m*V* ac voltage with a HP 4284 LCR meter. It can be seen that the dielectric constant and dielectric loss show dispersion with increasing frequency. As interpreted by several research groups [142, 143], the frequency dispersion in the range of 100 Hz to 100 kHz is related to the dielectric relaxation in the films, which might originate in

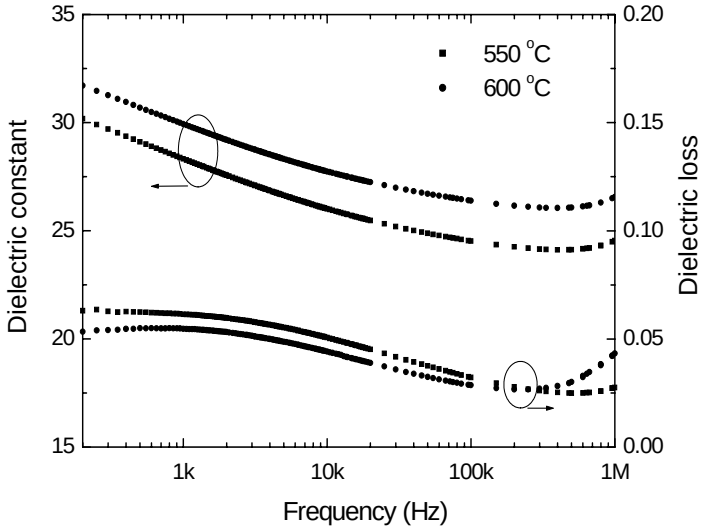

Figure 4-28. Dielectric constant and dielectric loss as a function of frequency of ZrO_2 thin films.

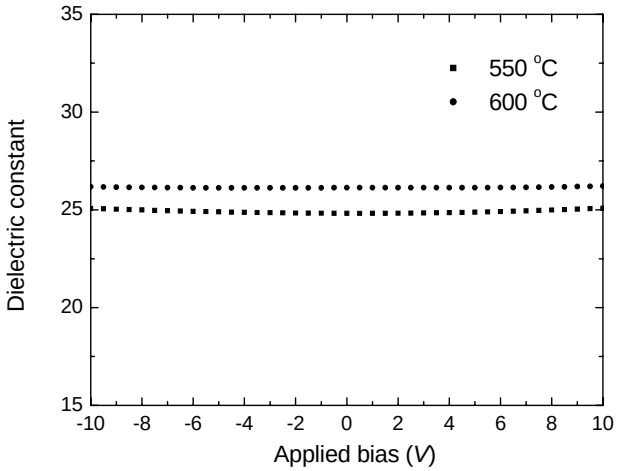

Figure 4-29. Dielectric constant dependence on applied bias of ZrO_2 thin films at a frequency of 100k Hz.

the oxygen vacancy species in the interfacial depletion layer. In most cases, the capacitor device requires that there is no practical change in the value of capacitance with the change in frequency.

The dielectric constant dependence on the applied bias is shown in Figure 4-29. During the measurement the oscillation level was 50 m*V* and the frequency was 100k Hz. The flat curve with no significant change in the dielectric constant indicates that ZrO_2 film has its dielectric constant nearly independent of the applied dc bias. The dielectric constant is about 25, which is consistent with the previous reports [140, 141].

4.5.2 Comparison of ZrO_2 and $Ca_xSr_{1-x}ZrO_3$ thin films

We give the comparison of ZrO_2 and $Ca_xSr_{1-x}ZrO_3$ thin films prepared by the same sol-gel process, which is shown in Table 4-4.

Compared with ZrO_2 oxide thin films, the high temperature thermodynamic stability, high and stable dielectric constant, and low leakage current density suggest that the $Ca_xSr_{1-x}ZrO_3$ thin films are more suitable as a promising candidate for high-k microelectronic device applications.

Table 4-4. Comparison of properties of ZrO_2 and $Ca_xSr_{1-x}ZrO_3$ thin films.

	Crystallization temperature (ºC)	Dielectric constant	Leakage current density @1M*V*/cm annealed at 600 ºC (A/cm^2)
ZrO_2	~400, very low	~25, shows dispersion with frequency	1.2×10^{-8}
$Ca_xSr_{1-x}ZrO_3$	Higher than >600	16~28, stable with frequency and applied field	8.2×10^{-9}, x=0 5.7×10^{-10}, x=0.4 6.0×10^{-10}, x=0.7 1.2×10^{-9}, x=1 (extracted from Figure 4-27)

CHAPTER FIVE

EFFECTS OF THE PREPARATION CONDITIONS

In Chapter 4, we have investigated the influence of the processing parameters on the structure and dielectric properties of the $Ca_xSr_{1-x}ZrO_3$ thin films. It is well established that the dielectric and electrical properties of thin films are dependent on the compositional ratio, the film thickness, the electrode materials, and many other processing conditions. In this chapter much effort has been made to achieve low leakage current density levels and to understand leakage conduction mechanisms in perovskite thin films. The crystalline structure, dielectric and electrical properties of the $Ca_xSr_{1-x}ZrO_3$ system were investigated as a function of the preparation conditions of various substrates and the heat-treatment conditions after thin film deposition.

This chapter is composed of three sections. The effects of the bottom electrode and heat-treatment are investigated in the first two sections, respectively. Thereafter, the leakage conduction mechanisms are discussed in the last section.

5.1 Effect of the bottom electrode

5.1.1 Films deposited on various substrates

A Pt/Ti bilayer has been widely used as a bottom electrode for dielectric thin films. Platinum (Pt) is one of the most promising candidates for the bottom electrodes due to its high thermal conductivity and good stability in high-temperature oxidizing environments [144]. However, the adhesion of Pt to substrates such as silicon-oxide (SiO_x) is poor. Ti is introduced to promote adhesion between Pt and the substrates. It was reported that when the Pt/Ti substrates were heat-treated in oxygen environment, titanium oxide formed along Pt grain boundaries [145], and that in the Pt/TiO_2 system the TiO_2 inhibits the diffusion of Ti into the Pt layer [145, 146].

The $Ca_xSr_{1-x}ZrO_3$ (x=0) thin films were deposited on two different kinds of substrates. Figure 5-1 shows the XRD patterns for those films deposited on Pt/Ti/SiO_2/Si substrates and Pt/TiO_2/SiO_2/Si substrates at different annealing temperatures in flowing oxygen. From Figure 5-1 (a) it is clearly shown that with the increase of annealing temperature to higher than 600 °C, the diffraction peaks of TiO_2 appear,

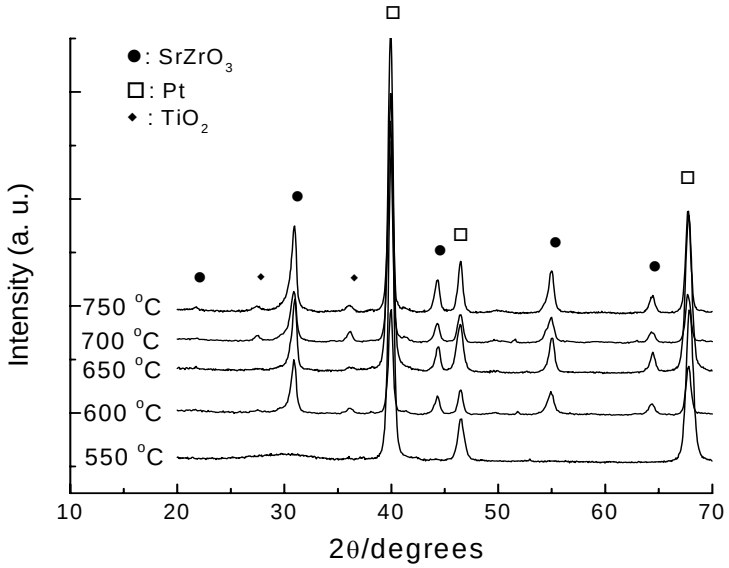

(a)

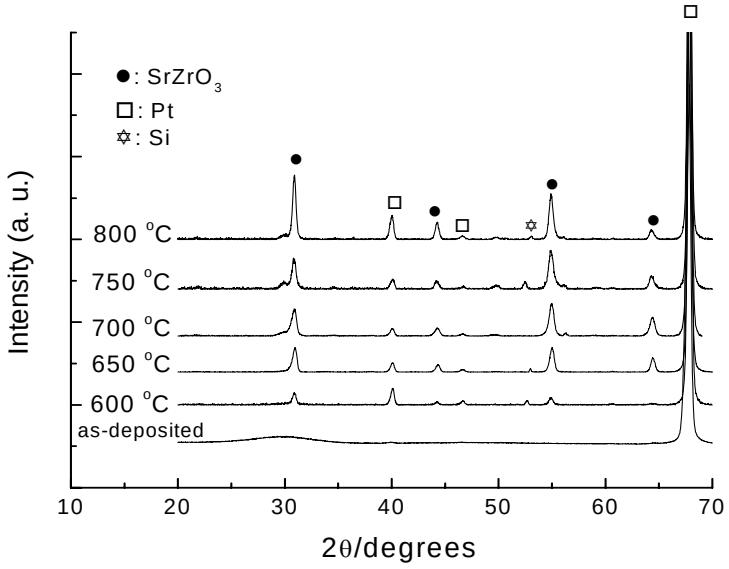

(b)

Figure 5-1. X-ray diffraction patterns of $Ca_xSr_{1-x}ZrO_3$ (x=0) films deposited on various substrates. (a) $Pt/Ti/SiO_2/Si$, (b) $Pt/TiO_2SiO_2/Si$.

which are caused by the interdiffusion of the Pt/Ti bottom electrode, it will be discussed in detail in the following section. On the contrary as shown in Figure 5-1 (b), by using $Pt/TiO_2/SiO_2/Si$ substrate, there are no TiO_2 peaks in the films even after annealing at 800 °C, which indicates that the thin TiO_2 binding layer protects the bottom electrode from the diffusion of Ti effectively.

Figure 5-2 shows the leakage current density dependence on applied field of $Ca_xSr_{1-x}ZrO_3$ (x=0) films deposited on these two substrates. As clearly shown in Figure 5-2, the films deposited on the $Pt/Ti/SiO_2/Si$ substrate show poorer leakage current properties compared to the films deposited on $Pt/TiO_2/SiO_2/Si$ substrate when annealed at above 650 °C. The possible reason is due to the interdiffusion of the Pt/Ti bottom electrode. By using a thin TiO_2 as the binding layer, the interdiffusion can be effectively reduced, so that the electrical properties of the thin films are improved.

As seen in both *J-E* curves in Figure 5-2, when annealed at 550 and 600 °C, the thin films achieve very low leakage current density at a level of 10^{-9} A/cm^2 and high breakdown strength. The poorest current property obtained in the films using $Pt/Ti/SiO_2/Si$ substrate annealed at above 650 °C may be due to the open grain boundaries in thin films which are annealed at relatively high temperature [147].

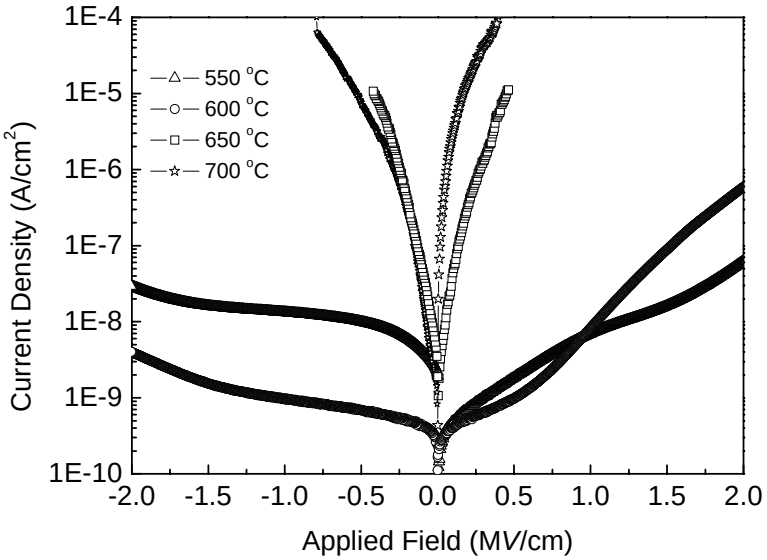

(a)

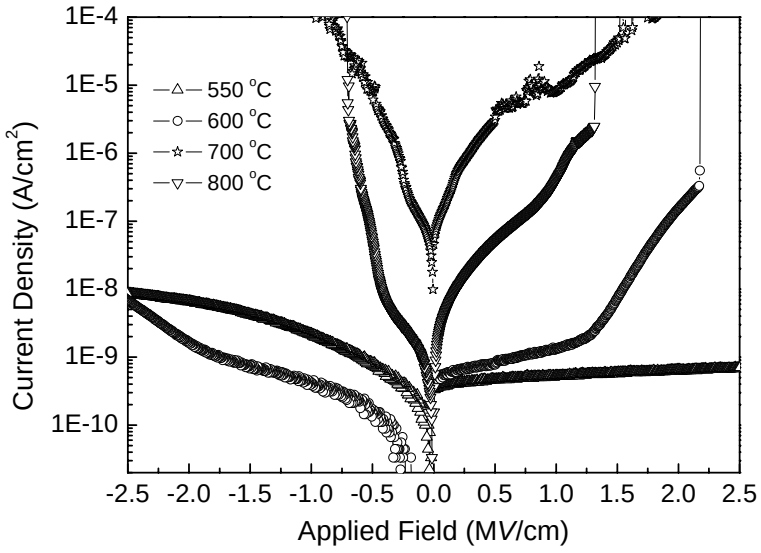

(b)

Figure 5-2. Leakage current density dependence on applied field of $Ca_xSr_{1-x}ZrO_3$ (x=0) films deposited on (a) $Pt/Ti/SiO_2/Si$ and (b) $Pt/TiO_2/SiO_2/Si$ substrates.

Meanwhile, if using $Pt/TiO_2/SiO_2/Si$ as the substrate, the bottom electrode can survive even after annealed at 800 °C as shown in Figure 5-2 (b). The leakage current density of the thin film annealed at 800 °C is about 4×10^{-7} A/cm^2 at a high electric field of 1 M*V*/cm. However, the thin film annealed at 800 °C shows better current property than that of the 700°C annealed film. The possible reason is that such a high temperature treatment can promote thin film crystallized more completely and thus greatly eliminate the electrical defects related to the polycrystalline grain.

5.1.2 AES depth profile

An investigation of Ti out-diffusion toward the Pt surface has been done to clarify the leakage properties of $CaZrO_3$ thin films deposited on $Pt/Ti/SiO_2/Si$ substrate. However, it is not easy to observe the distribution of Ti on Pt surface because the amount of Ti out-diffused to the Pt surface is very small. From Figure 5-1(a), XRD results also confirms that titanium oxide phase exists when the $SrZrO_3$ thin films have been annealed at high temperature above 650 °C which are deposited on $Pt/Ti/SiO_2/Si$ substrate.

The expected reactions are well known in the literature on the oxidation mechanisms in titanium, and on Ti/SiO_2 interface studies. It was found that at annealing temperatures around 650 °C the out-diffused oxygen atoms due to SiO_2 dissociation will dissolve into the region of the bilayer metal films [148]. The strong affinity

between Ti and oxygen seems adequate to cause its diffusion along the Pt-grain boundaries. Kim *et al.* [149] found the formation of a TiO_2 phase when $Pb(Zr,Ti)O_3$/Pt/Ti/SiO_2/Si sample was annealed at temperature of 600 °C or higher in O_2. AES analysis of the 650 °C annealed sample confirmed the presence of a Pt-containing layer sandwiched by TiO_2 layers. In this study, the interdiffusion of Pt, Ti and O inside the Pt/Ti layer was investigated by AES depth profiling and the out-diffusion of Ti was inferred from the results.

The AES depth profiles of the $Ca_xSr_{1-x}ZrO_3$ (x=1) thin films annealed at different temperatures are shown in Figure 5-3.

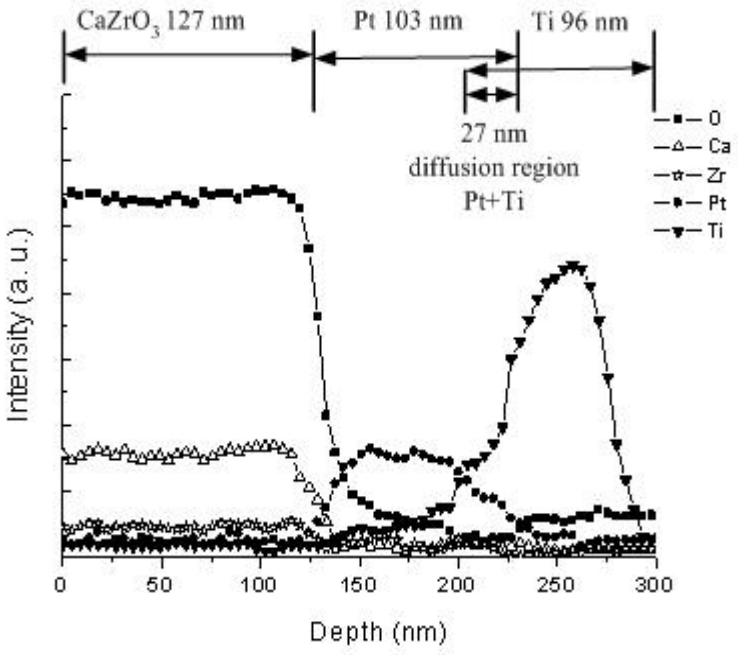

(a)

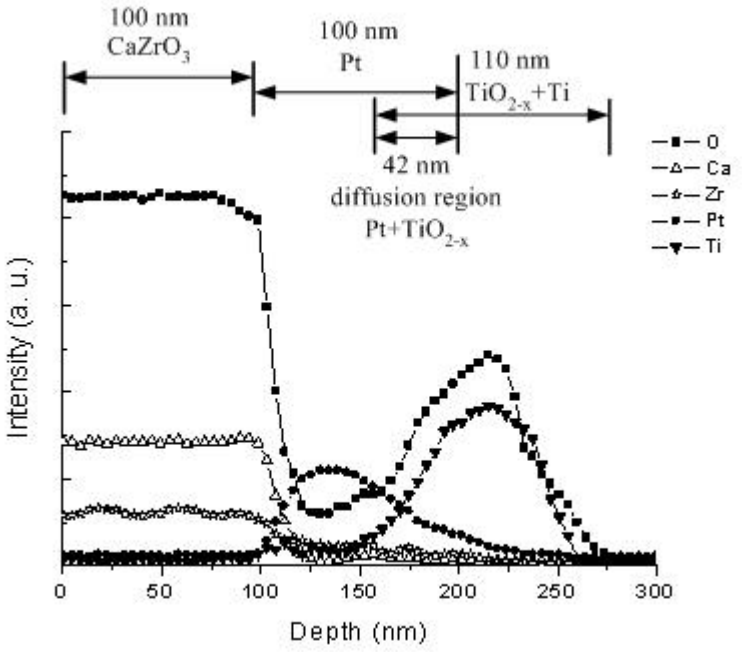

(b)

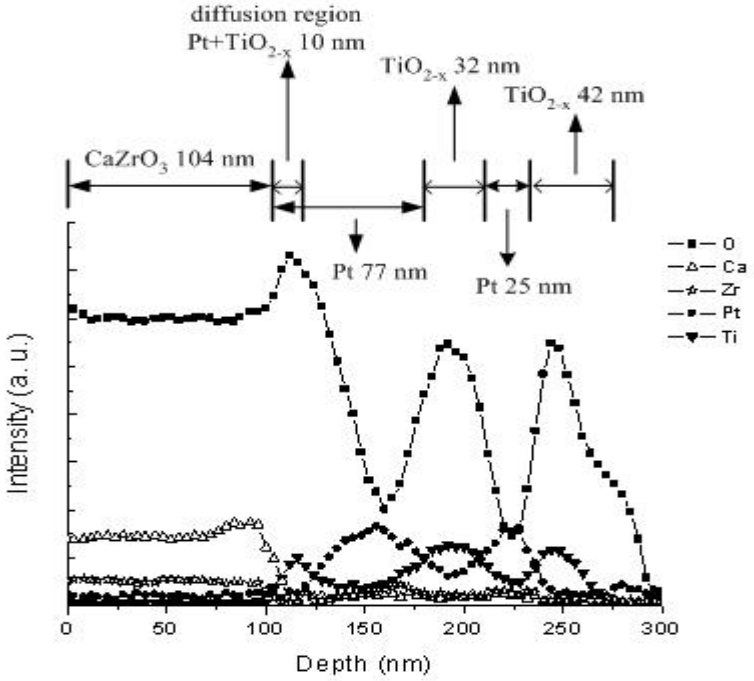

(c)

Figure 5-3. AES depth profiles of the $Ca_xSr_{1-x}ZrO_3$ (x=1) films after annealed at different temperatures (a) 550 °C, (b) 600 °C, (c) 650 °C.

Figure 5-3 (a) shows $Ca_xSr_{1-x}ZrO_3$ (x=1) thin film annealed at 550 °C in flowing oxygen. The concentration of Ti increases abruptly from Pt layer to Ti under layer. Meaning while, the concentration of O decreases abruptly in the Pt layer near Pt surface and increases slightly from Pt layer to Ti under layer. It indicates some inter-diffusion at the Pt/Ti interface, but the remaining flat regions of Pt and Ti maintain their integrity. That means Ti buffer layer is not oxidized into titanium oxide phase when the sample is annealed at low temperature.

When the film is annealed at 600 °C, Figure 5-3 (b) shows that the concentration O and Ti increase abruptly in the Pt layer to Ti under layer. The Pt-Ti inter-diffusion zone expands in comparison to that of the $CaZrO_3$ thin film annealed at 550 °C (as shown in Figure 5-3 (a)). This is probably because Ti under Pt layer near the Pt surface begins to oxidize to form titanium oxide in the Pt grain boundaries. It is reported that increasing the temperature above 500 °C the Pt film was therefore ineffective to prevent the migration of Ti through the Pt film [140].

With increasing annealing temperature to 650 °C, it can be easily seen in Figure 5-3 (c) three titanium oxide layers formed. Ti atoms out-diffuse towards the Pt grain boundaries and the out-diffused metallic Ti can readily diffuse along the surface grain boundaries of Pt because of its good wettability on Pt. Then the surface Ti is oxidized, it forms titanium oxide in the Pt surface grain boundaries.

Based on these data, the diffusion of Ti and O in oxygen environment can be explained as follows. In the initial stage of post-annealing in 550 °C, Ti diffused from the Ti under layer into Pt boundaries and formed about 27 nm diffusion region, as shown in Figure 5-3 (a). As reported in the literature, this process takes place mainly in the highly distorted grain boundary region [150]. Tisone and Drobek [151] found titanium diffusion into platinum boundaries even at 150 °C. As it is well known that Ti is an active element and has its high diffusivity, the oxidation of titanium would be enhanced partly because of the enhanced diffusion of oxygen into the titanium layer at higher temperatures, as shown in Figure 5-3 (b). The diffusion region of combined titanium oxide and Pt increases to 42 nm. With increasing annealing temperature to 650 °C, the peak position of the platinum pile-up move further inward, which is clearly seen in Figure 5-3 (c). All Ti has been consumed in the reaction process. Ti atoms out-diffuse through the Pt grain boundaries and get to the surface, and then it forms titanium oxide (about 10 nm) in the Pt surface grain boundaries. The presence of the titanium oxide phase is confirmed by X-ray diffraction analysis result.

In conclusion, Ti diffusion into the Pt layer along the Pt grain boundaries in the Pt/Ti electrode stacks and the Ti in the Pt layer was oxidized during the post-annealing process in oxygen ambient. Moreover, the $SrZrO_3$ capacitor fabricated on the Pt/TiO_2 electrode stack showed better electrical properties than the capacitor on the Pt/Ti electrode stack.

5.2 Effect of the heat-treatment

In this study, the electrical properties of $Ca_xSr_{1-x}ZrO_3$ (x=1) thin films post-annealed under oxygen and air atmosphere were investigated.

In sol-gel technique and others using organometallic precursors, a problem that has frequently been met is the elimination of residual organics in the film in order to get the film in the desired phase [152]. Depending on the nature of precursor materials, hydrolysis and condensation reactions, residual carbonates can be removed in the amorphous-crystalline phase transformation [153]. The heat treatment temperature needs to be optimized to obtain desirable electrical properties in the thin films. The electrical properties of sol-gel-derived lanthanum-modified lead titanate (PLT) thin films prepared using different precursor sources have been investigated. FTIR and XPS analyses indicate that better removal of carbonaceous contents is the key step to yield improved electrical properties in these films [154]. Zhang *et al.* [155] reported the growth of thin tantalum oxide films which are prepared by spin-coating using a sol-gel processing. Their result showed that the residual organic carbon content, which is considered to be harmful to the electrical properties, can be completely removed by proper heat-treatment.

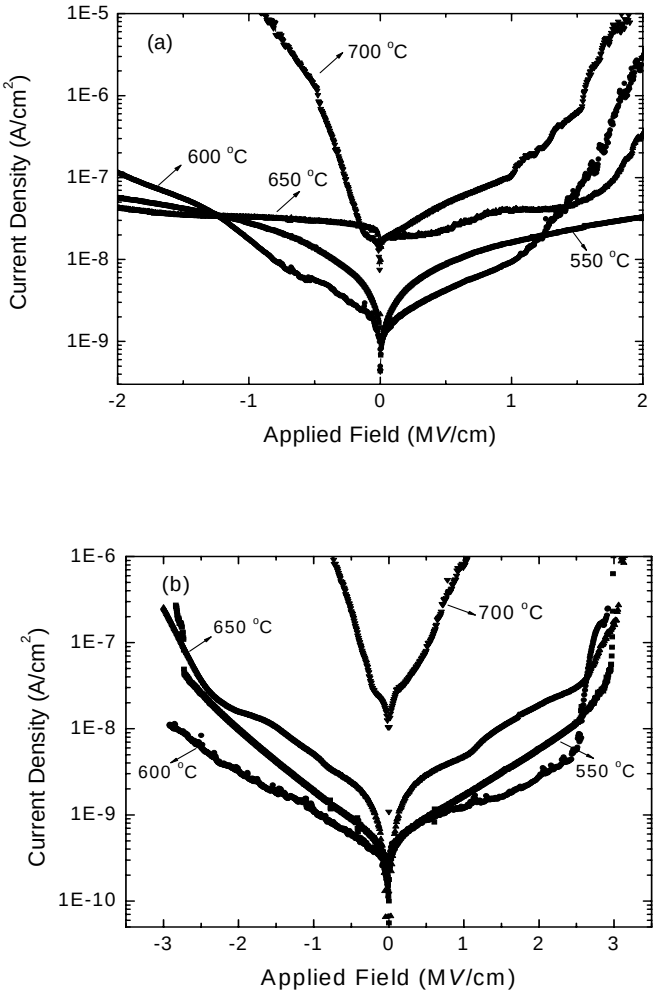

Figure 5-4. Leakage current density dependence on applied field of $CaZrO_3$ films annealed at different temperatures in (a) air and (b) O_2.

The leakage current densities of $CaZrO_3$ thin films post-annealed in air or O_2 atmosphere are plotted as a function of the applied field, as shown in Figures 5-4 (a) and (b). Our FTIR results indicate that residual carbonate content exists in the $CaZrO_3$ thin film annealed at 550 °C. The entrapped residual carbonaceous species is

detrimental to the electrical properties of the films. In general, carbonates are more conductive than high insulating oxides, leading to the deterioration of the insulating properties of the material. Therefore, the thin film annealed at 550 °C has higher leakage current density than that of the thin film annealed at 600 °C. It can be seen from Figure 5-4 that the $CaZrO_3$ thin film annealed at 600 °C shows the best electrical leakage properties due to its amorphous structure and the nearly complete removal of residual carbonates in the film, which is confirmed by XRD and FTIR analyses. Amorphous films usually exhibit low leakage currents compared to the crystalline films because of higher scattering of the charge carries which is due to lack of long range order in the film. XRD results show the thin films have their polycrystalline structure annealed at temperatures to 650 and 700 °C, polycrystalline films show higher leakage current density, which is contributed to grain boundaries serving as leakage paths.

The lowest leakage current densities of the $CaZrO_3$ thin films post-annealed in air or O_2 atmosphere are approximately 1×10^{-8} A/cm^2 and 1×10^{-9} A/cm^2 at 1 MV/cm, respectively. Therefore, a significant reduction in the leakage current is found in the $CaZrO_3$ thin film post-annealed in flowing oxygen. This observation indicates that the leakage current depends on the post-annealing heat-treatment.

It is assumed that the ionized oxygen vacancies are generated on the $CaZrO_3$ outermost surface, which is similar with the BST thin film [156, 157]. Therefore, the highly charged layer on the $CaZrO_3$ thin film surface, similar to highly doped surface layers in semiconductors, can either reduce a potential barrier or result in an ohmic contact. When the external electric field is zero, the width of the depletion region W can be expressed as [158]:

$$W = \left[\frac{2\varepsilon_0\varepsilon_i V_{bi}}{qN_D}\right]^{1/2} \text{ with } qV_{bi} = \phi_M - \chi - (E_C - E_F), \quad (5\text{-}1)$$

where V_{bi} is the built-in potential, χ is the electron affinity of $CaZrO_3$ thin film, and ϕ_M refers to the metal work function. The depletion region width W is inversely proportional to the square root of the charge concentration N_D. This means the width of the depletion region decreases as the charge concentration increases. Thus, with increasing concentration of electrons at the interfacial region, the leakage current through the barrier increases. Therefore, post-annealing in flowing oxygen gas is expected to be useful in reducing the leakage current of $CaZrO_3$ thin film by reducing the concentration of the ionized oxygen vacancies.

5.3 Leakage conduction mechanism

In order to effectively control and decrease the leakage currents, it is necessary to understand the dominant conduction mechanism especially at high electric fields. The rate of increase of current density through an insulator with the applied field can reveal some information about the generation and transportation of charge carriers in

the films. The current density in an insulator can be limited by either of electrode-insulator interface or by the availability of charge carriers in the bulk of the material.

Although $Ca_xSr_{1-x}ZrO_3$ thin films have low leakage characteristics in the amorphous phase, high temperature treatments resulted in the crystallization of the films and the increase of leakage current. Hence, it is important to study the various leakage mechanisms in the amorphous and crystalline films in order to improve their electrical properties. Little studies on the leakage current mechanisms of the amorphous and crystalline $Ca_xSr_{1-x}ZrO_3$ thin films having metal insulator metal (MIM) structure have been investigated in literature. In this section, we report the possible conduction mechanisms in each end member of amorphous and crystalline $CaZrO_3$ and $SrZrO_3$ films at high electric fields.

5.3.1 Conduction mechanisms in $CaZrO_3$ thin films

XRD results showed that the 600 °C annealed $CaZrO_3$ films were amorphous and the 650 °C annealed films crystallized into the perovskite phase. Typical *I-V* characteristics in MIM capacitors with $CaZrO_3$ films annealed at different temperatures in O_2 are shown in Figure 5-4 (b). The increase in leakage current density in the crystallized films may be attributed to some defects resulted from the polycrystalline grain growth and thus opened grain boundaries in thin films annealed

at relatively high temperatures [147]. At very low electric fields, the current density increases approximately linearly with voltage, which means the samples display the Ohmic behavior. At higher fields, the current densities are proportional to the square root of the applied electric field, which suggests that the leakage current density is limited by a different conduction mechanism from that in the low electric field region.

Electrical measurement results show that amorphous $CaZrO_3$ films (annealed at 600 °C in O_2 for 1h) displayed a linear relationship in the ln (J) vs $E^{1/2}$ plots at the electric field region (0.25 ~ 1.8 M*V*/cm). This dependence is attributed to the Schottky thermal conduction mechanism [55]. The current density governed by this mechanism is described as:

$$J = A^* T^2 \exp\left(\frac{\alpha E^{1/2} - q\phi_b}{kT}\right); \quad \alpha = \sqrt{\frac{q^3}{4\pi\varepsilon_r\varepsilon_0}}, \tag{5-2}$$

where J is the current density, A^* the Richardson constant, $q\phi_b$ the Schottky barrier height, T the temperature, E the applied field, k the Boltzman constant, q the electronic charge, ε_r the relative dielectric constant of the ceramic, and ε_0 the permittivity of free space. Thus, by plotting $\ln(J/T^2)$ vs $1000/T$ and $\ln(J)$ vs $E^{1/2}$, a straight line is expected. Agreement with the Schottky thermal conduction mechanism can be checked by comparing the results of the following two methods. In method I, A^* is obtained from the intercept of the $\ln(J/T^2)$ vs $1/T$ plot at a given field. Then, a barrier height is calculated using the Richardson constant and the intercept of the ln(J)

vs $E^{1/2}$ curve at a given temperature. In method II, α is determined from the slope of the ln(J) vs $E^{1/2}$ curve. Using the value of α and the slope of the ln(J/T^2) vs 1/T plot the barrier height can be calculated. Agreement of the barrier heights calculated via the two methods verifies that both the temperature and field dependence of the leakage current density is self-consistently interpreted by the Schottky thermal conduction mechanism.

The temperature dependence of the Schottky conduction behavior via applied fields is shown in Figure 5-5. The field dependence of the Schottky conduction behavior at two temperatures is given in Figure 5-6.

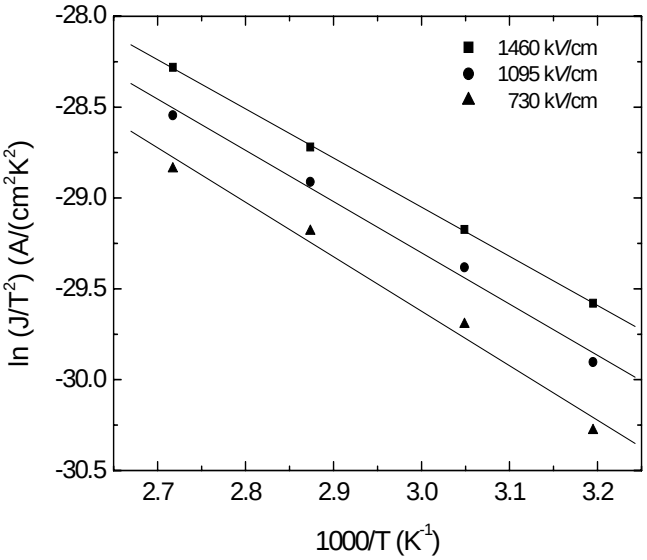

Figure 5-5. Plot of ln (J/T^2) vs 1000/T of amorphous $CaZrO_3$ films, for applied voltages of V=10, 15, and 20 V.

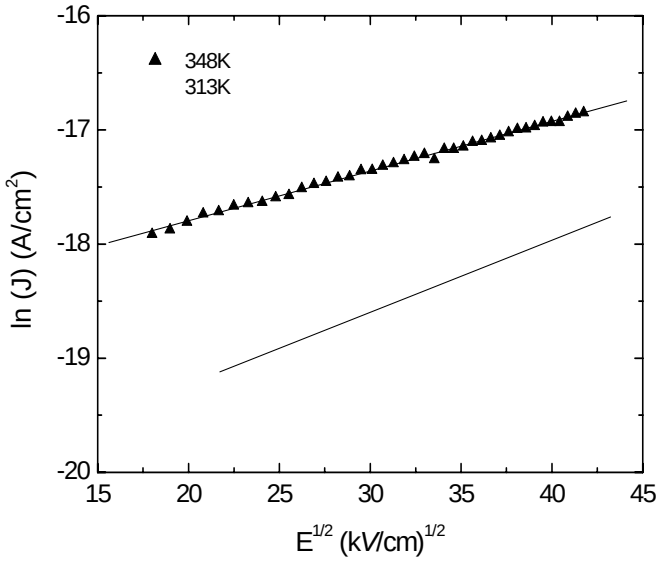

Figure 5-6. Plot of ln(J) vs $E^{1/2}$ of amorphous $CaZrO_3$ films, for measurement temperatures T= 313 and 348 K.

Table 5-1. Barrier heights (in eV) calculated by fitting the data from Figures 5-5 and 5-6.

	730 kV/cm		1095 kV/cm		1460 kV/cm	
	I	II	I	II	I	II
313K	0.34	0.33	0.32	0.29	0.30	0.28
348K	0.34	0.33	0.32	0.31	0.30	0.28

The barrier heights $q\phi_b$ calculated from the two methods are summarized in Table 5-1. It is evident that there is a good agreement with the form predicted from equation (5-2) in both cases. Besides the consistency of the two different analysis methods,

there is also in a good agreement between the barrier heights extracted from the two measurement temperatures.

The agreement in functional form predicted from equation (5-2) for both the temperature and field dependencies strongly supports the conclusion that the Schottky conduction occurs in the amorphous $CaZrO_3$ film.

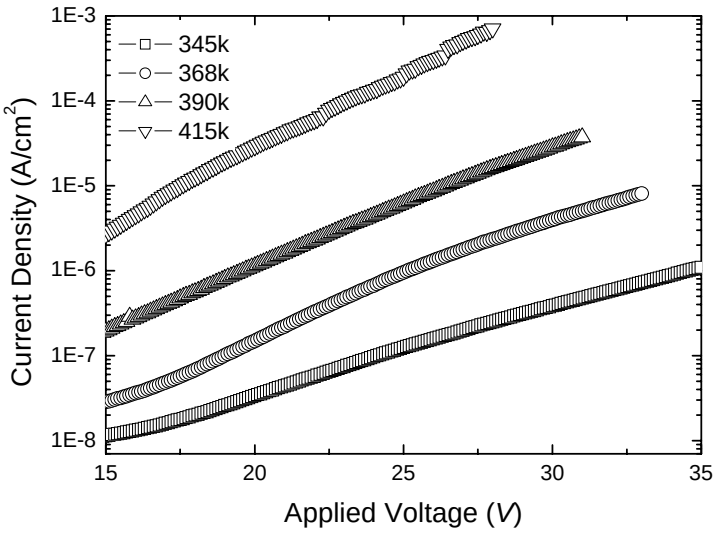

Figure 5-7. Plot of *J-V* of polycrystalline $CaZrO_3$ thin films at different temperatures.

The dominant conduction mechanism of polycrystalline $CaZrO_3$ thin film (annealed at 650 °C in O_2 for 1h) at high electric fields (1.3 ~ 3.0 M*V*/cm) was investigated. The *J-V* characteristics of the $CaZrO_3$ thin films were measured at different temperatures, as shown in Figure 5-7. It can be seen that the leakage current density increases with

increasing the measurement temperature, which indicates at higher temperatures the electrons are increasingly energetic. That is a common phenomenon in insulators.

The current given by the Poole-Frenkel emission can be expressed as [106]:

$$J = BV\exp\left[-\frac{q\phi_{pf} - \gamma E^{1/2}}{kT}\right], \gamma = \left[\frac{q^3}{\pi\varepsilon_0\varepsilon_r}\right]^{1/2}, \tag{5-3}$$

or it can be rewritten as:

$$\ln(J/V) = \ln B + \frac{\gamma\sqrt{E} - q\phi_{pf}}{kT}, \tag{5-4}$$

where B denote constants, $q\phi_{pf}$ is the trap energy level. If the leakage current at high field is governed by the Poole-Frenkel emission, the ln(J/V) vs $E^{1/2}$ plot should be a straight line.

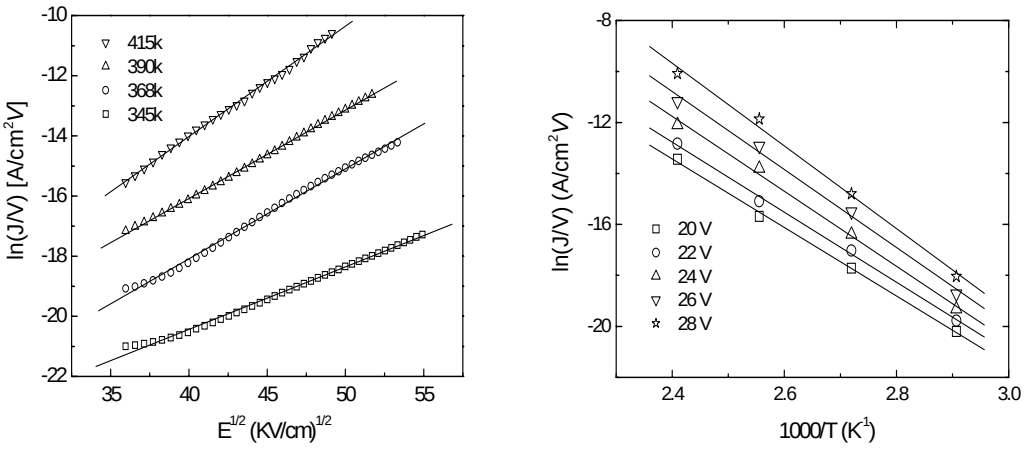

(a) (b)

Figure 5-8. Plot of (a) ln(J/V) vs $E^{1/2}$ and (b) ln (J/V) vs 1000/T of polycrystalline $CaZrO_3$ thin films.

To check the conduction mechanism in the polycrystalline $CaZrO_3$ thin films at high electric fields, ln(*J/V*) was replotted as function of $E^{1/2}$. As a result, Figure 5-8 (a) shows an almost linear relationship in the curve of ln(*J/V*) vs $E^{1/2}$. The Arrhenius plot of ln(*J/V*) against *1/T* taken from the linear extrapolation of plots in Figure 5-8 (a) is shown in Figure 5-8 (b). A quite good linearity can be observed from the plots. The result indicates that the relation of the Poole-Frenkel mechanism is satisfactorily followed. A trap level $q\phi_{pf}$ of 0.62 e*V* can be obtained. Therefore, it is concluded that the conduction mechanism of polycrystalline $CaZrO_3$ thin film at high electric fields is dominated by the Poole-Frenkel effect.

It is interesting to see that the barrier height of the Poole-Frenkel conduction in polycrystalline $CaZrO_3$ thin films is higher than the barrier height of the Schottky thermal conduction in amorphous $CaZrO_3$ thin films obtained previously, although the former has a higher leakage current density than that of the latter at high electric fields. It indicates that the trap density responsible for the high leakage current must be higher in the polycrystalline $CaZrO_3$ thin film.

5.3.2 Conduction mechanisms in $SrZrO_3$ thin films

XRD results showed that the 550 °C annealed $SrZrO_3$ films were amorphous and the 600 °C annealed films crystallized into the perovskite phase. Similar with the discussion in the previous section, the leakage current in $SrZrO_3$ thin films is usually

described by Schottky conduction or Poole-Frenkel conduction mechanism at high electric fields.

Electrical measurement results show that amorphous $SrZrO_3$ films (annealed at 550 °C in O_2 for 1h) displayed a linear relationship in the ln (J) vs $E^{1/2}$ plots at the electric field region (1.0 ~ 2.5 MV/cm), as shown in Figure 5-9.

A quite good linearity can also be observed from the plot of ln (J/T^2) vs 1000/T. These results indicate that the relation of the Schottky thermal conduction is dominant in amorphous $SrZrO_3$ films. A barrier height of $q\phi_b$=0.6 eV can be evaluated from Figure 5-10.

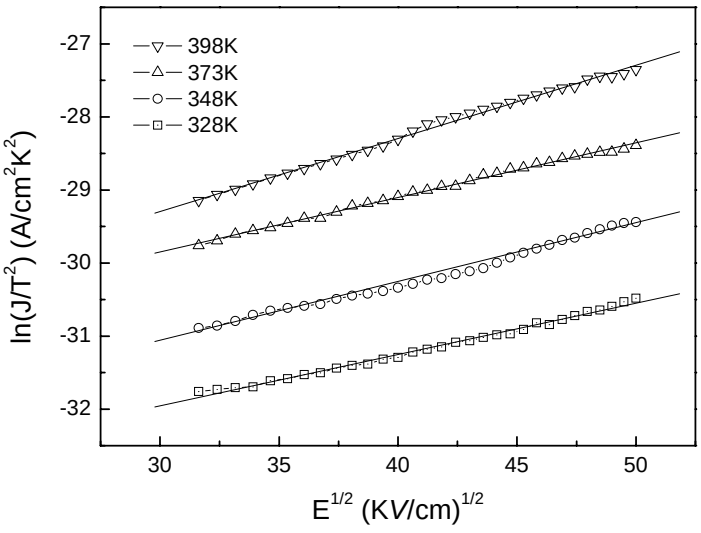

Figure 5-9. Plot of ln (J/T^2) vs $E^{1/2}$ of amorphous $SrZrO_3$ films.

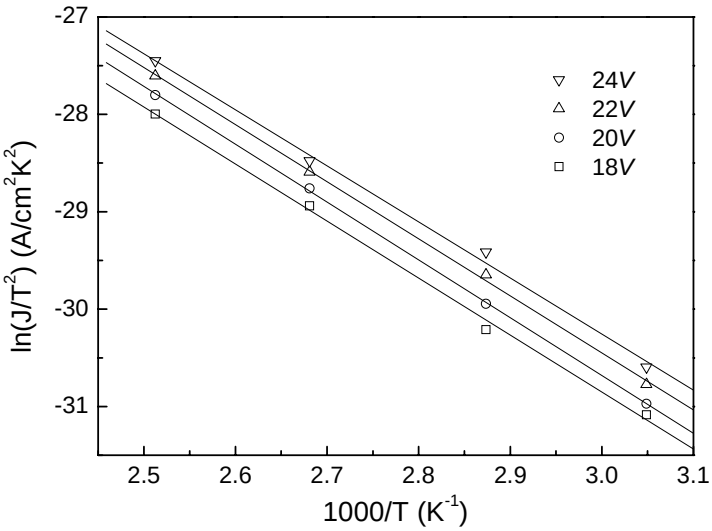

Figure 5-10. Plot of ln (J/T^2) vs 1000/T of amorphous $SrZrO_3$ films, for applied voltages of V=18, 20, 22 and 24 V.

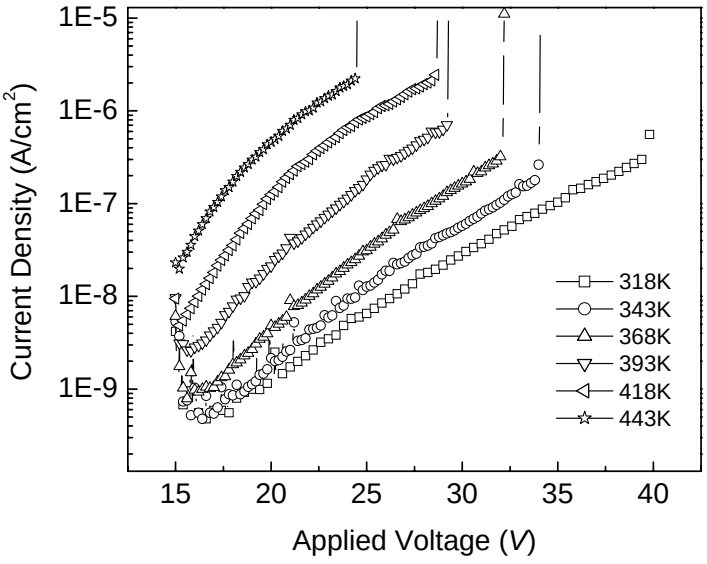

Figure 5-11. Plot of J-V of polycrystalline $SrZrO_3$ thin films at different temperatures.

The dominant conduction mechanism of the polycrystalline $SrZrO_3$ thin film (annealed at 600 °C in O_2 for 1h) at high electric fields (1.25 ~ 3.0 M*V*/cm) was investigated. The *J*-*V* characteristics of the polycrystalline $SrZrO_3$ thin films were measured at different temperatures, as shown in Figure 5-11.

Hence, to reveal the conduction mechanism more clearly, the curves in Figure 5-11 are replotted as a function of $E^{1/2}$ in Figure 5-12. It shows an almost linear relationship in the curve of ln(*J*/*V*) vs $E^{1/2}$.

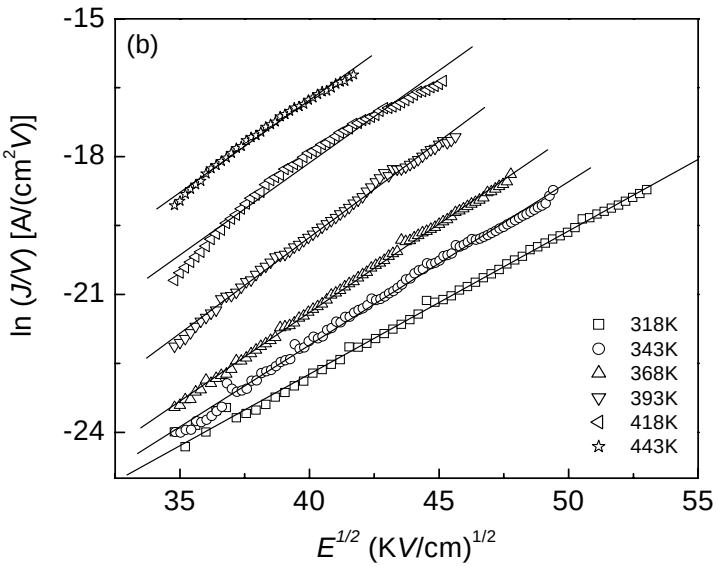

Figure 5-12. Plot of ln(*J*/*V*) vs $E^{1/2}$ of polycrystalline $SrZrO_3$ thin films.

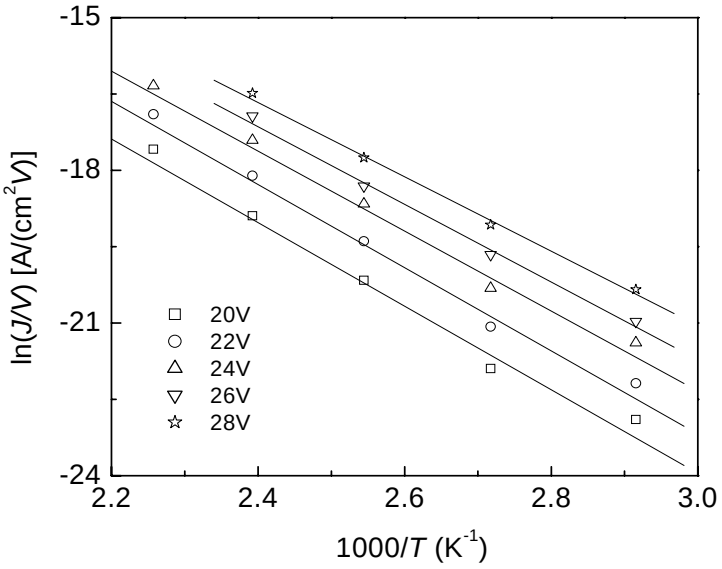

Figure 5-13. Plot of ln (*J/V*) vs 1000/*T* of polycrystalline $SrZrO_3$ thin films, for applied voltages of V=20, 22, 24, 26 and 28 *V*.

In order to confirm the leakage current mechanism, we try to fit the curve of ln(*J/V*) vs. *1/T* which is the characteristic for the Poole-Frenkel mechanism and the curve of ln(J/T^2) vs. *1/T* which is the characteristic for the Schottky mechanism. Good linearity is achieved by using the plot of ln(*J/V*) vs. *1/T* (as shown in Figure 5-13); meanwhile, the plot of ln(J/T^2) vs. *1/T* is not a straight line. Based on the curve of ln(*J/V*) vs. *1/T*, we calculated the trap level $q\phi_{pf}$ in the polycrystalline $SrZrO_3$ thin film and got a value of 0.64 e*V*. Hence, the Poole-Frenkel mechanism is dominant in polycrystalline $SrZrO_3$ thin films at high electric fields (1.25 ~ 3.0 MV/cm).

5.3.3 Effects of post-annealing on the structural and electrical properties

Based on these discussions above, it is found that the Schottky conduction mechanism is dominant in amorphous thin films and the Poole-Frenkel mechanism is dominant in polycrystalline thin films at high electric fields. Different conduction mechanisms are observed in thin films with different structural properties. There may be a certain correlation between the change of the leakage current characteristic and that in the structure of the thin films. It has been pointed out that the grain boundaries may serve as a new leakage current path and degrade the leakage current characteristic of the polycrystalline films. Thus it is reasonable to suspect that the high leakage current is induced from the high trap density in the grain boundaries.

When the magnitude of leakage current observed in polycrystalline thin film is compared with that of amorphous thin film under the same applied voltage, the value of the former is larger than that of the latter. Therefore, we infer that the number of trapped defects which are created in the polycrystalline film is rather larger than that of in amorphous film. The reason is as follows: since the thin film has polycrystalline structure as confirmed by XRD analysis, it is expected that a considerable number grain boundaries are present in the polycrystalline film. Bulk imperfections including grain boundaries, vacancies and dislocations have been relatively well studied and are known to trap charge and increase leakage current. In general, a grain boundary in an insulator becomes electrically active as a result of charge trapping by defect states

localized between two adjacent grains. Such defect states are possibly created by the crystallographic mismatch between the adjacent grains, thereby leading to boundary defects [159]. Therefore, due to larger defect density, the Poole-Frenkel conduction mechanism is confirmed dominant in the polycrystalline $CaZrO_3$ and $SrZrO_3$ thin films.

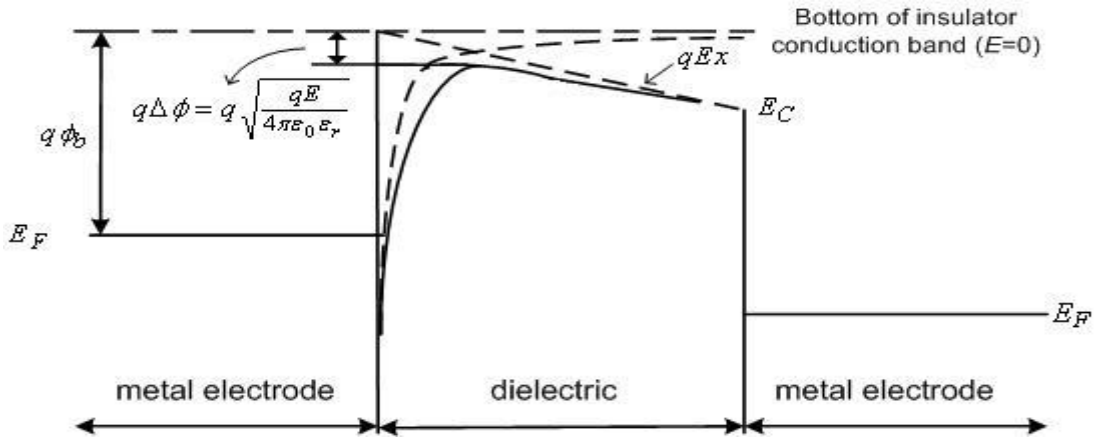

(a) Schottky mechanism [55]

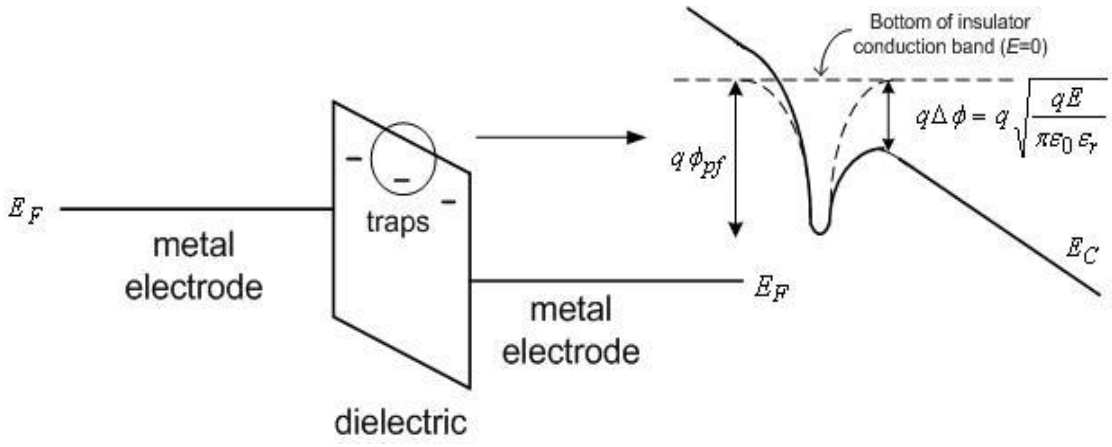

(b) Poole-Frenkel mechanism [106]

Figure 5-14. A schematic energy band diagram displaying (a) the Schottky transport mechanism and (b) the Poole-Frenkel transport mechanism.

The energy band diagrams are schematically described in Figure 5-14. In the amorphous film, a potential barrier occurs at the interface between a metal and an insulating film due to the applied field and the image force, as shown in Figure 5-14 (a). In this case, the leakage current should occur only by the thermally activated emission, and the leakage level is determined by the barrier height. Thus the conduction process is electrode-limited. In contrast, in the polycrystalline thin film, the Poole-Frenkel conduction mechanism assumes the existence of traps in the dielectric, that might be ionized and thus release a charge carrier into the conduction band. The depth of these traps $q\phi_{pf}$ is lowered, when an external field E is applied, as shown in Figure 5-14 (b). The interaction between the positively charged trap and the electrons gives rise to the Coulombic barrier [160]. When the Coulombic potential barrier is lowered by the applied electric field, the electron will be ejected from the traps to the conduction band of the dielectric by field-assisted ionization. The leakage level is determined by the availability of charge carriers in the bulk of the material. Thus the conduction process is bulk-limited. Poole-Frenkel conduction mechanism is often observed at high electric field and high temperature [161-163].

CHAPTER SIX

CONCLUSION AND RECOMMENDATIONS

6.1 Conclusion

In this thesis, $Ca_xSr_{1-x}ZrO_3$ thin films have been successfully synthesized by a sol-gel route. The phase developments and microstructures have been investigated by XRD, AFM, and FTIR. The influence of the deposition process, composition ratio and preparation conditions on the microstructure, dielectric and electric properties of $Ca_xSr_{1-x}ZrO_3$ thin films has been systematically investigated. The dielectric and electrical properties have been characterized and analyzed. The film properties are comparable to published results.

The obtained molar cation ratios in the $Ca_xSr_{1-x}ZrO_3$ thin films have been determined by EDX method. All of the XRD results and IR spectra suggest the complete

decomposition of carbonate and the growth of the perovskite phase when the $Ca_xSr_{1-x}ZrO_3$ thin films are annealed at above 600 ºC.

AES depth profiling presents clear evidence for the interdiffusion of Pt/Ti bilayer in oxidizing environments at high temperatures. Annealing in an oxidizing atmosphere causes oxidation of the intermediate Ti layer and its migration into Pt. Based on AES data, the diffusion of Ti and O in oxygen environment can be explained as follows. In the initial stage of oxygen heat-treatment, Ti diffuses from the Ti under layer, reacts with O diffused from the environment gas around the center region of Pt layer or from dissociated SiO_2 to form titanium oxide. With increase in annealing temperatures, the formation of titanium oxide increases. Higher annealing temperatures result in the formation of titanium oxide in the surface Pt grain boundaries.

Although two C1s lines are detected in the spectra, O1s referencing is found to be useful in interpreting the XPS spectra of $SrZrO_3$ and $CaZrO_3$ thin films.

Three main bands are clearly shown in the FTIR spectra. One is focused on the modes of metal-oxygen (M-O) vibrating at 400 ~ 800 cm^{-1}. CO_2 reflectance bands at 2340 and 2363 cm^{-1} approximately. The intensities of the bands at 1300 ~ 1800 cm^{-1} decrease with the increase of annealing temperature, indicating that the dissociation and evaporation of metal-organic compounds have occurred.

It is evident that post-annealing in flowing oxygen gas is useful in reducing the leakage current in the $Ca_xSr_{1-x}ZrO_3$ thin films. The lowest leakage current densities of the $CaZrO_3$ thin films post-annealed in air and O_2 atmosphere are approximately 1×10^{-8} A/cm^2 and 1×10^{-9} A/cm^2 at 1 M*V*/cm, respectively. $CaZrO_3$ thin films show good electrical properties in terms of a dielectric constant of about 20 and leakage current density of 1×10^{-7} A/cm^2 at a high applied electric field of 2.6 M*V*/cm. The Schottky mechanism dominates in amorphous $CaZrO_3$ and $SrZrO_3$ thin films at high electric fields. On the other hand, the Poole-Frenkel mechanism is dominant in polycrystalline $CaZrO_3$ and $SrZrO_3$ thin films at high electric fields.

Compared to ZrO_2 oxide thin films, $Ca_xSr_{1-x}ZrO_3$ thin films show higher crystallization temperatures and lower leakage current densities. With their relatively high and stable dielectric constants, $Ca_xSr_{1-x}ZrO_3$ thin films are promising candidates for high-k microelectronic device applications.

6.2 Recommendations for future work

It is evident in this thesis that the studies on the sol-gel $Ca_xSr_{1-x}ZrO_3$ thin films exhibit a good prospect for potential high-k microelectronic device applications. The future work towards the next generation gate dielectric and high-density capacitors as outlined below is highly recommended.

The $Ca_xSr_{1-x}ZrO_3$ thin films exhibit relatively high dielectric constant and low leakage behaviors. Meanwhile, we have also noted in this thesis that the dielectric constant of $Ca_xSr_{1-x}ZrO_3$ thin films is nearly independent of frequency and applied field, which is suitable for capacitor in practical high-k devices use. Therefore, it is suggested to extend the study on optimizing the electrical and dielectric properties of the $Ca_xSr_{1-x}ZrO_3$ system. Moreover, some device-related issues such as reliability and the control of carrier mobility are needed to be considered for the fabrication of the dielectric thin films on silicon since the current study mainly addresses to the physical properties of this material system.

An amorphous structure is the ideal one for the gate dielectric, so it needs the dielectric materials have high crystallization temperature to keep amorphous during high-temperature processing. From the results described above, it can be seen that the sol-gel technology is not suitable for ultra-thin high-k film deposition because it will lower the crystallization temperature of the dielectric material, and form silicon dioxide on Si substrates easily due to certain amount of H_2O and carbon and oxygen in precursor solutions.

Compared with chemical vapor deposition (CVD) and chemical solution deposition (CSD) methods, molecular beam epitaxy (MBE) method is indeed an ideal growth technique for studying new materials as it does not need any sophisticated chemicals.

It would maybe possible to grow ultra-thin high-k dielectric epitaxially on silicon. This result could offer advantages such as higher dielectric constant and better control of interfaces with respect to other growth techniques. Several requirements related to electrical and structural properties, interface engineering and thermal stability must be fulfilled. To address these issues the use of complementary characterization techniques is mandatory and in particular surface sensitive techniques are requested to investigate the composition and the micro-structure of ultra-thin films on silicon. AES is recommended for determining the composition of the ultra-thin film precisely. Future work on the high-k dielectric thin film using MBE technology is highly suggested to get the equivalent thickness of the ultra-thin film below 1 nanometer.

AUTHOR'S PUBLICATIONS

Journal Papers:

[1] **T. Yu**, W. G. Zhu, C. H. Chen, X. F. Chen, and R. G. Krishnan, "Preparation and characterization of sol-gel derived $CaZrO_3$ dielectric thin films for high-k applications", Physica B, 348 (2004) 440.

[2] **T. Yu**, W. G. Zhu, C. H. Chen, X. F. Chen, and R. G. Krishnan, "Fabrication and characterization of perovskite $CaZrO_3$ oxide thin films", Ceramics International, 30 (2004) 1279.

[3] W. Zhu, **T**. **Yu**, C. H. Chen, X. F. Chen and R. G. Krishnan, "Preparation and characterizations of high-k $(Ca,Sr)ZrO_3$ gate dielectric thin films by sol-gel technology"， Integrated Ferroelectrics, 61 (2004) 25.

[4] Y. K. Lu, C. H. Chen, W. Zhu, **T. Yu** and X. F. Chen, "Structural and electric properties of $SrZrO_3$ thin films on different Pt bottom electrodes", Ceramics International, 30 (2004) 1547.

[5] C. H. Chen, W. Zhu, **T. Yu**, X. F. Chen, and X. Yao, "Preparation of metal-organic decomposition-derived strontium zirconate dielectric thin films",

Appl. Surf. Sci., 211 (2003) 244.

[6] C. H. Chen, W. Zhu, **T. Yu**, X. F. Chen, X. Yao, and R. G. Krishnan, "FT-IR, structure and dielectric property investigation of strontium zirconate thin films prepared by MOD technique", Surface and Coatings Technology, 167 (2003) 245.

[7] C. H. Chen, W. Zhu, **T. Yu**, X. F. Chen, and X. Yao, "Preparation and characteristic study of MOD derived dielectric $SrZrO_3$ thin films", Ferroelectrics, 292 (2003) 29.

Conference Papers:

[1] **T. Yu**, W. G. Zhu, X. F. Chen and Y. K. Lu, "Leakage current behavior in $CaZrO_3$ thin films for high-k applications", 2004 MRS spring meeting, San Francisco, USA, April 2004.

[2] **T. Yu**, C. H. Chen, X. F. Chen, W.G. Zhu, and R. G. Krishnan, "Preparation and characterizations of high-k gate dielectric $CaZrO_3$ thin films by sol-gel technology", Characterization and Metrology for ULSI Technology 2003 International Conference, Austin, TX, USA, March 2003.

[3] W. Zhu, C. H. Chen, **T. Yu**, and R. G. Krishnan, "Preparation and characterizations of high-k $(Ca,Sr)ZrO_3$ gate dielectric thin films by sol-gel technology", The 10th European Meeting on Ferroelectricity, Cambridge, UK, August 2003.

[4] C. H. Chen, W. Zhu, **T. Yu**, X. F. Chen, and Y. K. Lu, "Metallo-organic decomposition derived $Sr_{0.95}Ca_{0.05}ZrO_3$ oxide thin films on $Pt/Ti/SiO_2/Si$

substrate", 2002 Conference on Optoelectronic and Microelectronic Materials and Devices, COMMAD 2002 Proceedings, (2002) 169.

BIBLIOGRAPHY

[1] G. Moore, "Progress in digital integrated electronics", Tech. Dig. IEEE. Electron Device Meeting, (1975) 11.

[2] International Technology Roadmap for Semiconductor (SIA Roadmaps), San Jose, CA, 2001.

[3] P. A. Packan, "Pushing the limits", Science, 285 (1999) 2079.

[4] J. Maserjian, G. P. Petersson, "Tunneling through thin MOS structures: Dependence on energy (E-Φ)", Appl. Phys. Lett., 25 (1974) 50.

[5] H. S. Momose, M. Ono, T. Yoshitomi, T. Ohguro, S-I. Nakamura, M. Saito, and H. Iwai, "Tunneling gate oxide approach to ultra-high current drive in small-geometry MOSFETs", Tech. Dig. IEEE Electron Device Meeting, (1994) 593.

[6] D. A. Buchanan and S. H. Lo, "Reliability and integration of ultra-thin gate dielectrics for advanced CMOS", Microelectron. Eng., 36 (1997) 13.

[7] S. S. Pandit, A. Weyl, and D. Janke, "High-temperature ionic and electronic conduction in zirconate and hafnate compounds", Solid State Ionics, 69 (1994) 93.

[8] S. Yamaguchi, K. Kobayashi, T. Higuchi, S. Shin, and Y. Iguchi, "Electronic transport properties and electronic structure of $InO_{1.5}$-doped $CaZrO_3$", Solid State Ionics, 136-137 (2000) 305.

[9] T. Yajima, H. Kazeoka, T. Yogo and H. Iwahara, "Proton conduction in sintered oxides based on $CaZrO_3$", Solid State Ionics, 47 (1991) 271.

[10] T. Yajima, H. Iwahara, K. Koide, and K. Yamamoto, "$CaZrO_3$-type hydrogen and steam sensors: trial fabrication and their characteristics", Sensors and Acutators, B5 (1991) 145.

[11] T. Hibino, K. Mizutani, T. Yajima, and H. Iwahara, "Evaluation of proton conductivity in $SrCeO_3$, $BaCeO_3$, $CaZrO_3$ and $SrZrO_3$ by temperature programmed desorption method", Solid State Ionics, 57 (1992) 303.

[12] T. Chiang, C. C. Wang and S. A. Akbar, "Calcium zirconate for the monitoring of hydrocarbons", Sensors and Acutators B, 46 (1998) 208.

[13] C. C. Wang, S. A. Akbar, W. Chen, and J. R. Schorr, "High-temperature thermistors based on yttria and calcium zirconate", Sensors and Acutators, A58 (1997) 237.

[14] T. Yamaguchi, Y. Komatsu, T. Otobe, and Y. Murakami, "Newly developed ternary (Ca, Sr, Ba) zirconate ceramic system for microwave resonators", Ferroelectrics, 27 (1980) 273.

[15] H. S. Wong, D. J. Frank, P. M. W. Solomon, H.J. Clement, and J. J. Welser, "Nanoscale CMOS", Proc. IEEE., 87 (1999) 537.

[16] C. J. Frosch and L. Derick, "Surface protection and selective masking during diffusion in silicon", Proceedings of the Electrochemical Society, 104 (1957) 547.

[17] M. M. Atalla, E. Tannenbaum, and E. J. Scheibner, "Stabilization of silicon surfaces by thermally grown oxides", Bell Syst. Tech. J., 38 (1959) 749.

[18] J. R. Ligenza and W. G. Spitzer, "The mechanisms for silicon oxidation in steam and oxygen", J. Phys. Chem. Solids, 14 (1960) 131.

[19] J. R. Ligenza and W. G. Spiter, "Effects of crystal orientation on oxidation rates of silicon in high pressure steam", J. Phys. Chem., 65 (1961) 2011.

[20] H. S. Wong and Y. Taur, "Three-dimensional "atomistic" simulation of discrete random dopant distribution effects in sub-0.1 μm MOSFET's", IEEE Tech. Dig., (1993) 705.

[21] D. A. Buchanan and S. H. Lo, "Characterization and the limits of ultrathin SiO_2 based dielectrics for future CMOS applications", presented at the Symposium on the Physics and Chemistry of SiO_2 and the Si-SiO_2 Interface, Los Angeles, 1996.

[22] E. L. Lakomaa, S. Haukka, and T. Suntola, "Atomic layer growth of TiO_2 on silica", Appl. Surf. Sci., 60/61(1992) 742.

[23] M. B. Lee, M. Kawasaki, and H. Koinuma, "Formation and characterization of epitaxial TiO_2 and $BaTiO_3/TiO_2$ films on Si substrate", Jpn. J. Appl. Phys., 34 (1995) 808.

[24] H. S. Kim, D. C. Gilmer and D. L. Polla, "Leakage current and electrical breakdown in metal-organic chemical vapor deposited TiO_2 dielectrics on silicon substrates", Appl. Phys. Lett., 69 (1996) 3860.

[25] S. Chen, M. G. Mason, H. J. Gysling, G. R. Paz-Pujalt, T. N. Blanton, T. Castro, K. M. Chen, C. P. Fictorie, W. L. Gladfelter, A. Franciosi, P. I. Cohen, and J. F. Evans, "Ultrahigh vacuum metalorganic chemical vapor deposition growth and in situ characterization of epitaxial TiO_2 films", J. Vac. Sci. Technol., 11 (1993) 2419.

[26] S. A. Campbell, D.C. Gilmer, X. C. Wang, M. T. Hsieh, H. S. Kim, W. Gladfelter, and J. Yan, "MOSFET transistors fabricated with high permittivity TiO_2 dielectrics", IEEE Trans. Electron Devices, 44 (1997) 104.

[27] K. W. Kwon, C. S. Kang, and S. T. Ahn, "Thermally robust Ta_2O_5 capacitor for the 256-Mbit DRAM", IEEE Trans. Electron Devices, 43 (1996) 919.

[28] K. Sundaram, W. K. Choi, and C. H. Ling, "Quasi-static and high-frequency *C-V* measurements on $Al/Ta_2O_5/SiO_2/Si$", Thin Solid Films, 230 (1993) 145.

[29] J. G. Hwu and S. T. Lin, "Electrical characterisation of the insulating property of Ta_2O_5 in $Al\text{-}Ta_2O_5\text{-}SiO_2\text{-}Si$ capacitors by a low-frequency C/V technique", IEEE Proc. G. Circuits. Devices & Syst., 137 (1990) 390.

[30] S. Zaima, T. Furuta, and Y. Koide, "Conduction mechanism of leakage current in Ta_2O_5 films on Si prepared by LPCVD", J. Electrochem. Soc., 137 (1990) 2876.

[31] J. L. Autran, R. Devine, C. Chaneliere, and B. Balland, "Fabrication and characterization of Si-MOSFETs with PECVD amorphous Ta_2O_5 gate Insulator", IEEE Electron. Device. Lett., 18 (1997) 447.

[32] K. A. Son, A. Y. Mao, Y. M. Sun, B. Y. Kim, F. Liu, A. Kamath, J. M. White, D. L. Kwong, D. A. Roberts, and R. *N*. Vritis, "Chemical vapor deposition of ultrathin Ta_2O_5 films using $Ta[N(CH_3)_2]_5$", Appl. Phys. Lett., 72 (1998) 1187.

[33] S. D. Khanin and A. L. Ivanovskii, "The influence of structural defects on the electronic properties of amorphous Ta_2O_5", Phys. Status. Solidi, 174 (1992) 449.

[34] I. Kim, J. S. Kim, O. S. Kwon, S. T. Ahn, J. S. Chun, and W. J. Lee, "Effects of annealing in O_2 and N_2 on the electrical properties of tantalum oxide thin films prepared by electron cyclotron resonance plasma enhanced chemical vapor deposition", J. Electron. Mater., 24 (1995) 1435.

[35] G. Q. Lo, D. L. Kwong, and S. Lee, "Metal-oxide-semiconductor characteristics of chemical vapor deposited Ta_2O_5 films", Appl. Phys. Lett., 60 (1992) 3287.

[36] G. Q. Lo, D. L. Kwong, and S. Lee, "Reliability characteristics of MOS capacitors with chemical vapor deposited Ta_2O_5 gate dielectrics", Appl. Phys. Lett., 62 (1993) 973.

[37] G. B. Alers, R. M. Fleming, Y. H. Wong, B. Dennis, A. Pinczuk, G. Redinbo, R. Urdahl, E. Ong, and Z. Hasan, "Nitrogen plasma annealing for low temperature Ta_2O_5 films", Appl. Phys. Lett., 72 (1998) 1308.

[38] G. B. Alers, D. J. Werder, Y. Chabal, H. C. Lu, E. P. Gusev, E. Garfunkel, T. Gustafsson, and R. Urdahl, "Intermixing at the tantalum oxide/silicon interface in gate dielectric structures", Appl. Phys. Lett., 73 (1998) 1517.

[39] C. W. Liang, T. C. Luo, M. S. Feng, H. C. Cheng, and D. Su, "Characterization of anodic aluminum oxide film and its application to amorphous silicon thin film transistors", Mater. Chem. Phys., 43 (1996) 166.

[40] J. Kolodzey, E. A. Chowdhury, T. N. Adam, G. H. Qui, I. Rau, J. O. Olowolafe, J. S. Suehle, and Y. Chen, "Electrical conduction and dielectric breakdown in aluminum oxide insulators on silicon", IEEE Trans. Electron Devices, 47 (2000) 121.

[41] L. A. Ragnarsson, S. Guha, N. A. Bojarczuk, E. Cartier, M. V. Fischetti, K. Rim, and J. Karasinski, "Electrical characterization of Al_2O_3 n-channel MOSFETs with aluminum gates", IEEE Electron Device. Lett., 22 (2001) 490.

[42] M. Shahjahan, N. Takahashi, K. Sawada, and M. Ishida, "Fabrication and electrical characterization of ultrathin crystalline Al_2O_3 gate dielectric films on Si(100) and Si(111) by molecular beam epitaxy", Jpn. J. Appl. Phys., part 2, 41 (2002) 1474.

[43] W. J. Qi, R. Nieh, B. H. Lee, L. G. Kang, Y. Jeon, and J. C. Lee , "Electrical and reliability characteristics of ZrO_2 deposited directly on Si for gate dielectric application", Appl. Phys. Lett., 77 (2000) 3269.

[44] Y. Kim, J. Koo, J. W. Han, S. Choi, H. Jeon, and C. G. Park, "Characteristics of ZrO_2 gate dielectric deposited using Zr t-butoxide and Zr(NEt2)(4) precursors by plasma enhanced atomic layer deposition method", J. Appl. Lett., 92 (2002) 5443.

[45] Y. S. Lin, R. Puthenkovilakam, J. P. Chang, C. Bouldin, I. Levin, N.V. Nguyen, J. Ehrstein, Y. Sun, P. Pianetta, T. Conard, W. Vandervorst, V. Venturo, and S. Selbrede, "Interfacial properties of ZrO_2 on silicon", J. Appl. Lett., part 1, 93 (2003) 5945.

[46] S. W. Nam, J. H. Yoo, S. Nam, D. H. Ko, C. W. Yang, and J. H. Ku, "Characteristics of ZrO_2 films with Al and Pt gate electrodes", J. Electrochem. Soc., 150 (2003) 849.

[47] H. Lee, S. Jeon, and H. Hwang, "Electrical characteristics of a Dy-doped HfO_2 gate dielectric", Appl. Phys. Lett., 79 (2001) 2615.

[48] M. L. Green, M. Y. Ho, B. Busch, G. D. Wilk, T. Sorsch, T. Conard, B. Brijs, W. Vandervorst, P. I. Raisanen, D. Muller, M. Bude, and J. Grazul, "Nucleation and growth of atomic layer deposited HfO_2 gate dielectric layers on chemical oxide (Si-O-H) and thermal oxide (SiO_2 or Si-O-N) underlayers", J. Appl. Phys., 92 (2002) 7168.

[49] Y. H. Kim, K. Onishi, C. S. Kang, H. J. Cho, R. Choi, S. Krishnan, M. S. Akbar, and J. C. Lee, "Thickness dependence of Weibull slopes of HfO_2 gate dielectrics", IEEE Electron Device Letters, 24 (2003) 40.

[50] J. K. Schaeffer, S. B. Samavedam, D. C. Gilmer, V. Dhandapani, P. J. Tobin, J. Mogab, B. Y. Nguyen, B. E. White, S. Dakshina-Murthy, R. S. Rai, Z. X. Jiang , R. Martin, M. V. Raymond, M. Zavala, L. B. La, J. A. Smith, R. Garcia, D. Roan, M. Kottke, and R. B. Gregory, "Physical and electrical properties of metal gate electrodes on HfO_2 gate dielectrics", J. Vac. Sci& Tech B., 21 (2003) 11.

[51] M. Yang, E. P. Gusev, M. K. Ieong, O. Gluschenkov, D. C. Boyd, K. K. Chan, P. M. Kozlowski, C. P. D'Emic, R. M. Sicina, P. C. Jamison, and A. I. Chou, "Performance dependence of CMOS on silicon substrate orientation for ultrathin oxynitride and HfO_2 gate dielectrics", IEEE Electron Device Letters, 24 (2003) 339.

[52] E. P. Gusev, C. Cabral, M. Copel, C. D'Emic, and M. Gribelyuk, "Ultrathin HfO_2 films grown on silicon by atomic layer deposition for advanced gate dielectrics applications", Microelectron. Eng., 69 (2003) 145.

[53] J. Senzaki, K. Kurihara, N. Nomura, O. Mitsunaga, Y. Iwasaki, and T. Ueno, "Characterization of $Pb(Zr,Ti)O_3$ thin films on Si substrates using MgO intermediate layer for metal/ferroelectric/insulator/semiconductor field effect transistor devices", Jpn. J. Appl. Lett., part 1, 37 (1998) 5150.

[54] S. M. Koo, S. I. Khartsev, C. M. Zetterling, A. M. Grishin, and M. Ostling, "Processing and properties of ferroelectric $Pb(Zr,Ti)O_3$/silicon carbide field-effect transistor", Integrated Ferroelectrics, 57 (2003) 1221.

[55] S. M. Sze, "Physics of semiconductor devices", Wiley, (1981).

[56] E. H. Nicollian and J. R. Brews, "MOS (metal oxide semiconductor) physics and technology", Wiley, (1982).

[57] E. P. Gusev, M. Copel, E. Cartier, I. J. R. Baumvol, C. Krug, and M. A. Gribelyuk, "High-resolution depth profiling in ultrathin Al_2O_3 films on Si", Appl. Phys. Lett., 76 (2000) 176.

[58] D. A. Buchanan, E. P. Gusev, E. Cartier, H. O. Schmidt, K. Rim, M. A. Gribelyuk, A. Mocuta, A. Ajmera, M. Copel, S. Guha et al., "80 nm polysilicon gated n-FETs with ultra-thin Al_2O_3 gate dielectric for ULSI applications", Tech. Dig. Int. Eletron Devices Meet., (2000) 223.

[59] K. J. Hubbard and D. G. Schlom, "Thermodynamic stability of binary oxides in contact with silicon", J. Mater. Res., 11(1996) 2757.

[60] International Reliability Physics Symposium (2003).

[61] C. Lin, A. I. Chou, P. Choudhury, J. C. Lee, K. Kumar, B. Doyle, and H. R. Soleiman, "Reliability of gate oxide grown on nitrogen-implanted Si substrates", Appl. Phys. Lett., 69 (1996) 3701.

[62] D. C. Gilmer, R. Hegde, R. Cotton, R. Garcia, V. Dhandapani, D. Triyoso, D. Roan, A. Franke, R. Rai, L. Prabhu, C. Hobbs, J. M. Grant, L. La, S. Samavedam, B. Taylor, H. Tseng, and P. Tobin, "Compatibility of polycrystalline silicon gate deposition with HfO_2 and Al_2O_3/HfO_2 gate dielectrics", Appl. Phys. Lett., 81 (2002) 1288.

[63] W. M. Robert, I. G. Mark, A. B. George, M. Z. Peter, R. H. Howard, "Challenges in gate stack engineering", Solid State Tech., 46 (2003) 43.

[64] S. Zaima, T. Furata, and Y. Koide, "Conduction mechanism of leakage current in Ta_2O_5 films on Si prepared by LPCVD", J. Electronchem. Soc., 137, (1990) 2876.

[65] C. H. Ling, "Interfacial polarisation in Al-Y_2O_3-SiO_2-Si capacitor", Electron Lett., 29 (1993) 1676.

[66] K. Onisawa, M. Fuyama and K. Tamura, "Dielectric properties of rf-sputtered Y_2O_3 thin film-Si(100) interfaces", J. Appl. Phys., 68 (1990) 719.

[67] C. J. Taylor, D. C. Gilmer, D. Colombo, G. D. Wilk, S. A. Campbell, J. Roberts, and W. L. Gladfelter, "Does chemistry really matter in the chemical vapor deposition of titanium dioxide? Precursor and kinetic effects on the microstructure of polycrystalline films", J. Am. Chem. Soc., 121 (1999) 5220.

[68] L. Manchanda and M. Gurvitch, "Yttrium oxide/silicon dioxide: a new dielectric structure for VLSI/ULSI circuits", IEEE Electron Device Letters, 9 (1988) 180.

[69] M. Gurvitch, L. Manchanda, and J. M. Gibson, "Study of thermally oxidized yttrium films on silicon", Appl. Phys. Lett., 51 (1987) 919.

[70] R. Beyers, "Thermodynamic considerations in refractory metal-silicon-oxygen systems", J. Appl. Phys., 56 (1984) 147.

[71] K. J. Hubbard and D. G. Schlom, "Thermodynamic stability of binary oxides in contact with silicon", J. Mater. Res., 11 (1996) 2757.

[72] S. Q. Wang and J. W. Mayer, "Reactions of Zr thin films with SiO_2 substrates", J. Appl. Phys., 64 (1988) 4711.

[73] M. Gutowski, J. E. Jaffe, C. L. Liu, M. Stoker, R. I. Hegde, R. S. Rai, and P. J. Tobin, "Thermodynamic stability of high-K dielectric metal oxides ZrO_2 and HfO_2 in contact with Si and SiO_2", Appl. Phys. Lett., 80 (2002) 1897.

[74] G. D. Wilk, R. M. Wallace, and J. M. Anthony, "Hafnium and zirconium silicates for advanced gate dielectrics", J. Appl. Phys., 87 (2000) 484.

[75] R. H. Dennard, F. H. Gaensslen, H. N. Yu, V. l. Rideout, E. Barsous, and A. R. LeBlanc, "Design of ion-implanted MOSFETs with very small physical dimensions", IEEE J. Solid-State Circuits, SC-9 (1974) 256.

[76] H. S. Momose, T. Morimoto, Y. Ozawa, K. Yamabe, and H. Iwai, "Electrical characteristics of rapid thermal nitrided-oxide gate n- and p-MOSFET's with less than 1 atom% nitrogen concentration", IEEE Trans. Electron Devices, 41 (1995) 546.

[77] M. Copel, M. A. Gribelyuk, and E. Gusev, "Structure and stability of ultrathin zirconium oxide layers on Si(001)", Appl. Phys. Lett., 76 (2000) 436.

[78] Y. Takeshi, L. Ryosuke, I. Tsunehiro, N. Akira, S. Hideki, and F. Noburu, "Additional scattering effects for mobility degradation in Hf-silicate gate MISFETs", Tech. Dig. Int. Eletron Devices Meet., (2002) 621.

[79] K. Eisenbeiser, J. M. Finder, Z. Yu, J. Ramdani, J. A. Curless, J. A. Hallmark, R. Droopad, W. J. Ooms, L. Salem, S. Bradshaw, and C. D. Overgaard, "Field effect transistors with $SrTiO_3$ gate dielectric on Si ", Appl. Phys. Lett., 76 (2000) 1324.

[80] J. Kwo, M. Hong, A. R. Kortan, K. T. Queeney, Y. J. Chabal, J. P. Mannaerts, T. Boone, J. J. Krajewski, A. M. Sergent, and J. M. Rosamilia, "High ε gate dielectrics Gd_2O_3 and Y_2O_3 for silicon", Appl. Phys. Lett., 77 (2000) 130.

[81] M. R. Visokay, J. J. Chambers, A. L. P. Rotondaro, A. Shanware, and L. Colombo, "Application of HfSiON as a gate dielectric material", Appl. Phys. Lett., 80 (2002) 3183.

[82] G. D. Wilk and R.M. Wallace, "Electrical properties of hafnium silicate gate dielectrics deposited directly on silicon", Appl. Phys. Lett., 74 (1999) 2854.

[83] M. S. Joo, B. J. Cho, C. C. Yeo, D. S. H. Chan, S. J. Whoang, S. Mathew, L. K. Bera, N. Balasubramanian, and D. L. Kwong, "Formation of hafnium-aluminum-oxide gate dielectric using single cocktail liquid source in MOCVD process", IEEE. Trans. Electron Devices, 50 (2003) 2088.

[84] S. J. Wang, C. K. Ong, S. Y. Xu, P. Chen, W. C. Tjiu, J. W. Chai, A. C. H. Huan, W. J. Yoo, J. S. Lim, W. Feng, and W. K. Choi, "Crystalline zirconia oxide on silicon as alternative gate dielectrics", Appl. Phys. Lett., 78 (2001) 1604.

[85] D. J. DiMaria and J. H. Stathis, “Ultimate limit for defect generation in ultra-thin silicon dioxide”, Appl. Phys. Lett., 71 (1997) 3230.

[86] J. H. Stathis and D. J. DiMaria, "Oxide scaling limit for future logic and memory technology", Microelectron. Eng., 48 (1999) 395.

[87] Y. Yamamura, S. Kawasaki, and H. Sakai, “Molecular dynamics analysis of ionic conduction mechanism in yttria-stabilized zirconia”, Solid State Ionics, 126 (1999) 181.

[88] T. Osaka, C. Numako, and K. Koto, “Local structure and thermal study of ytterbium-doped $SrZrO_3$”, Mater. Res. Bull., 34 (1999) 11.

[89] W. Engelen, A. Buekenhoudt, J. Luyten, and F. De Schutter, “Humidity sensitivity of electrochemical hydrogen cells using calcium zirconate ceramics”, Solid State Ionics, 96 (1997) 55.

[90] V. Longo, F. Richiasdiello, and O. Shaizero, “Science of ceramics II”, Swedish Ceramic Society, (1981).

[91] J. Nair, P. Nair, E. B. M. Doesburg, J. G. VAN Ommen, J. R. H. Ross, A. J. Burggraaf, and F. Mizukami, “Preparation and characterization of lanthanum zirconate”, J. Mater. Sci., 33 (1998) 4517.

[92] H. J. A. Koopmans, G. M. H. van de Velde, and P. J. Gellings, “Powder neutron diffraction study of the perovskites $CaTiO_3$ and $CaZrO_3$”, Acta Crystallogr. Sect. C, 39 (1983) 1323.

[93] R. A. Davies, M. S. Islam, and J. D. Gale, “Dopant and proton incorporation in perovskite-type zirconates”, Solid State Ionics, 126 (1999) 323.

[94] M. Joseph, N. Sivakumar, P. Manoravi, and S. Vanavaramban, “Preparation of thin film of $CaZrO_3$ by pulsed laser deposition”, Solid State Ionics, 144 (2001) 339.

[95] S. Zafar, R. E. Jones, B. Jiang, B. White, V. Kaushik, and S. Gillespie, “The electronic conduction mechanism in barium strontium titanate thin films”, Appl. Phys. Lett., 73 (1998) 3533.

[96] S. I. Jang and H. M. Jang, “Structure and electrical properties of boron-added $(Ba,Sr)TiO_3$ thin films fabricated by the sol-gel method”, Thin Solid Films, 330 (1998) 89.

[97] C. S. Hwang, B. T. Lee, C. S. Kang, K. H. Lee, H. J. Cho, H. Hideki, W. D. Kim, S. I. Lee, and M. Y. Lee, "Depletion layer thickness and Schottky type carrier injection at the interface between Pt electrodes and (Ba,Sr)TiO_3 thin films", J. Appl. Phys., 85 (1999) 287.

[98] G. C. Chao and J. M. Wu, "Leakage current and fatigue properties of Pb(Zr,Ti)O_3 ferroelectric films prepared by RF-magnetron sputtering on textured $LaNiO_3$ electrode", Jpn. J. Appl. Phys., 40 (2001) 2417.

[99] K. H. Yoon, J. H. Park, and J.H. Jang, "Solution deposition processing and electrical properties of $Ba(Ti_{1-x}Sn_x)O_3$ thin films", J. Mater. Res., 14 (1999) 2933.

[100] H. Yang, B. Chen, K. Tao, X. G. Qiu, B. Xu, and B. Zhao, "Temperature- and field-dependent leakage current of Pt/$(Ba_{0.7}Sr_{0.3})TiO_3$ interface", Appl. Phys. Lett., 83 (2003) 1611.

[101] S. Y. Yang, J. S. Lee, S. H. Kim, G. B. Chae, and M. S. Jang, "Ferroelectricity and electric conduction characteristics of Sr-modified lead zirconate titanate thin film capacitors", Jpn. J. Appl. Lett., 36 (1997) 749.

[102] X. G. Tang, J. Wang, Y. W. Zhang, H. L. W. Chan, A. L. Ding, and C. L. Choy, "Leakage current and pyroelectric properties of compositionally graded (Pb,Ca)TiO_3 films", Appl. Phys. A., 78 (2004) 1205.

[103] F. M. Pontes, E. R. Leite, E. J. H. Lee, E. Longo, and J. A. Varela, "Preparation, microstructural and electrical characterization of $SrTiO_3$ thin films prepared by chemical route", J. Eur. Ceram. Soc., 21 (2001) 419.

[104] C. B. Samantaray, A. Dhar, M. L. Mukherjee, D. Bhattacharya, and S. K. Ray, "RF magnetron sputtered high-k barium strontium titanate thin films on magnetoresistive $La_{0.7}Ca_{0.3}MnO_3$ electrode", Mater. Sci. Eng. B, 88 (2002) 14.

[105] B. Panda, C. B. Samantaray, A. Dhar, S. K. Ray, and D. Bhattacharya, "Electrical properties of r.f. magnetron sputtered $Ba_xSr_{1-x}TiO_3$ films on multi-layered bottom electrodes for high-density memory application", J. Mater. Sci., 13 (2002) 263.

[106] G. G. Raju, "Dielectrics in electric fields", Marcel Dekker, New York, 2003.

[107] Proceedings of the Thorium Fuel Cycle Symposium, Gatlinburg, Tennessee, Dec 5-7, TID 7650, book II, (1962) 519.

[108] M. E. A. Hermans, ibid, (1968) 21.

[109] M. A. Aegerter, M. J. Jafelicci, D. F. Souza, and E. D. Zanotto, "Sol-gel science and technology", World Scientific, New York, 1989.

[110] L. H. Hench and J. K. West, "The sol-gel process", Chem. Rev., 90 (1990) 33.

[111] J. G. Yoon, Y. J. Kwag and H. K. Kim, "Structural characterization of sol-gel derived MgO thin film on Si substrate", J. Kor. Phys. Soc., 31 (1997) 613.

[112] C. R. Cho, S. I. Kwun, T. W. Noh and M. S. Jang, "Electric properties of sol-gel deposited $BaTiO_3$ thin films on Si (100) substrates", Jpn. J. Appl. Phys, 36 (1997) 2196.

[113] L. Van Rij, L. Winubst, L. Jun, and J. Schoonman, "Analysis of the preparation of In-doped $CaZrO_3$ using a peroxo-oxalate complexation method", J. Mater. Chem. 10 (2000) 2515.

[114] H. S. Potdar, S. B. Deshpande, A. J. Patil, A. S. Deshpande, Y. B. Khollam, and S. K. Date, "Preparation and characterization of strontium zirconate ($SrZrO_3$) fine powders", Mater. Chem. Phys., 65 (2000) 178.

[115] J. R. Hellmann and V. S. Stubican, "Stable and metastable phase relations in the system ZrO_2-CaO", J. Am. Ceram. Soc., 66 (1983) 260.

[116] V. S. Stubican and J. R. Hellmann, "Defects and ordering in zirconia crystalline solutions", Mater. Sci. Monogr., 10 (1982) 257.

[117] V. S. Stubican and S. P. Ray, "Phase equilibria and ordering in the system ZrO_2-CaO", J. Am. Ceram. Soc., 60 (1977) 534.

[118] M. H. Yeh, K. S. Liu, and I. N. Lin, "Structure and dielectric properties of $SrTiO_3$ films prepared by pulsed laser deposition technique", Jpn. J. Appl. Phys., 34 (1995) 2447.

[119] J. P. Wang, Y. C. Ling, M. H. Yeh, K. S. Liu, and I. N. Lin, "$SrTiO_3$ buffering effect on $Pb_{1-x}La_xTiO_3$ thin films prepared by pulsed laser deposition", Appl. Phys. Lett., 68 (1996) 3401.

[120] FÈ. Laura, G. Norga, and D. J. Wouters, "Absorption-reflection infrared spectroscopy studies of sol-gel prepared ferroelectric $Pb(Zr,Ti)O_3$ thin films on Pt electrodes", J. Sol-gel Sci & Tech., 19 (2000) 149.

[121] J. S. Lee, H. J. Kwon, Y. W. Jeong, H. H. Kim, K. H. Park, and C. Y. Kim, "Microstructural characterization of Pt/Ti and RuO_2 electrodes on SiO_2/Si annealed in the oxygen ambient", Mater. Res. Soc. Symp., 433 (1996) 175.

[122] H. J. Nam, H. H. Kim, and W. J. Lee, "The effects of the preparation conditions and heat-treatment conditions of Pt/Ti/SiO_2/Si substrates on the nucleation and growth of Pb(Zr,Ti)O_3 films", Jpn. J. Appl. Phys., 37 (1998) 3462.

[123] S. B. Quadri, E. F. Skelton, D. Hsu, A. D. Dinsmore, J. Yang, H. F. Gray, and B. R. Ratna, "Size-induced transition-temperature reduction in nanoparticles of ZnS", Phys. Rev. B., 60 (1999) 9191.

[124] W. M. Riggs and M. J. arker, "Methods of surface analysis", edited by A. W. Czanderna, Elsevier, Amsterdam, 1975.

[125] M. P. Seah, P. W. Swift, and D. Shuttleworth, "Practical surface analysis", Edited by D. Briggs and M. P. Seah, John Wiley, Chichester, 1990.

[126] P. Swift, "Adventitious carbon - the panacea for energy referencing?", Surf. Interface Anal., 4 (1982) 47.

[127] A. K. Bhattacharya, D. R. Pyke, G. S. Walker, and C. R. Werrett, "Surface reactivity of different aluminas as revealed by their XPS C1s spectra", Appl. Surf. Sci., 108 (1997) 465.

[128] A. K. Bhattacharya, D. R. Pyke, R. Reynolds, G. S. Walker and C. R. Werrett, "The use of O1s charge referencing for the X-ray photoelectron spectroscopy of Al/Si, Al/Ti and Al/Zr mixed oxides", J. Mater. Sci. Lett., 16 (1997) 1.

[129] C. R. Werrett, A. K. Bhattacharya, and D. R. Pyke, "Validity of Cls charge referencing in the XPS of oxidised Al-Si alloys", Appl. Surf. Sci., 103 (1996) 403.

[130] Y. S. Tang and N. K. Huang, "X-ray photoelectron spectroscopic studies of the O 1s state on the surface of dual ion beam deposited ZrOx films", Solid. State. Commun., 77 (1991) 341.

[131] R. L. Pecsok and L. D. Shields, "Modern methods of chemical analysis", Wiley, New York, 1968.

[132] A. T. Schwartz et al., "Chemistry in context", American Chemical Society, Washington, DC, 1994.

[133] T. López, P. Bosch, M. Asomoza, R. Gómez and E. Ramos, "DTA-TGA and FTIR spectroscopies of sol-gel hydrotalcites: aluminum source effect on physicochemical properties", Mater. Lett., 31 (1997) 311.

[134] W. Zheng, W. Pang, and G. Meng, "Hydrothermal synthesis of $SrZrO_{3-\alpha}$ (M=Al, Ga, In, $x \leq 0.20$) series oxides", Solid State Ionics, 108 (1998) 37.

[135] S. C. Pillai, S. W. Boland and S. M. Haile, "Low-temperature crystallization of sol-gel processed $Pb_{0.5}Ba_{0.5}TiO_3$: powders and oriented thin films", J. Amerc. Cermic. Soci., 87 (2004) 1388.

[136] K. Hwang, J. Song, B. Kang and Y. Park, "Sol–gel derived hydroxyapatite films on alumina substrates", Surface and Coatings Technology, 123 (2000) 252.

[137] S. Y. Hou, J. Kwo, R. K. Watts, J. Y. Cheng, and D. K. Fork, "Structure and properties of epitaxial $Ba_{0.5}Sr_{0.5}TiO_3/SrRuO_3/ZrO_2$ heterostructure on Si grown by off-axis sputtering", Appl. Phys. Lett., 67 (1995) 1387.

[138] W. D. Kingery, H. K. Bowen, and D. R. Uhlmann, "Introduction to ceramics", Wiley, 1991.

[139] N. Vittayakorn, G. Rujijanagul, and T. Tunkasiri, "Perovskite phase formation and ferroelectric properties of the lead nickel niobate-lead zinc niobate-lead zirconate titanate ternary system", J. Mater. Res., 18 (2003) 2882.

[140] B. Kralik, E. K. Chang, and S. G. Louie, "Structural properties and quasiparticle band structure of zirconia", Phys. Rev. B., 57 (1998) 7027.

[141] M. Balog, M. Schieber, M. Michman, and S. Patai, "The chemical vapour deposition and characterization of ZrO_2 films from organometallic compounds", Thin Solid Films, 47 (1977) 109.

[142] S. B. Krupanidhi and C. J. Peng, "Studies on structural and electrical properties of barium strontium titanate thin films developed by metallo-organic decomposition", Thin Solid Films, 305 (1997) 144.

[143] Y. Fukuda, K. Numata, K. Aoki, and A. Nishimura, "Origin of dielectric relaxation observed for $Ba_{0.5}Sr_{0.5}TiO_3$ thin-film capacitor", Jpn. J. Appl. Phys., 35 (1996) 5178.

[144] H. N. Al-Shareef and A. I. Kingon, "Ferroelectric thin films: Synthesis and basic properties", Gordon and Broach, Amsterdam, 1996.

[145] K. Sreenivas, I. Reaney, T. Maeder, N. Setter, C. Jagadish, and R. G. Elliman, "Investigation of Pt/Ti bilayer metallization on silicon for ferroelectric thin film integration", J. Appl. Phys., 75 (1994) 232.

[146] H. N. AL-Shareef, K. D. Gifford, S. H. Rou, P. D. Hren, O. Auciello, and A. I. Kingon, "Electrodes for ferroelectric thin films", Integrat. Ferroelectr., 3 (1993) 321.

[147] W. Zhu, O. K. Tan, and X. Yao, "Amorphous ferroelectric $(Ba_{0.67}Sr_{0.33})Ti_{1.02}O_3$ thin films with enhanced H_2 induced interfacial polarization potential", J. Appl. Phys., 84 (1998) 5134.

[148] S. Q. Wang and J. W. Mayer, "Oxygen sinks in reactions of thin bilayer refractory metal films with SiO_2 substrates", Thin Solid Films, 202 (1991) 105.

[149] S. T. Kim, C. Y. Kim, K. H. Park, K. Y. Kim, and J. S. Lee, "Study on microstructrues and interdiffusion behavior in Pt/Ti/SiO_2/Si and Pb(Zr,Ti)O_3/ Pt/Ti/SiO_2/Si multilayer systems", Jpn. J. Appl. Phys., 34 (1995) 4945.

[150] A. Ehrlich, U. Weiβ, W. Hoyer, and T. Geβner, "Microstructural changes of Pt/Ti bylayer during annealing in different atmosphere-an XRD study", Thin Solid Films, 300 (1997) 122.

[151] T. C. Tisone and J. Drobek, "Diffusion in thin film Ti–Au, Ti–Pd, and Ti–Pt couples", J. Vac. Sci. Technol., 9 (1972) 271.

[152] C. Miot, E. Husson, C. Proust, R. Erre, JP. Coutures, "X-ray photoelectron spectroscopy characterization of barium titanate ceramics prepared by the citric route. Residual carbon study", J. Mater.Res., 12 (1997) 2388.

[153] R. W. Schwartz, T. J. Boyle, S. J. Lockwood, M. B. Sinclair, D. Dimos and C. D. Buchheit, "Sol-gel processing of PZT thin films: A review of the state-of-the-art and processing optimization strategies", Integr. Ferroelectr., 7 (1995) 259.

[154] S. Bhaskar, S. B. Majurnder, E. R. Fachini and R. S. Katiyar, "Influence of precursor solutions on the ferroelectric properties of sol-gel-derived lanthanum-modified lead titanate (PLT) thin films", J. Am. Ceram. Soc., 81 (2004) 384.

[155] J. Y. Zhang, L. J. Bie, V. Dusastre and I. W. Boyd, "Thin tantalum oxide films prepared by 172 nm Excimer lamp irradiation using sol-gel method", Thin Solid Films, 318 (1998) 252.

[156] R. Waser, T. Baiatu, and K. H. hardtl, "DC electrical degradation of perovskite-type titanates", J. Am. Ceram. Soc., 63 (1990) 1645.

[157] D. M. Smyth, M. P. Harmer, and P. Peng, "Defect chemistry of relaxor ferroelectrics and the implications for dielectric degradation", J. Am. Ceram. Soc., 72 (1989) 2276.

[158] G. W. Neudeck, "The pn junction diode", Addison-Wesley, 1987.

[159] G. Blatter and F. Greuter, "Carrier transport through grain boundaries in semiconductors", Phys. Rev. B., 33 (1986) 3952.

[160] J. G. Simmons, "Poole-Frenkel Effect and Schottky Effect in Metal-Insulator-Metal Systems", Phys. Rev., 155 (1967) 657.

[161] S. Ezhilvalavan and T. Y. Tseng, "Conduction mechanisms in amorphous and crystalline Ta_2O_5 thin films", J. Appl. Phys., 83 (1998) 4797.

[162] S. Banerjee, B. Shen, I. Chen, J. Bohlman, G. Brown, and R. Doering, "Conduction mechanisms in sputtered Ta_2O_5 on Si with an interfacial SiO_2 layer", J. Appl. Phys., 65 (1989) 1140.

[163] C. Chaneliere, J. L. Autran, and R. A. B. Devine, "Conduction mechanisms in Ta_2O_5/SiO_2 and Ta_2O_5/Si_3N_4 stacked structures on Si", J. Appl. Phys., 86 (1999) 480.